Size-resolved isotope analysis reveals anthropogenic reactive nitrogen transport and transformation in Taiwan mountain forests

Wen-Chien Lee,[1] Ming-Hao Huang,[1] Wei-Chieh Huang,[1] Jen-Ping Chen,[1] Yen-Jen Lai,[2,3] Haojia Ren,[4]* and Hui-Ming Hung[1]*

[1] Department of Atmospheric Sciences, National Taiwan University, Taipei, 10617, Taiwan

[2] Experimental Forest, National Taiwan University, Nantou, 557004, Taiwan

[3] Department of Agricultural Chemistry, National Taiwan University, Taipei, 10617, Taiwan

[4] Department of Geosciences, National Taiwan University, Taipei, 10617, Taiwan

Correspondence to: Haojia Ren (abbyren@ntu.edu.tw) and Hui-Ming Hung (hmhung@ntu.edu.tw)

Abstract.

Reactive nitrogen (Nr) species such as particulate ammonium ($p\mathrm{NH_4^+}$) and nitrate ($p\mathrm{NO_3^-}$) are critical drivers of ~~cause~~ air pollution and ~~affect~~ ecosystem~~s~~ health, yet their transformation processes in mountain forests are not well-characterized. We address this ~~Size-resolved isotope analysis of aerosols could reveal these processes, but is rarely performed due to low particle concentrations. We overcame this limitation~~ by combining size-segregated aerosol sampling at Xitou, Taiwan, with sensitive isotopic techniques and Bayesian modeling. Functional groups were analyzed by Fourier-transform infrared spectroscopy (FTIR-ATR), and isotopes $\delta^{15}\mathrm{N}$ and $\delta^{18}\mathrm{O}$ were measured by gas chromatography-isotope ratio mass spectrometry (GC-IRMS), enabling quantification of $p\mathrm{NH_4^+}$ source contributions and $p\mathrm{NO_3^-}$ formation pathways. Typical diurnal patterns, with higher daytime particle concentrations, were disrupted during a 26-hour fog ~~caused by~~with stagnant ~~atmospheric~~ conditions, suppressing the advection of isotopically enriched urban plumes~~. During fog, the average $\delta^{15}\mathrm{N\text{-}NH_4^+}$ decreased from 11.75±2.42‰ (mean±1σ) during clear periods to 7.75±1.37‰, while $\delta^{15}\mathrm{N\text{-}NO_3^-}$ dropped from −2.57±1.80‰ to −4.51±1.79‰~~ and promoting~~, indicating continued isotopic fractionation~~aqueous phase gas-particle isotopic re-equilibration under reduced urban influence~~. Under clear conditions, size-resolved $\delta^{15}\mathrm{N\text{-}NH_4^+}$ exhibited a bell-shaped distribution peaking at the accumulation mode, but this gradient flattened during fog. Size-resolved δ^{15}~~isotope~~ N and $\delta^{18}\mathrm{O}$ results of $p\mathrm{NO_3^-}$ revealed two distinct nitrate formation regimes~~evolution during transport~~: urban plumes retained $\mathrm{O_3}$-driven oxidation signatures with ~~isotopic fractionation~~higher $\delta^{18}\mathrm{O}$, ~~whereas mountain~~and rural/~~-~~local regimes dominated by ~~formed nitrate was produced via~~ $\mathrm{RO_2}$-involved processes with greater isotopic ~~fractionation~~ depletion and enhanced biogenic contributions. Bayesian modeling indicated that 50−83% of $\mathrm{NH_3}$ emissions originated from combustion-related sources, while $\mathrm{RO_2}$-initiated oxidation dominated daytime $p\mathrm{NO_3^-}$ formation (42−95%) ~~of $p\mathrm{NO_3^-}$ formed through $\mathrm{RO_2}$ initiated oxidation during daytime~~ and heterogeneous reactions contributed 6−84% ~~through heterogeneous reactions~~ at night. These findings emphasize the importance of controlling urban $\mathrm{NO_x}$ and combustion-related $\mathrm{NH_3}$ emissions ~~to reduce downwind Nr pollution~~ and demonstrate how size-resolved isotope analysis elucidates aerosol evolution along transport pathways.

1. Introduction

Anthropogenic activities have significantly altered the global ~~increased~~ reactive nitrogen (Nr) cycle~~in the Earth system~~, ~~contributing to~~ with profound implications for climate change, biodiversity loss, acid deposition, and air ~~pollution~~quality. Among Nr species, particulate ammonium (pNH_4^+) and nitrate (pNO_3^-) derived from ammonia (NH_3) and nitrogen oxides (NO_x), respectively, are major pollutants that degrade ~~air quality, reduce~~ visibility~~,~~ and increase human morbidity (Gong et al., 2024; Zhang et al., 2017). In Asian ~~countries~~regions, these species account for approximately 10−37% of non-refractory PM_1 (particulate matter with a diameter less than 1 μm) mass (Zhou et al., 2020). ~~Although~~ While anthropogenic Nr is frequently transported to rural and remote areas, its distribution remains ~~uneven~~heterogeneous, exacerbating regional disparities in nitrogen ~~availability~~ deposition and environmental impacts (Galloway et al., 2008). Therefore, understanding the formation pathways, transport mechanisms, and sources of Nr is essential for evaluating its origins and ~~environmental~~ ecological impacts.

Nr is emitted from ~~both~~ a diverse array of anthropogenic and biogenic sources. NH_3 is predominantly released from agricultural activities and is ~~primarily~~ removed through dry deposition, precipitation scavenging, and chemical conversion to pNH_4^+ via reactions with acidic ~~products~~ precursors from NO_x and sulfur dioxide (SO_2) oxidations (Meng et al., 2017). Sources of NO_x include coal combustion, vehicle exhausts, biomass burning, and soil emissions (Fan et al., 2020). ~~NO_x is removed from the atmosphere through oxidation processes (Romer et al., 2016).~~ In the presence of sunlight, ~~atmospheric~~ NO_x undergoes rapid~~ly transforms~~ oxidation through ozone (O_3) or ~~organic~~ peroxy radical (RO_2) pathways (termed P_{O_3} and P_{RO_2}, respectively) before converting to nitric acid (HNO_3) ~~as follows~~via the following reactions:

$$NO + O_3\,(\text{or } RO_2) \rightarrow NO_2 + O_2\,(\text{or } RO)$$

~~$NO + O_3\,(\text{or } RO_2) \rightarrow NO_2 + O_2\,(\text{or } RO)$~~ (R1)

$$NO_2 + h\nu \xrightarrow{O_2} NO + O_3$$

~~$NO_2 + h\nu \xrightarrow{O_2} NO + O_3$~~ (R2)

$$NO_2 + OH + M \rightarrow HNO_3 + M$$

~~$NO_2 + OH + M \rightarrow HNO_3 + M$~~ (R3)

Tropospheric O_3 is a key oxidant formed from the photolysis of NO_2 ~~when volatile organic compounds (VOCs) undergo oxidation in the presence of NO_x and sunlight~~ (Haagen-Smit et al., 1953). Another important oxidant is~~,~~ the RO_2 radical~~s~~, which is primarily formed through the reaction of VOC with ~~during daytime when~~ hydroxyl radicals (OH) and might be more abundant ~~react with biogenic VOCs such as isoprene~~ in forested environments (Romer et al., 2016). ~~In the absence of sunlight~~Under nocturnal or low-light conditions, NO_x accumulates as nitrogen dioxide (NO_2) ~~in the presence of~~ through reaction with O_3, which then undergoes heterogeneous reactions (termed as het) to produce HNO_3 as follows:

$$NO_2 + O_3 \rightarrow NO_3 + O_2$$

~~$NO_2 + O_3 \rightarrow NO_3 + O_2$~~ (R4)

$$NO_3 + NO_2 + M \rightarrow N_2O_5 + M$$

~~$NO_3 + NO_2 + M \rightarrow N_2O_5 + M$~~ (R5)

$$N_2O_5 + H_2O_{(\text{surface})} \rightarrow 2HNO_{3(aq)}$$

$N_2O_5 + H_2O_{(surface)} \rightarrow 2HNO_{3(aq)}$ (R6)

These oxidation processes not only regulate atmospheric chemistry but also leave distinct isotopic signatures for nitrate, making stable isotope analysis a powerful robust tool for tracing the origin, evolution, and transport of aerosol particles (Moore, 1977). The sources of $p$$NH_4^+$ can be distinguished using nNitrogen isotope ratios ($\delta^{15}N = [(^{15}R_{sample})/(^{15}R_{air}) - 1] \times 1000‰$, where ^{15}R is the ratio of $^{15}N/^{14}N$) are used to distinguish emission sources of $p$$NH_4^+$ and transport of $p$$NO_3^-$, as different emission sources exhibit characteristic $\delta^{15}N$ signatures (Savard et al., 2017; Chang et al., 2018). Additionally, the oxidation pathways leading to $p$$NO_3^-$ formation can be inferred from while oxygen isotope ratios ($\delta^{18}O = [(^{18}R_{sample})/(^{18}R_{VSMOW}) - 1] \times 1000‰$, where ^{18}R is the ratio of $^{18}O/^{16}O$) in $p$$NO_3^-$ provide insights into specific oxidation pathways, as , since each oxidant (O_3, OH, RO_2) imparts a unique $\delta^{18}O$ signature isotopic fingerprint (Walters and Michalski, 2016).

The sources of $p$$NH_4^+$ and the formation mechanisms of $p$$NO_3^-$ have successfully been identified using Although isotopic- Bayesian mixing model frameworks (e.g., IsoSource, SIAR, or MixSIAR) have successfully identified the sources of Nr and the formation mechanisms of $p$$NO_3^-$ (Fan et al., 2020; Chang et al., 2018; Kawashima et al., 2023; Pan et al., 2016). However, these processes are spatially highly variable in complex terrains., and relatively l Little is known about the sources and atmospheric processing of Nr in East Asian mountain forests, where complex interactions between local emissions and long range transported pollutants interact under high-humidity conditionsare common (Guha et al., 2017). During atmospheric transport, $\delta^{15}N$ values are modified by kinetic fractionation and gas-particle partitioning, often leading to a progressive depletion of heavier isotopesnitrogen isotope ratios undergo modifications due to deposition, chemical transformation, and photochemical processes. In particular, the gas-particle partitioning between NH_3 and $p$$NH_4^+$ can lead to a progressive decrease in $\delta^{15}N$ NH_4^+ values with increasing transport distance (Pan et al., 2016). Similarly, $p$$NO_3^-$ experiences gradual $\delta^{15}N$ depletion during long-range transport as kinetic fractionation during HNO_3 uptake preferentially incorporates lighter isotopes into the particulate phase (Gobel et al., 2013; Walters and Michalski, 2016). HoweverFurthermore, due to the typically low concentrations of mountain aerosols have historically limited detailed particles, detailed $\delta^{15}N$ and $\delta^{18}O$ analyses of size-segregated isotopic analysesaerosol particles remain limited, constraining our understanding of emission sources and size-dependent nitrogen transformation pathways (Morin et al., 2009).

Xitou, a representative cloud forest in central Taiwan, serves as an ideal natural laboratory to address these gaps. Situated in a valley oriented toward urban regions, the site experiences predictable valley-mountain breeze circulations that transport anthropogenic plumes into a biogenic-rich environment where Nr accounts for 13–23% of PM_{10} mass (Chen et al., 2021). This mixing vessel is characterized by frequent fog and persistent humidity, with a mean relative humidity (RH) above 80%. F(Hsieh et al., 2019)og droplets serve as a reactive aqueous medium, facilitating the dissolution of Nr species and accelerating secondary aerosol formation through aqueous-phase oxidation, thereby modifying aerosol hygroscopicity and chemical aging (Ervens, 2015). Specifically, aqueous-phase nitrate formation during fog proceeds via oxidation of NO_2 by ·OH radicals and heterogeneous hydrolysis of N_2O_5 on fog droplet surfaces. Furthermore, NO_2 disproportionation represents an additional pathway, a process enhanced by the larger radii of fog droplets compared to aerosol particles (Zhang et al., 2022; Lin et al., 2026; Yu et al., 2023). In addition, recent field research has demonstrated efficient nitrate formation during fog occurs mainly on fog interstitial aerosols through NO_2 and N_2O_5 hydrolysis, highlighting the importance of size-resolved characterization of aerosols under fog conditions (Xu et al., 2024).

While previousThe prolonged fog can significantly alter aerosol composition and isotopic signals by promoting aqueous-phase reactions and enhancing local gas-particle partitioning.

Previous work at Xitou has characterized winter Nr sources using $\delta^{15}N$ and $\delta^{18}O$ isotope signatures (Chen, T. Y. et al., 2022), yet the influence of role of prolonged fog and stagnant atmospheric conditions due to suppressed atmospheric transport on isotopic distributions was not well investigated. The prolonged fog can significantly alter aerosol composition and isotopic signals by promoting aqueous-phase reactions and enhancing local gas-particle partitioning.remains poorly resolved.

In this study, we investigate the size-dependent isotope distribution of aerosols during ~~and examine~~ a rare ~26-hour fog episode to ~~understand~~ examine how extreme humidity and suppressed transport~~stagnant and high-RH conditions modulate~~ modulate the transformation ~~and distribution patterns~~ of pNH_4^+ and pNO_3^-. By combining size-segregated sampling ~~Using stable isotope analysis~~ with Bayesian source apportionment ~~modeling~~, we ~~investigate~~ evaluate the relative contributions of local ~~and~~ versus transported sources and evaluate how fog conditions affect the isotopic composition of Nr species in a subtropical mountain forest. This study provides valuable insights into aqueous-phase nitrogen processing, offering a clearer picture of how stagnant meteorological regimes alter chemical evolution in a subtropical mountain environment~~Nr sources and atmospheric transformation processes, which are essential for informing effective air quality management strategies~~.

2. Methods

2.1. ~~Sample collection~~Site description and sampling

~~FA f~~ield measurements ~~was~~ were conducted from 17 to 24 April 2021, at the Xitou Experimental Forest of National Taiwan University (23°40'12" N, 120°47'54" E, 1179 m a~~bove sea level~~.s.l.; Fig. S1). April represents the spring transition in Taiwan, a period characterized by frequent fog at Xitou, and a shift in aerosol loading from wintertime maxima to summertime minima.~~The measurement site is located in a river valley adjacent to the western foothills of Taiwan's Central Mountain Range, approximately 65–75 km southeast of the Taichung metropolitan area and 50–60 km inland from the Taiwan Strait. The area is characterized by limited direct anthropogenic influence, with no significant industrial facilities, oil refineries, or large-scale farming operations, though some small-scale agriculture activities exist locally. During the measurement period, size-segregated aerosol particles were collected for daytime and nighttime intervals to analyze their chemical composition and the isotopic signatures ($\delta^{15}N$ and $\delta^{18}O$) of Nr species. Meanwhile, meteorological parameters and atmospheric conditions were monitored. The isotopic data $\delta^{15}N$-NH_4^+ and $\delta^{18}O$-NO_3^- were further applied to estimate the sources and formation pathways of Nr aerosols using a Mixed Stable Isotope Analysis in R (MixSIAR) framework (Stock et al., 2018).~~

~~2.1. Sample collection~~

Size-segregated aerosol samples were collected during alternating daytime (09:00 to 17:00 LT, denoted as 'D') and nighttime (18:00 to 06:00 LT on the following day, denoted as 'N') intervals using a micro-orifice uniform deposit impactor (MOUDI, Model 125R, MSP Corporation, Shoreview, Minnesota, USA) ~~equipped with 46.2 mm polytetrafluoroethylene (PTFE) filters (Whatman 7592–104)~~. The MOUDI was operated at a flow rate of 30 L min^{-1}, ~~providing~~ with aerodynamic cut-point diameters of 0.056, 0.1, 0.18, 0.32, 0.56, 1.0, 1.8, 3.2, 5.6, and 10 μm. The higher flow rate (30 vs. 10 L min^{-1}) relative to the prior winter study yielded greater particle mass for analysis. Sampling was conducted on 46.2 mm polytetrafluoroethylene (PTFE) filters (Whatman 7592-104) ~~a half-day basis, with daytime (09:00 to 17:00 LT, denoted as 'D') and nighttime (18:00 to 06:00 LT on the following day, denoted as 'N') periods. Each sample was~~ labeled by day and night intervals as 'ddD' or 'ddN', where 'dd' represents the day of ~~the month~~(e.g., "17D"). ~~After sample collection, filters~~ Samples were sealed in aluminum foil and stored at 4°C ~~until~~ prior to analysis.

Meteorological parameters, including pressure, temperature, RH, trace gases, visibility, and radiation, were monitored by ~~During the sampling period,~~ a custom-built Air Quality Box (AQB) and the on-site Agricultural Meteorological Station. Among the trace gases measured by AQB ~~was applied to continuously monitor meteorological parameters, including temperature, relative humidity (RH), and trace gas concentrations (CO, NO, NO_2, and O_x (NO_2 + O_3)). However, due to the stability of the calibration issue~~, carbon monoxide (CO) was selected as the primary tracer for analysis due to its reliable calibration ~~only CO is considered in this study~~ (Huang, W. C. et al., 2024). ~~Additionally, visibility, radiation, wind speed, and wind direction data were acquired from the Agricultural Meteorological Station of the Experimental Forest, College of Bio-Resources and Agriculture, National Taiwan University.~~

2.2. Sample analysis and isotope measurements

The analytical workflow involved~~Sample analysis consisted of three sequential steps~~: concentration ~~measurement~~screening, aqueous extraction, and isotopic measurements (Fig. 1~~1~~). ~~First~~Initially, attenuated total reflectance Fourier transform infrared spectroscopy (ATR-FTIR, Nicolet 6700, Thermo Fisher Scientific, Madison, WI, USA) was used to semi-quantitatively screen~~fy sample concentrations on the~~ filters ~~to ensure~~ for sufficient nitrogen content (≥ 1 μM N as NO_3^- + NH_4^+~~,~~) ~~for size-resolved isotope analysis,~~ with details in Supplementary Description S1). Filters from adjacent size bins with insufficient loading ~~collected during the same period~~ were combined, and ~~when samples contained insufficient N content. The combined filters, with~~ a mass-weighted ~~particle~~ diameter was calculated ~~following~~ as detailed in Supplementary Description S2.

Filters~~,~~ were extracted in 30 mL Milli-Q water (18.2 MΩ at 25°C) using 30-min ultrasonication, followed by ~~and extracts were~~ filter~~ed~~ing through 0.22 μm Millipore syringe filters ~~and stored in high-density polyethylene (HDPE) bottles~~. Total nitrogen (TN) was determined by oxidizing part of the ~~The~~ extract~~eds~~ ~~nitrogen species were oxidized~~ to nitrate ~~ion~~ (NO_3^-) using potassium persulfate ~~reagent for total nitrogen (TN) analysis~~. The bacterial denitrifier method was subsequently employed to measure the $\delta^{15}N$ of TN, and the $\delta^{15}N$ and $\delta^{18}O$ of nitrate + nitrite (NO_3^- + NO_2^-, NN). Two bacterial strains were employed: *Pseudomonas chlororaphis* (ATCC® 43928™, Manassas, VA, USA) for TN analysis and *Pseudomonas chlororaphis ssp. aureofaciens* (ATCC® 13985™, Manassas, VA, USA) for NN analysis to convert NO_3^- to nitrous oxide (N_2O) gas while preserving isotopic integrity (Weigand et al., 2016). Isotopic ratios of N_2O were measured via gas chromatography-isotope ratio mass spectrometry (GC-IRMS) and calibrated against international isotope standards: USGS 34 ($\delta^{15}N$ = −1.8‰; $\delta^{18}O$ = −27.93‰) and IAEA-NO_3 ($\delta^{15}N$ = +4.7‰; $\delta^{18}O$ = +25.61‰) (Böhlke et al., 2003). Detailed descriptions of isotope measurement procedures are provided by Chen, T. Y. et al. (2022).

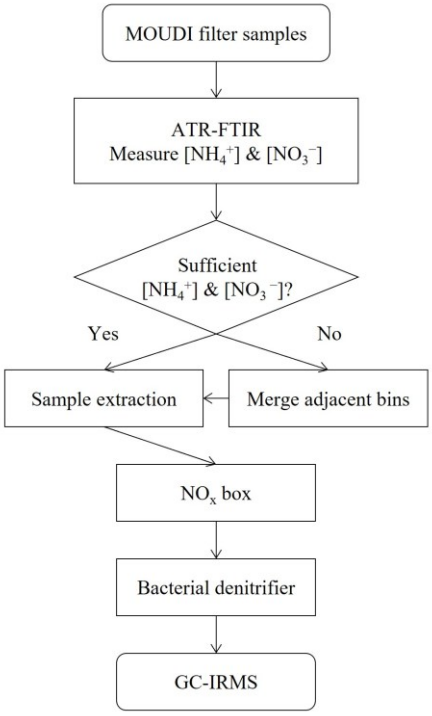

Figure 1. Schematic diagram of sampling and isotope analysis procedures.

~~Subsequently, the bacterial denitrifier method was employed to measure the $\delta^{15}N$ of TN, as well as both $\delta^{15}N$ and $\delta^{18}O$ of nitrate + nitrite (NO_3^- + NO_2^-, NN). Two bacterial strains were employed: *Pseudomonas*~~

~~*chlororaphis* (ATCC® 43928™, Manassas, VA, USA) for TN analysis and *Pseudomonas chlororaphis ssp. aureofaciens* (ATCC® 13985™, Manassas, VA, USA) for NN analysis. These bacteria converted sample NO_3^- to nitrous oxide (N_2O) while preserving the original isotopic compositions of both N and O elements (Weigand et al., 2016). Gas chromatography-isotope ratio mass spectrometry (GC-IRMS) was used to analyze the resulting N_2O for the simultaneous determination of $\delta^{15}N$ and $\delta^{18}O$ values. The system was calibrated using two international isotope standards: USGS 34 ($\delta^{15}N$ = −1.8‰; $\delta^{18}O$ = −27.93‰) and IAEA NO_3 ($\delta^{15}N$ = +4.7‰; $\delta^{18}O$ = +25.61‰)(Böhlke et al., 2003). Detailed descriptions of isotope measurement procedures are provided by Chen, T. Y. et al. (2022).~~

Given that NO_2^- concentrations detected by IC analysis were negligible, ~~Isotopic values measured for~~ NN values were considered as representative of $p$$NO_3^-$ (i.e., $\delta^{15}N\text{-}NN \approx \delta^{15}N\text{-}NO_3^-$; $\delta^{18}O\text{-}NN \approx \delta^{18}O\text{-}NO_3^-$) ~~due to negligible NO_2^- concentrations detected by IC analysis~~. ~~Since~~ If TN primarily comprises NH_4^+ and NN, the $\delta^{15}N$ of $p$$NH_4^+$ can be calculated via mass balance ~~isotopic values measured for TN minus those for NN were assumed to represent NH_4^+, expressed as~~:

$$\delta^{15}N\text{-}NH_4^+ = \frac{\delta^{15}N_{TN} \times M_{TN} - \delta^{15}N_{NN} \times M_{NN}}{M_{TN} - M_{NN}} \quad (1)$$

~~$$\delta^{15}N\text{-}NH_4^+ = \frac{\delta^{15}N_{TN} \times M_{TN} - \delta^{15}N_{NN} \times M_{NN}}{M_{TN} - M_{NN}}, \quad (1)$$~~

where M_{TN} and M_{NN} represent the molarities of TN and NN ~~in the sample solution~~, respectively, measured by the photolytic $NO/NO_2/NO_x$ analyzer (NO_x box, Model T200P, Teledyne API). Stringent quality control was applied: ~~For quality control, $\delta^{15}N\text{-}NH_4^+$ isotope~~ data points were excluded ~~from analysis~~ if NN ~~comprised greater than~~ exceeded 80% of TN or if NH_4^+ was ~~represented~~ less than 60% of water-soluble reduced nitrogen (i.e., M_{TN}−M_{NN}). The latter criterion was based on the assumption that contributions from organic nitrogen were negligible under these conditions. The NH_4^+ concentration was determined on a fluorescence spectrophotometer (Hitachi F-2700) using a fluorometric method (Holmes et al., 1999). ~~For quality control, $\delta^{15}N\text{-}NH_4^+$ isotope data points were excluded from analysis if NN comprised greater than 80% of TN or if NH_4^+ represented less than 60% of TN−NN. The latter criterion was based on the assumption that contributions from organic nitrogen were negligible under these conditions.~~

2.3. Bayesian isotope mixing model framework (MixSIAR)

Source contributions of NH_3 and the formation pathways of $p$$NO_3^-$ were estimated using the MixSIAR framework (v3.1.12), which employs Bayesian models to estimate source contributions while accounting for uncertainties in source values (Stock et al., 2018). The ~~Bayesian~~ model follows the general form ~~is formulated~~ as follows:

$$X_{ij} = \sum_{k=1}^{n} P_k \times S_{jk} + err_{ij}$$

~~$$X_{ij} = \sum_{k=1}^{n} P_k \times S_{jk} + \varepsilon_{ij} \quad (2)$$~~

where X_{ij} is the measured isotope value of tracer j ($\delta^{15}N\text{-}NH_4^+$ or $\delta^{18}O\text{-}NO_3^-$) for ~~the merged filter~~ sample i, P_k is the proportion of source k with $\sum P_k = 1$ ~~$\sum P_k = 1$~~, S_{jk} is the isotope value of ~~tracer j for~~ source k, ~~following~~ (as a normal distribution with mean values and standard deviations), and ~~ε_{ij}~~ err_{ij} is the residual error. The model was run with extended Markov Chain Monte Carlo (MCMC) parameters to ensure convergence, with all runs confirmed to have converged based on the Gelman-Rubin potential scale reduction factor and the Geweke diagnostic (Stock and

Semmens, 2016). Results are reported as mean source contributions with associated standard deviations. To further assess model performance, reconstructed X_{ij} was calculated by weighting S_{jk} with the model-derived P_k and compared to the measured X_{ij}.

2.3.1. Source apportionments of NH_3

To account for isotopic fractionation during the NH_3 to pNH_4^+ transition~~Determining NH_3 emission sources requires analyzing the emitted δ^{15}N-NH_3 values. However, due to isotopic fractionation during the conversion of NH_3 to pNH_4^+, the measured δ^{15}N-NH_4^+ values do not directly reflect NH_3 sources. Since direct δ^{15}N-NH_3 measurements were not available in this study,~~ the initial δ^{15}N-NH_3 (i.e., δ^{15}N-NH_3^0) was estimated from the concentration-weighted mean δ^{15}N-NH_4^+ ~~using an empirical relationship~~ following Pan et al. (2016):

$$\delta^{15}\text{N-NH}_3^{\,0} = \delta^{15}\text{N-NH}_4^+ - \varepsilon_{\mathrm{NH_4^+-NH_3}}\left(1-f\right), \quad (3)$$

where ~~δ^{15}N-NH_4^+ represents the concentration-weighted mean δ^{15}N-NH_4^+ at Xitou,~~ $\varepsilon_{\mathrm{NH_4^+-NH_3}}$ is the isotope fractionation constant ~~assumed as (~~+33‰ for equilibrium isotope effect (EIE) between $NH_{3(g)}$ and $pNH_{4(aq/s)}^+$ (Heaton et al., 1997), and f is the fraction of pNH_4^+ in the NH_3–pNH_4^+ system. Sensitivity tests regarding the temperature dependence, gas–particle equilibrium, and the approximation of equilibrium on $\varepsilon_{\mathrm{NH_4^+-NH_3}}$ were performed, as detailed in Supplementary Description S3 and Table S1 ~~(~~Chang et al., 2025). The f values were ~~estimated using~~ derived from the Community Multiscale Air Quality (CMAQ) model (version 4.7.1), incorporating meteorological data from the Weather Research and Forecasting (WRF) model (version 3.7.1) and the emission database from the Taiwan Emission Data System (version 12) (Tsai et al., 2024). The model-simulated pNH_4^+ mass concentrations agreed with laboratory measurements within a 20% uncertainty range (Fig. S2).

For NH_3 source apportionment, ~~we considered~~ four major emission sources were considered~~, each with characteristic δ^{15}N-NH_3 values~~: fertilizer (−28.3±5.8‰), waste (−17.6±5.6‰), NH_3 slip (−8.2±5.5‰), and fossil fuel emissions (1.8±3.2‰) (Kawashima et al., 2023). These sources can be categorized into two groups based on their δ^{15}N-NH_3 signatures: (1) volatilization-related sources (fertilizer and waste) with lower δ^{15}N-NH_3 values, and (2) combustion-related sources (NH_3 slip and fossil fuel emissions) with higher values (Chen, Z.-L. et al., 2022). δ^{15}N-NH_3 obtained using passive techniques was adjusted by 15‰ to account for systematic differences between collection methods (Kawashima et al., 2023; Walters et al., 2020). Statistical values for MixSIAR analysis are provided in Table S2~~1~~.

2.3.2. Estimating formation pathways of pNO_3^-

δ^{18}O-NO_3^- is applied to evaluate the relative contributions of various HNO_3 formation. Six potential pathways were considered by combining the primary oxidants (P_{O_3} and P_{RO_2}) with three terminal mechanisms (OH1, OH2, and heterogeneous processes (het)). These pathways are characterized by their specific δ^{18}O-NO_3^- signatures (Fig. S3), calculated using a mass-balance approach assuming no kinetic isotope fractionation (Walters and Michalski, 2016). RO_2 was assigned a δ^{18}O of 23.5‰, reflecting that O in RO_2 originates from molecular O_2 (Kroopnick and Craig, 1972). O_3 exhibits elevated δ^{18}O values ranging from 90 to 122‰ (Hastings et al., 2003). OH radicals were split into OH1 (−15 to 0‰) (Dubey et al., 1997), and OH2 (38 to 61‰). Daytime mechanisms included $P_{RO_2\text{-}OH1}$ (33–49‰), $P_{RO_2\text{-}OH2}$ (50–69‰), $P_{O_3\text{-}OH1}$ (55–81‰), and $P_{O_3\text{-}OH2}$ (73–102‰). Nighttime analysis focused on $P_{RO_2\text{-}het}$ (50–69‰) and $P_{O_3\text{-}het}$ (73–102‰), while retaining $P_{RO_2\text{-}OH1}$ to account for residual daytime nitrate that persists into the night. Sensitivity analyses regarding pathway exclusion are detailed in Supplementary Description S44, Tables S3 and S4.

~~To evaluate the contribution of different HNO_3 formation pathways, six potential reaction mechanisms were considered, each characterized by $\delta^{18}O$-NO_3^- signatures, as shown in Fig. S3. These pathways were classified based on the initial reaction step: PXa for the formation initiated by the reaction of NO with RO_2, while PXb for the reaction of NO_2 and O_3. The variable X (1, 2, or 3) denotes the oxidants involved in the second reaction step: OH (from H_2O) as P1, OH (from $O[^1D] + H_2O$) as P2, and O_3 as P3. The $\delta^{18}O$ values of key oxidants were assigned based on their atmospheric sources. RO_2 is assumed to be 23.5‰, reflecting that O in RO_2 originates from molecular O_2 (Kroopnick and Craig, 1972). O_3 exhibits elevated $\delta^{18}O$ values ranging from 90 to 122‰ (Hastings et al., 2003). OH radicals exhibit different $\delta^{18}O$ signatures depending on their formation pathway. A lower $\delta^{18}O$ signature (−15 to 0‰) for OH directly derived from the oxygen atom in H_2O (Dubey et al., 1997), and a higher $\delta^{18}O$ (38 to 61‰) for OH formed via the reaction of $O(^1D)$ (produced from O_3 photolysis) with H_2O due to the oxygen contribution from O_3. The $\delta^{18}O$ of HNO_3 was calculated using a mass balance approach, assuming no kinetic isotope fractionation (Walters and Michalski, 2016). For daytime formation, four pathways were considered: P1a ($\delta^{18}O$-NO_2^-: 33–49‰), P2a ($\delta^{18}O$-NO_3^-: 50–69‰), P1b ($\delta^{18}O$-NO_3^-: 55–81‰), and P2b ($\delta^{18}O$-NO_3^-: 73–102‰). For nighttime formation, pathways P3a ($\delta^{18}O$-NO_3^-: 50–69‰) and P3b ($\delta^{18}O$-NO_3^-: 73–102‰) were considered, while retaining P1a to account for residual from daytime processes (Fig. S3). The inclusion of P1a in nighttime analysis is necessary because the observed nighttime $\delta^{18}O$-NO_3^- values could not be fully explained by typical nocturnal formation pathways (*i.e.*, P3a and P3b) alone. To simplify the nighttime analysis, P2a, P1b, and P2b were excluded due to their overlapping $\delta^{18}O$ signatures with P3a and P3b. However, it is possible that the estimated fractions of P3a and P3b include partial contributions from these excluded pathways.~~

3. Results and discussion

3.1. Environmental variabilities

Figure ~~2~~3 shows the temporal evolution of key ~~various~~ environmental parameters, including temperature (Temp), relative humidity (RH), wind speed (WS), wind direction (WD), radiation (Rad), visibility (Vis), and carbon monoxide (CO) concentration ~~monitored during~~ for the sampling period ~~from 17 to 24 April 2021~~. During ~~the~~ clear-sky periods, the site exhibited pronounced ~~distinct~~ diurnal cycles driven by complex terrain. ~~variations were observed in temperature, RH, wind direction, solar radiation, and CO concentrations.~~ Daytime temperatures (20±2 °C) were consistently higher ~~(20±2 °C)~~ than nighttime values (15±1 °C). Conversely, ~~while~~ RH ~~exhibited the opposite trend, increasing to peaked~~99±1 % at night (99±1 %) and reached a minimum during daytime ~~compared to~~ (87±8 %) ~~during daytime~~. Wind patterns followed typical valley-mountain circulation, with daytime valley winds predominant from the north (316°−33°) ~~and~~ while nighttime mountain ~~winds~~ breezes shifted to the southeast (124°−179°), consistent with previous observations ~~in Xitou~~ (Chen et al., 2021). This circulation, often coupled with ~~The combined effects of daytime valley winds and~~ sea breezes inland penetration, facilitated the diurnal upslope ~~daily~~ transport of air masses from ~~upstream~~ low-altitude urban areas toward the ~~downstream~~ mountain ~~site~~forest, likely introducing anthropogenic pollutants. This transport mechanism is further evidenced ~~pattern is corroborated~~ by CO concentrations, a reliable tracer of combustion emissions, which were consistently higher during the daytime (0.23±0.03 ppm) than at nighttime (0.14±0.03 ppm).

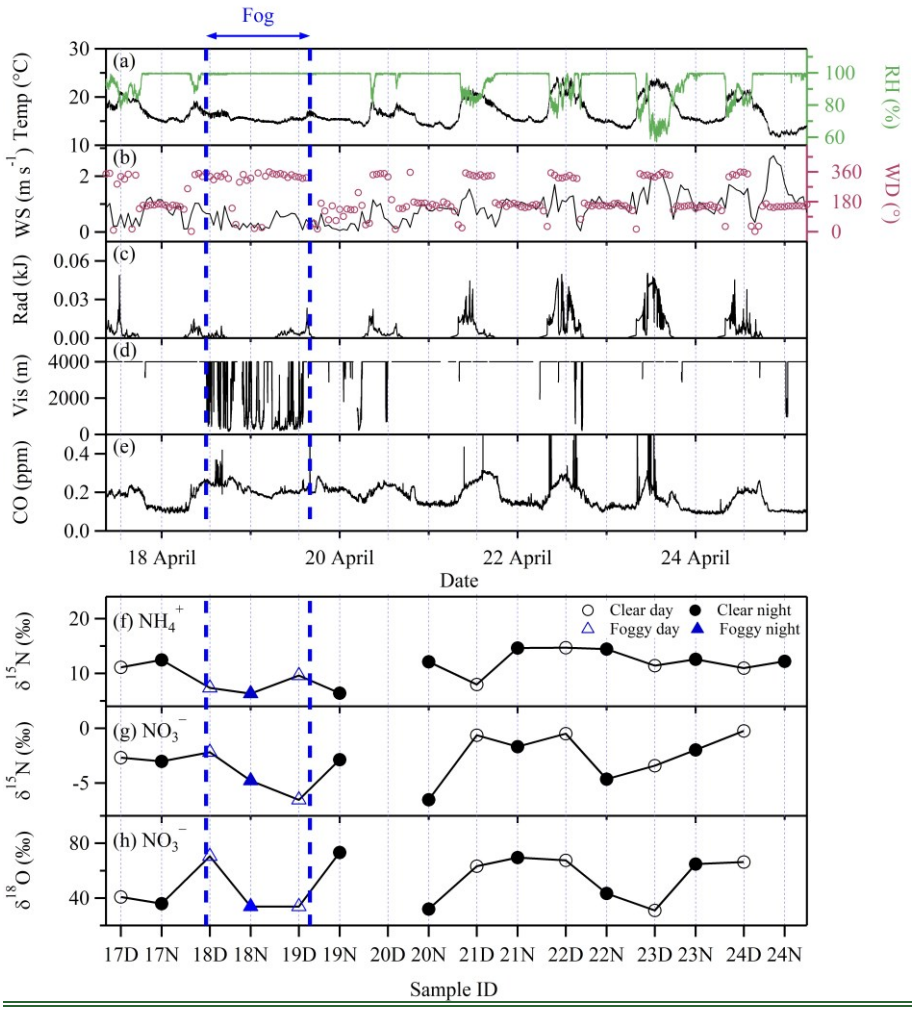

Figure 2. Time series of various environmental parameters measured from 17−24 April 2021, including (a) temperature (Temp) and relative humidity (RH), (b) wind speed (WS) and wind direction (WD), (c) radiation (Rad), (d) visibility (Vis), and (e) CO concentration. The concentration-weighted isotope values for (f) δ^{15}N-NH_4^+, (g) δ^{15}N-NO_3^-, and (h) δ^{18}O-NO_3^- over daytime (09:00−17:00 LT, D) and nighttime (18:00−06:00 LT the next day, N) sampling periods. Uncertainties for δ^{15}N and δ^{18}O measurements are generally less than 0.1‰ and are smaller than the symbol size.

A significant departure from these typical diurnal patterns occurred~~However, meteorological observations~~ during ~~the sampling period revealed~~ a prolonged fog episode lasting approximately 26 hours ~~that disrupted these typical diurnal patterns and influenced local atmospheric dynamics and Nr behavior. This prolonged fog occurred~~ (from 18 April 12:00 to 19 April 14:00). This event was characterized ~~, identified~~ by visibility below 1000 m and RH ~~above~~ exceeding 90% for at least one hour. During this episode, the local atmosphere became exceptionally stagnant: Mean ~~~26 hour period,~~ wind speed decreased from 0.9±0.6 m s^{-1} to 0.5±0.5 m s^{-1}, with approximately 25% of observations ~~recording~~ < 0.1 m s^{-1}~~, indicating stagnant conditions. Meanwhile, t~~ Temperature (15±1 °C) and RH (99.5±0.2 %) remained relatively stable, effectively locking the meteorological state. Notably, ~~and~~ CO concentrations during the foggy night (0.22±0.03 ppm) remained as high as ~~were comparable to those observed during clear~~ clear daytime levels. This lack of nocturnal ventilation suggests that pollutants were trapped within the valley~~, indicating that pollutants were not removed during nighttime and that transport was limited~~, creating a quasi-closed~~-~~ system ~~environment~~ highly conducive to in-situ chemical transformations and aqueous-phase processing.

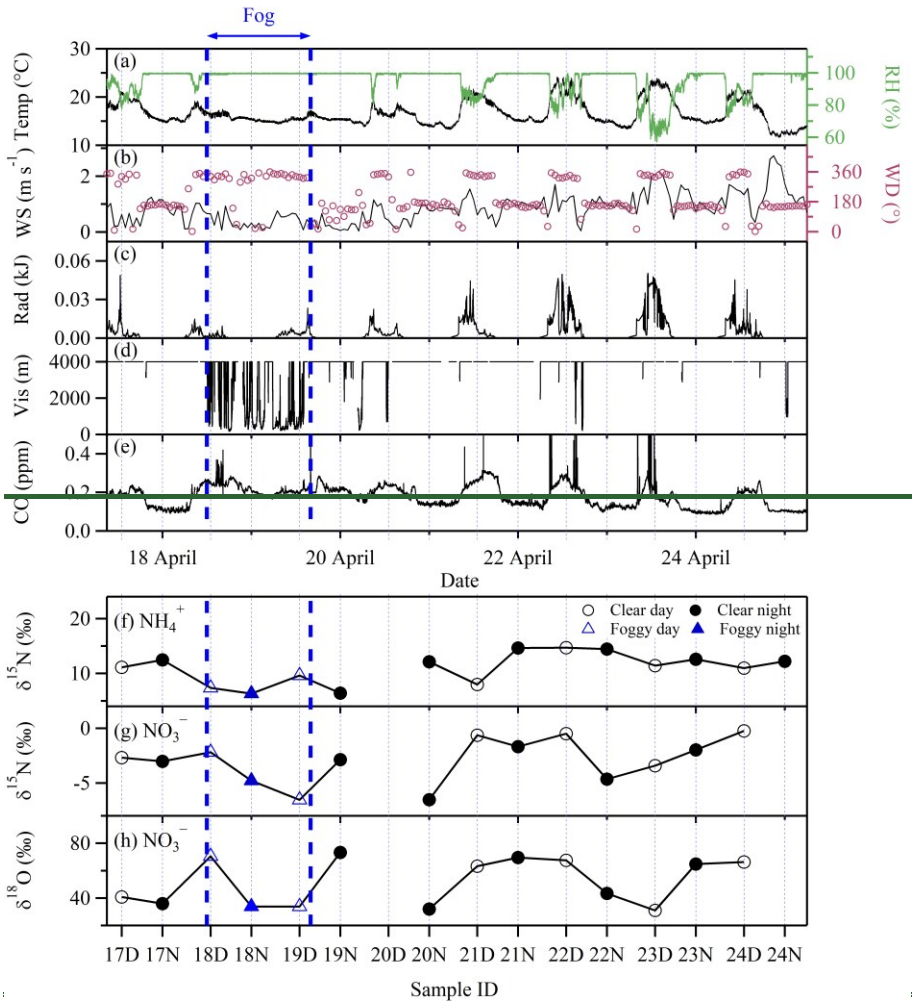

~~**Figure 2. Time series of various environmental parameters measured from 17–24 April 2021, including (a) temperature (Temp) and relative humidity (RH), (b) wind speed (WS) and wind direction (WD), (c) radiation (Rad), (d) visibility (Vis), and (e) CO concentration. The concentration-weighted isotope values for (f) $\delta^{15}N$-NH_4^+, (g) $\delta^{15}N$-NO_3^-, and (h) $\delta^{18}O$-NO_3^- over daytime (09:00–17:00 LT, D) and nighttime (18:00–06:00 LT the next day, N) sampling periods.**~~

3.2. Size-resolved aerosol chemical composition

The ~~effects~~ impact of the prolonged fog on the mass concentration distributions of NH_4^+, NO_3^-, SO_4^{2-}, and black carbon (BC) as a function of particle size ~~are~~ is shown in Fig. ~~3~~3 (detailed temporal variation is provided in Fig. S4). ~~During~~ Under the clear period (~~Fig. 3,~~ left panels), ~~these~~ all four species exhibited higher daytime concentrations than nighttime values. NH_4^+, SO_4^{2-}, and BC ~~exhibited~~ peaked ~~concentrations~~ in the 0.32–0.56 μm range during the daytime, and shifted to 1–1.8 μm with a broader distribution and lower total concentrations at nighttime. In comparison, NO_3^- showed a bimodal distribution, with peaks at 0.56–1 μm and 3.2–5.6 μm during daytime, shifting to 1–1.8 μm and 3.2–5.6 μm at nighttime. These ~~variations~~ shifts likely reflect coagulation and hygroscopic ~~processes contributing to particle~~ growth under elevated nocturnal RH ~~conditions~~.

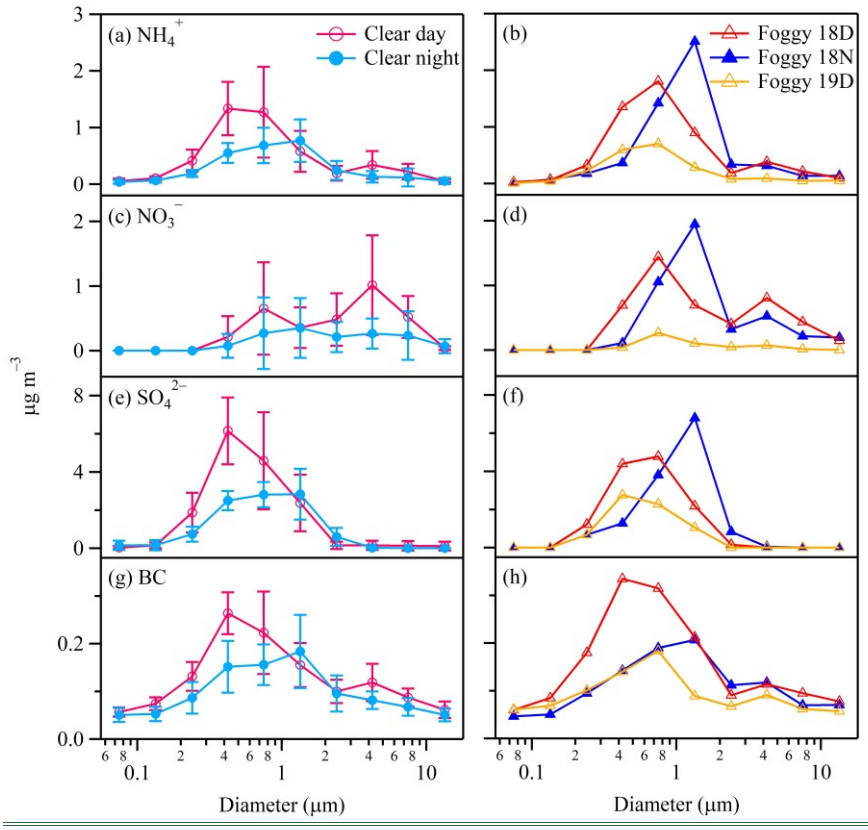

Figure 3. Size-resolved mass concentration distributions of particulate (a,b) NH_4^+, (c,d) NO_3^-, (e,f) SO_4^{2-}, and (g,h) black carbon (BC) estimated from FTIR analysis during clear (left panels) and foggy (right panels) periods.

During the foggy period (Fig. 3, right panels), the mass concentration distributions on 18D remained within the variability range observed during clear periods, with peaks around 0.32–1 μm. Compared with clear days, nitrate concentrations in the sub-micrometer NO_3^- concentrations region increased on 18D, surpassing those observed in the coarse-mode levels. This enhancement likely resulted from the accelerated enhanced HNO_3-NH_3 partitioning processes, promoted by the high surface-to-volume ratio and elevated water content of sub-micrometer particles during the hygroscopic growth at high RHonset of fog. On By 18N, all species exhibited peak shifts to the 1−1.8 μm range, indicating substantial hygroscopic growth and coagulation during the fog period. While total concentrations of NH_4^+, SO_4^{2-}, and NO_3^- remained relatively stable compared to 18D, the observed decrease in BC suggests a transition, where aqueous chemistry in the fog droplets compensated for the mass lost to deposition. On the following day In the subsequent interval (19D), concentrations of all species decreased, likely resulting from wet deposition of larger droplets and reduced suppressed pollutant transport under stagnant conditions. A time series showing the changes in concentration of pNH_4^+, pNO_3^-, pSO_4^{2-}, and BC is provided in Fig. S4. These observations demonstrate that prolonged fog conditions not only enhanced local chemical transformations processes and but also fundamentally altered particle size distributions. Such shifts in composition and The changes in particle size and composition provide the critical framework laid the foundation for interpreting isotopic shifts fractionation and reactive nitrogen Nr transformations discussed in subsequent the following sections.

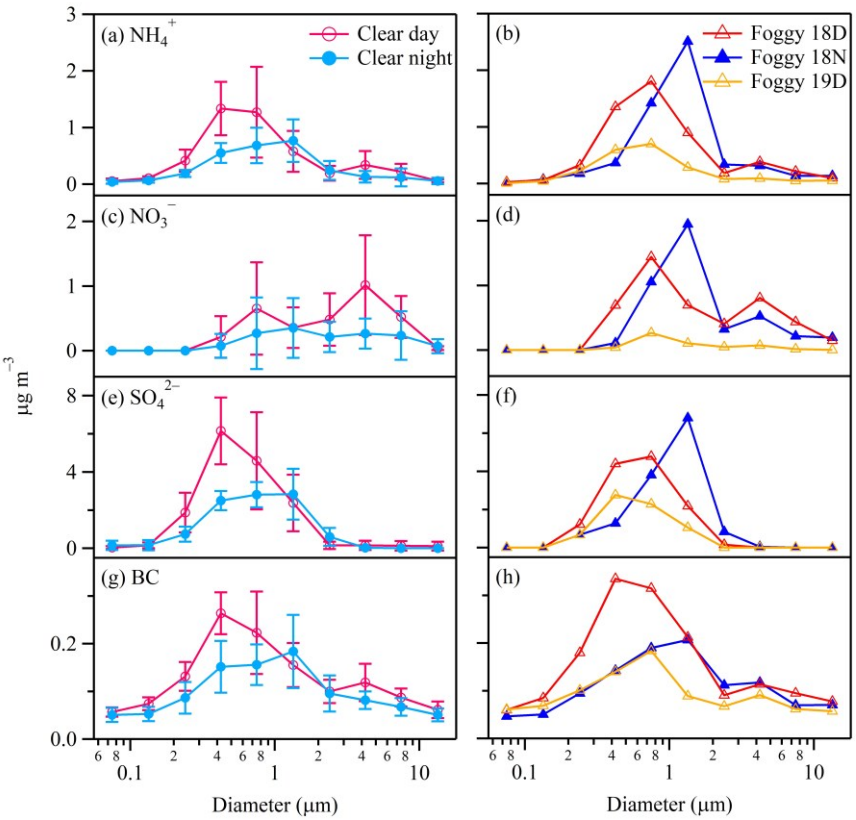

~~**Figure 3. Size-resolved mass concentration distributions of particulate (a,b) NH_4^+, (c,d) NO_3^-, (e,f) SO_4^{2-}, and (g,h) black carbon (BC) estimated from FTIR analysis during clear (left panels) and foggy (right panels) periods.**~~

3.3. δ^{15}N-NH_4^+ and derivation of emitted δ^{15}N-NH_3

3.3.1. δ^{15}N-NH_4^+

The daily concentration-weighted δ^{15}N-NH_4^+ values at the Xitou site ranged from 6.31‰ to 14.69‰, with an average of 10.95 ± 2.76‰ (Fig. 2~~2~~f, calculation details in Supplementary Description S5). ~~This~~ These result~~s~~ ~~is~~ are consistent with previous winter observations at ~~the same~~ this site (−3.7‰ to 21.39‰, with an average of 11.95 ± 2.65‰) (Chen, T. Y. et al., 2022). As shown in Fig. S5, these values ~~and~~ fall~~s~~ between those typical of urban-influenced environments (19.6‰) and remote/forest sites (~5.6‰) ~~within the range reported for both urban and remote locations, as shown in Fig. S5~~, reflecting the mixed-source characteristics of Xitou (Chen, T. Y. et al., 2022; Kawashima et al., 2023; Hall et al., 2016; Kundu et al., 2010; Moore, 1977; Proemse et al., 2012; Savard et al., 2017; Ti et al., 2018; Walters et al., 2022). ~~(~~Kawashima et al., 2023; Kundu et al., 2010; Moore, 1977) The isotopic signature is particularly comparable to other semi-rural receptor sites in East Asia that receive diluted urban plumes mixed with regional agricultural background.

Temporal patterns showed higher δ^{15}N-NH_4^+ during the clear period, with daytime and nighttime averages of 11.22 ± 2.13‰ and 12.12 ± 2.53‰, respectively (Table 1~~1~~). In contrast, lower values were ~~often~~ observed during fog, ~~decreasing from~~ including 7.35‰ (18D), ~~to~~ 6.31‰ (18N), ~~before increasing to~~ and 9.60‰ (19D). This decline of δ^{15}N during the fog likely results from three concurrent processes under stagnant conditions. First, stagnant conditions suppressed the transport of δ^{15}N-enriched urban plumes from nearby source regions. Second, continuous exchange between gas-phase NH_3 and pNH_4^+ shifts the particle phase toward the signature of the local NH_3 pool, which is depleted in δ^{15}N due to agricultural volatilization. ~~The decrease may result from the absence of fresh NH_3 input under stagnant fog conditions, allowing continuous isotopic fractionation as NH_3 converts to pNH_4^+ (Walters~~

et al., 2019). Furthermore, wet deposition during fog may remove ^{15}N-enriched particles, forcing the remaining pNH$_4^+$ to re-equilibrate with an increasingly δ^{15}N-depleted gas phase. The This observed decrease in δ^{15}N-NH$_4^+$ during the foggy period contrasts with our previous study, which reportinged a slight increases during shorter in δ^{15}N-NH$_4^+$ under foggy conditions events (< 6 hours) (Chen, T. Y. et al., 2022). The nearly double concentrations of both pNH$_4^+$ and pNO$_3^-$ in this study than in those in Chen, T. Y. et al. (2022) might indicate a stronger partition of NH$_3$ into the particle phase, leading to much lower δ^{15}N-NH$_4^+$ in this study. This discrepancy likely reflects that previous fog events, lasting only ~ 6 hours, were insufficient to permit detectable isotopic fractionation processes (Chen, T. Y. et al., 2022; Chen et al., 2021).

Table 1. Concentration-weighted isotope values (unit: ‰) under different weather circumstances.

	δ^{15}N-NH$_4^+$	δ^{15}N-NO$_3^-$	δ^{18}O-NO$_3^-$
All	10.81±2.72 (n = 15)	−2.98±1.97 (n = 14)	51.82±16.47 (n = 14)
Clear day	11.22±2.13 (n = 5)	−1.50±1.30 (n = 5)	53.74±14.99 (n = 5)
Clear night	12.12±2.53 (n = 7)	−3.46±1.67 (n = 6)	53.12±16.59 (n = 6)
Foggy 18D	7.35 (n = 1)	−2.19 (n = 1)	70.44 (n = 1)
Foggy 18N	6.31 (n = 1)	−4.80 (n = 1)	33.81 (n = 1)
Foggy 19D	9.60 (n = 1)	−6.54 (n = 1)	33.81 (n = 1)

Under clear conditions (excluding 19N and 21D), The the size-resolved δ^{15}N-NH$_4^+$ distribution patterns shown in Fig. 4 revealed a bell-shaped distribution (Fig. 4). Values peaked at ~15‰ in the accumulation mode (~0.5−2 μm) and decreased to ~7‰ in both the ultrafine and coarse particles. an increase from 7.14‰ to 14.59‰ with particle diameter up to ~ 1 μm before a decline from 16.08‰ to 7.53‰ in the coarse mode (> 1 μm), reflecting differences in particle formation and transformation processes. This pattern reflects a transition between local emissions and aged, transported aerosols. For ultrafine mode (<0.5 μm), particles maintain isotopic equilibrium with the local NH$_3$ pool, dominated by δ^{15}N-depleted residual NH$_3$ or volatilization sources (typically −28.3‰ to −17.6‰). For accumulation-mode (~0.5–2 μm), particles preserve the signatures of lower-elevation anthropogenic emission regions. Here, combustion-derived NH$_3$ (typically −8.2‰ to 1.8‰) reacts with H$_2$SO$_4$ to form non-volatile ammonium sulfate and ammonium bisulfate. Unlike ammonium nitrate, which is more volatile and easily re-equilibrates with gas-phase NH$_3$ during transport, sulfate-bound NH$_4^+$ is more resistant to isotopic re-equilibration, allowing it to act as a conservative tracer of urban source signatures during upslope transport (Wu et al., 2022). For the coarse mode (> 2 μm), particles are likely dominated by mineral dust and sea salt and present a substantially weaker thermodynamic sink for NH$_3$ absorption compared to acidic fine-mode sulfate aerosols (Fig. S6) (Pye et al., 2020). Therefore, NH$_4^+$ in this mode likely maintains a dynamic equilibrium with local gas-phase NH$_3$, which We hypothesize that fine particles with a diameter less than 1 μm were formed near the sampling site, as their lower δ^{15}N-NH$_4^+$ values are consistent with emissions from biogenic sources. becomes progressively depleted in ^{15}N as the air mass ages.

During fog, the bell-shaped distribution flattened significantly. Weakened wind suppressed the upslope transport of enriched anthropogenic pollutants, while enhanced aqueous-phase interaction promoted uniform isotopic re-equilibrium across all sizes. The high NO$_3^-$ concentration from aqueous chemistry can also promote the local isotopically depleted NH$_3$ partitioning into the particle phase, dampening the size-dependent isotopic gradient.

The flat δ^{15}N-NH$_4^+$ size distribution was also observed on 19N and 21D. For 19N, it is likely a legacy effect of the preceding fog period (18D, 18N, and 19D). The NH$_3$ pool remained isotopically depleted from sustained fog-driven scavenging and re-equilibration, and regional transport had not yet replenished the accumulation-mode signal. However, high sub-micrometer NO$_3^-$ concentration (Fig. S4) suggests that fog-like aqueous chemistry persisted, maintaining isotopic signatures similar to 18D. Conversely, the flat distribution on 21D reflects a distinct source influence. HYSPLIT back-trajectories (Fig. S7) indicate that the air parcel traveled through agricultural

regions characterized by heavily depleted NH_3 (e.g., livestock waste, −28.3‰ to −17.6‰). The partitioning of this isotopically light NH_3 during transit effectively erased the characteristic accumulation-mode enrichment. ~~On the other hand, coarse particles (1–10 μm, PM_{1-10}) are likely produced from urban areas, where HNO_3 reacts with sea salt or dust to form nitrate-rich aerosols that were subsequently transported to the sampling site. Under high RH and near-neutral pH conditions (Fig. S6), isotopic exchange between NH_4^+ in coarse-mode particles and locally available NH_3 with lower $\delta^{15}N$ may occur via aqueous-phase reactions, resulting in isotopic depletion in the coarse fraction. During the foggy period, the bell-shaped pattern became less apparent, with $\delta^{15}N$-NH_4^+ values remaining relatively uniform across particle sizes. This was likely due to suppressed gas–particle exchange under stagnant and high RH conditions, combined with elevated NH_4^+ concentrations (Fig. 3) that promoted rapid HNO_3 uptake and neutralization in the particle phase, shifting the system toward equilibrium (Walters et al., 2019; Chen, T. Y. et al., 2022). A similar uniform distribution pattern was observed on 19N and 21D, which also exhibited comparably low $\delta^{15}N$-NH_4^+ values (Fig. 2f).~~

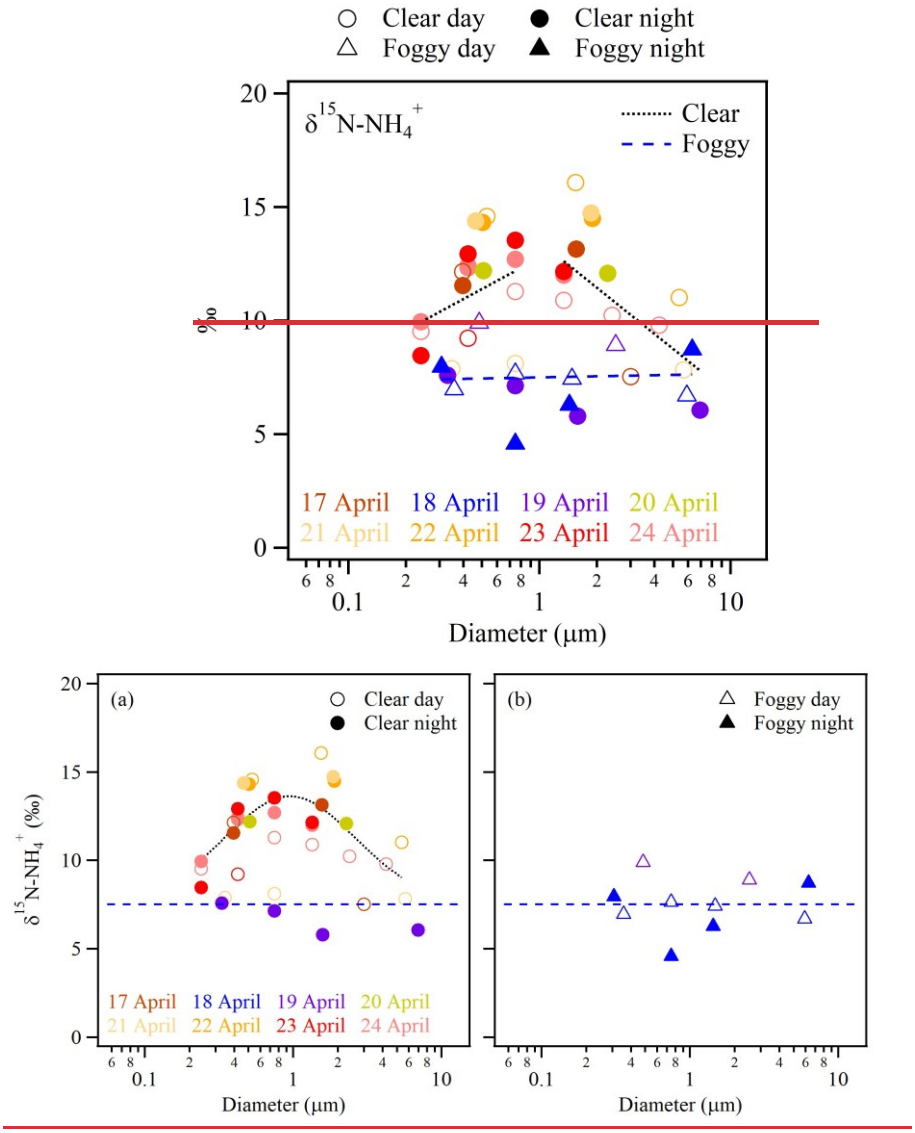

Figure 4. ~~Size-resolved isotopic composition~~ $\delta^{15}N$ of size-segregated pNH_4^+ during (a) clear and (b) foggy conditions. The dashed blue line indicates the mean $\delta^{15}N$-NH_4^+ for foggy periods. The dotted curve represents

LogNormal distribution fits for clear conditions, excluding 19N and 21D, where no distinct bell-shaped size dependence was identified. ~~**with a dotted (dashed) line indicating the linear regression trend during the clear (foggy) period.**~~

3.3.2. δ^{15}N-NH_3^0 and its source apportionment

The δ^{15}N-NH_3^0 values were derived using *f* values estimated from CMAQ-simulated NH_3 and measured pNH_4^+ concentrations (Fig. S8). The ~~derived~~ resulting δ^{15}N-NH_3^0 ranged from −12.55‰ to −6.71‰, ~~and was~~ consistently lower than the concentration-weighted δ^{15}N-NH_4^+, as shown in Fig. 5~~5~~a.~~-~~ Based on the derived δ^{15}N-NH_3^0 values and assuming a single-source contribution, NH_3 can be mainly attributed to NH_3 slip. However, because real-world ~~in real atmospheric conditions,~~ air parcels are typically influenced by a complex mixture of ~~multiple~~ emission sources ~~rather than a single dominant contributor. To quantitatively assess the contributions of different NH_3 sources to the observed particulate NH_4^+~~, the MixSIAR Bayesian framework was employed to quantitatively assess multiple source contributions~~, with the results summarized in~~ (Fig. 5~~5~~b). Overall, ~~the two~~ combustion-related sources (fossil fuel and NH_3 slip) were the dominant contributors to NH_3^0 (i.e., NH_4^+ + NH_3) in the Xitou area, accounting for 50−83% of ~~the~~ total NH_3 emissions. ~~-~~During periods with higher δ^{15}N-NH_3^0, such as 17D, 17N, and 19D, fossil fuel combustion dominated ~~contributed an average of (~~54±3%~~) to NH_3~~, followed by NH_3 slip (26±1%), waste (13±1%), and fertilizer (8±1%). In comparison, during periods with lower δ^{15}N-NH_3^0, the source contributions were more evenly distributed.~~:~~ ~~fossil~~ Fossil fuel combustion and NH_3 slip remain significant, ~~contributed~~ accounting for 30±5% and 29±1%, respectively, while the relative contributions from waste and fertilizer sources increased to 24±2% and 17±3% (Fig. S9~~8~~).~~-~~ Despite the sensitivity of $\varepsilon_{NH_4^+-NH_3}$ to temperature (Kawashima et al., 2023) and gas−particle equilibrium (Chang et al., 2025), the estimated δ^{15}N-NH_3^0 consistently yielded MixSIAR results in which combustion-related sources accounted for 88–95% of total NH_3 emission (see Supplementary Description S3 and Table S1). The persistent dominance of combustion-related sources at this~~e~~ remote mountain site, even during the stagnant fog condition, demonstrates the influence of ~~long-range~~ transport from urban and industrial areas. These findings underscore the need for regional emission control strategies targeting anthropogenic NH_3 sources, which may represent a more ~~, which represent the most efficient and~~ cost-effective mitigation strategy ~~in~~ for Taiwan, potentially yielding greater air quality benefits than ~~compared to~~ NO_x or SO_2 reductions alone (Huang, P. C. et al., 2024). It should be noted, however, that the differences in source contributions between daytime and nighttime periods, or between fog and clear conditions, remain within the overlapping ranges of the posterior distributions; consequently, the current sample number precludes statistically robust discrimination between these conditions. Expanded measurements encompassing multiple seasons and contrasting meteorological regimes would be necessary to establish whether systematic diurnal or fog-driven shifts in NH_3 source apportionment exist at this site.

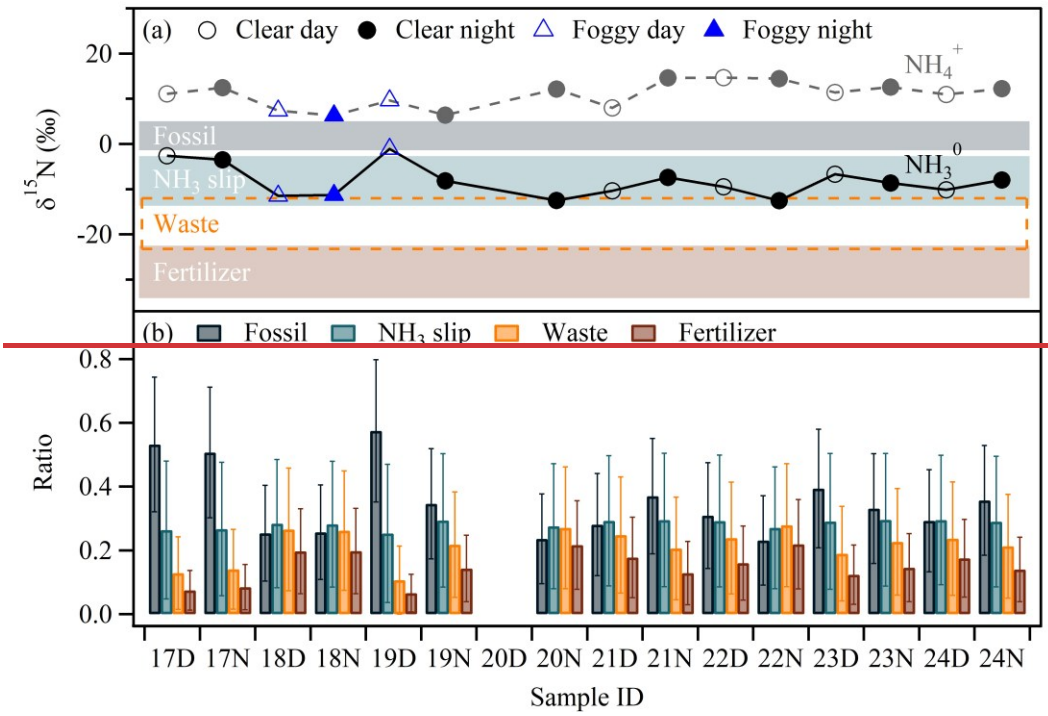

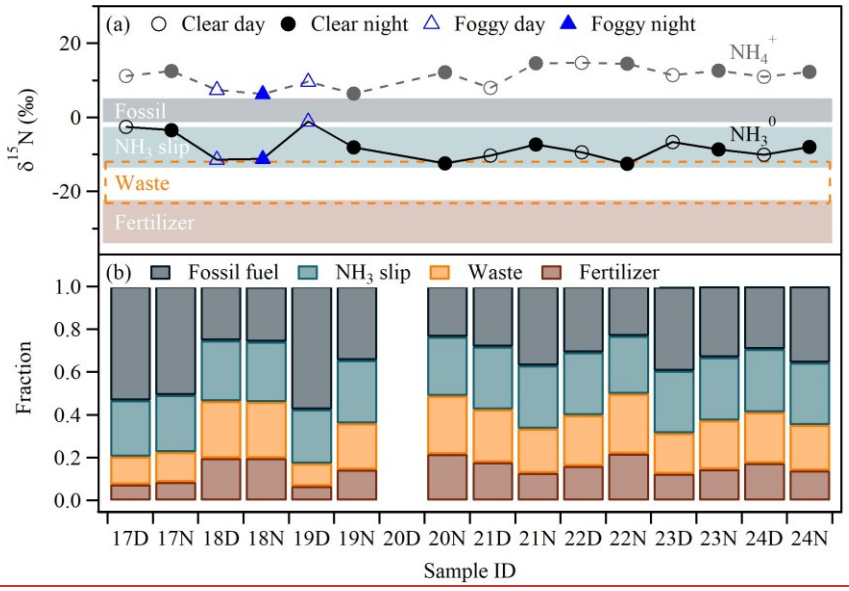

Figure 5. (a) Estimated $\delta^{15}N\text{-}NH_3^0$ at Xitou derived from measured $\delta^{15}N\text{-}NH_4^+$, and compared with the characteristic $\delta^{15}N$ ranges of NH_3 sources reported in the literature (Table S2~~1~~). (b) Source apportionment results of NH_3 from the MixSIAR framework. Uncertainties of each contribution are shown in Fig. S9.

3.4. $\delta^{15}N$ and $\delta^{18}O$ of pNO_3^-

3.4.1. $\delta^{15}N\text{-}NO_3^-$

The daily concentration-weighted $\delta^{15}N\text{-}NO_3^-$ values ranged from −6.54‰ to −0.24‰, with an average of −2.98±1.97‰ (Fig. 2~~2~~g). These values are consistent with those reported in mountain ~~regions~~ sites such as Mt. Lulin

(−3.6±3.8‰) (Guha et al., 2017) and the Himalayan-Tibetan Plateau (0.44±4.89‰) (Lin et al., 2021), as illustrated in Fig. S109. Compared to wintertime measurements at the same site (2.98±1.20‰) (Chen, T. Y. et al., 2022), these lower springtime values likely reflect seasonal shifts in NO_x sources and transport-related fractionation~~atmospheric processing~~. The depletion relative to ~~They are also significantly lower than typical~~ urban values, such as ~11.5‰ in Beijing and Gosan (Fan et al., 2020; Kundu et al., 2010), ~~indicating~~ indicates that NO_x-to-HNO_3 conversion during transport ~~long-range atmospheric transport from urban sources~~ to the mountain ~~site~~ receptors is accompanied by progressive isotopic fractionation ~~during NO_x-to-HNO_3 conversion, resulting in depletion of $\delta^{15}N$-NO_3^- values in mountain regions~~ (Freyer et al., 1993; Gobel et al., 2013).

Under clear conditions, $\delta^{15}N$-NO_3^- showed minor diurnal variation, with slightly higher values during daytime (−1.50±1.30‰) than nighttime (−3.46±1.67‰; Table ~~1~~1), likely reflecting ~~typical~~ shifts between transported urban and local biogenic NO_x sources or the depletion through deposition. During the fog, $\delta^{15}N$-NO_3^- decreased significantly from −2.19‰ (18D) to −4.80‰ (18N), and further to −6.54‰ (19D) (Fig. 2g). ~~, indicating a rapid shift in formation processes and nitrate sources. As observed for NH_4^+, t~~This decline, contrasting with ~~differs from the~~ previous shorter ~~study due to the extended~~ fog ~~duration~~ events (Chen, T. Y. et al., 2022). ~~It~~, reflects the combined effects of prolonged stagnation and a ~~isotopic partitioning between NO and NO_2, isotope fractionation during NO_x to pNO_3^- conversion, and~~ reduced ~~atmospheric transport, which limited the~~ influx of urban air. These conditions promote enhanced aqueous-phase pNO_3^- formation, predominantly driven by $\delta^{15}N$-depleted NO_x from locally derived biogenic precursors or precursors that have undergone extensive fractionation during transport ~~masses~~ (Vicars et al., 2013; Gobel et al., 2013). ~~Weak wind speeds further enhanced pNO_3^- formation in mountainous regions under high RH, where aqueous-phase reactions dominated. Simultaneously, the stagnation of air masses likely increased the relative contribution of local biogenic NO_x sources, which are typically more depleted in $\delta^{15}N$.~~

Relatively low concentration-weighted $\delta^{15}N$-NO_3^- values observed outside the fog periods on 20N and 22N, likely attributable to distinct mechanisms. For 22N, the depletion is linked to enhanced local production, supported by elevated sub-micrometer NO_3^- concentration shown in Fig. S4. For 22N, the low $\delta^{15}N$ coincides with significant deposition loss, as evidenced by low total NO_3^- levels. Because HNO_3 readily reacts with coarse-mode mineral dust and sea salt, the deposition efficiency during transport is high; this preferential removal of $\delta^{15}N$-enriched species often leaves the residual nitrate pool isotopically lower. Furthermore, the thermodynamic partitioning of HNO_3, governed by ambient temperature and particle acidity regulated by sulfate and ammonium, critically influences the observed $\delta^{15}N$. Ultimately, the observed $\delta^{15}N$ at this site serves as an integrated signal of physical and chemical dynamics processes within the air parcel during its transit.

Size-segregated $\delta^{15}N$-NO_3^- values ranged from −10.05 to 0.78‰, showing a weak positive correlation with particle diameter (Fig. ~~6~~6a). Fine particles (PM_1) had slightly lower $\delta^{15}N$-NO_3^- values (−3.59±2.38‰) compared to larger, coarse-mode particles (PM_{1-10}, −2.07±2.10‰), a trend consistent with ~~our~~ previous findings (Chen, T. Y. et al., 2022). This ~~pattern~~ size-dependent distribution likely reflects isotopic fractionation occurring during HNO_3 formation and its subsequent partitioning across different size modes. In environments (nearby coast) proximal to ~~urban areas near~~ major NO_x sources, HNO_3 may~~ight~~ react preferentially with coarse-mode particles (e.g., NaCl or mineral dust), forming $\delta^{15}N$-enriched pNO_3^-. The ~~remaining~~ residual NO_x~~,~~ pool, consequently ~~which is~~ depleted in $\delta^{15}N$, subsequently forms HNO_3 that condenses onto fine-mode particles as they undergo transport toward~~formed near~~ the sampling site (Gobel et al., 2013). However, it is important to note that the complex physical and chemical dynamic processes within the air parcel during its transit, as detailed above, may diminish these distinct isotopic signatures under varying daily meteorological conditions. ~~Additionally, fine-mode pNO_3^- typically forms through gas-phase oxidation of NO_x followed by HNO_3 condensation under sufficient NH_3, preserving the $\delta^{15}N$-depleted signature of precursor gases. In contrast, coarse-mode pNO_3^- often forms through heterogeneous reactions of NO_2 or HNO_3 on particle surfaces near the emission sources, which preferentially enrich heavier isotopes.~~

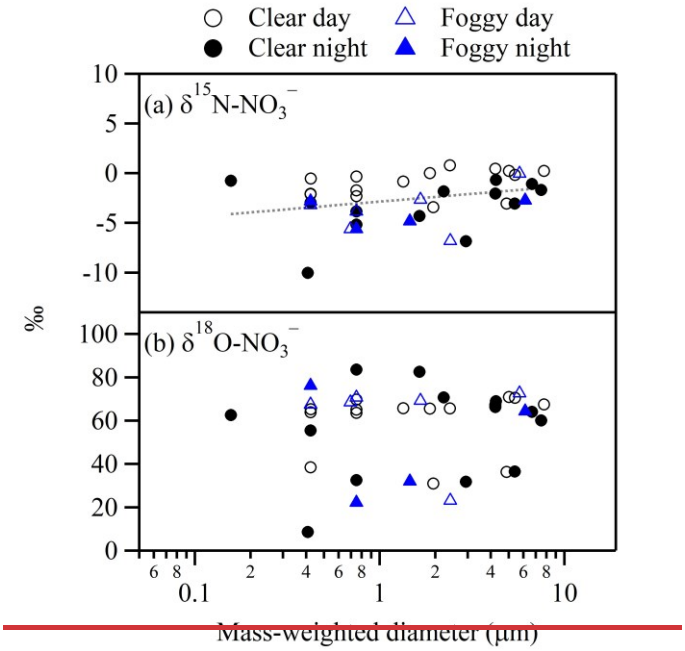

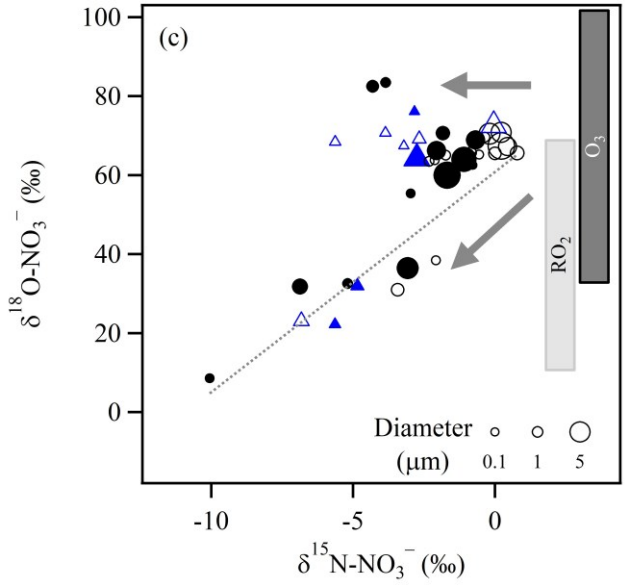

~~**Figure 6. Size-resolved isotopic composition of pNO_3^-. (a) $\delta^{15}N\text{-}NO_3^-$ values as a function of mass-weighted particle diameter, with a dotted line indicating the linear regression trend. (b) $\delta^{18}O\text{-}NO_3^-$ values as a function of mass-weighted particle diameter. (c) Two-dimensional plot of $\delta^{15}N$ versus $\delta^{18}O$ across particle sizes. The dotted line provides a visual guide to possible source groupings. The gray boxes labeled "RO_2" and "O_3" indicate the potential $\delta^{18}O\text{-}NO_3^-$ ranges resulting from reactions with RO_2 and O_3, respectively.**~~

3.4.2. Using $\delta^{18}O\text{-}NO_3^-$ to estimate ~~C~~contributions of pNO_3^- formation pathways

The daily concentration-weighted $\delta^{18}O\text{-}NO_3^-$ ranged from 30.98 to 73.27‰, with an average value of 51.82±16.47‰ (Fig. 2~~2~~h). Similar to $\delta^{15}N\text{-}NO_3^-$, ~~These~~ these values ~~are lower than our previous winter observations (72.66±3.42‰) (Chen, T. Y. et al., 2022), but~~ align with measurements from other mountain regions such as 10.8−92.4‰ at Mt. Lulin (Guha et al., 2017) and 64.71±11.52‰ at the Himalayan-Tibetan Plateau (Lin et al., 2021),

but are lower than previous winter observations (72.66±3.42‰) (Chen, T. Y. et al., 2022), as illustrated in Fig. S11~~0~~. In contrast, $\delta^{18}O\text{-}NO_3^-$ at urban sites such as Changchun (68.16±9.52‰) and Beijing (83.8±13.4‰) are substantially higher, consistent with O_3-dominated oxidation under polluted conditions. The relatively lower $\delta^{18}O\text{-}NO_3^-$ values at Xitou and other mountain sites suggest that RO_2-initiated pathways contribute more substantially to nitrate formation under less-polluted conditions. A sharp decrease in $\delta^{18}O\text{-}NO_3^-$ from 70.44‰ (18D) to 33.81‰ (18N and 19D) occurred during the fog, coinciding with $\delta^{15}N\text{-}NO_3^-$ depletion. ~~These declines indicate a~~ This shift from O_3- to RO_2-dominated oxidation, is likely driven by stagnant winds, suppressed urban input, and enhanced local aqueous-phase chemistry under high RH.

Notably, no significant systematic size-dependent trend of $\delta^{18}O\text{-}NO_3^-$ on particle size was observed (Fig. 6b). The spatial heterogeneity of oxidants (O_3 and RO_2), coupled with the complex HNO_3 partitioning dynamics within the air parcel, likely erases any size-dependent isotopic pattern and daily variation. However, the $\delta^{15}N\text{-}NO_3^-$ vs. $\delta^{18}O\text{-}NO_3^-$ relationship (Fig. 6c, S12, and S13) resolves two geochemically distinct regimes reflecting contrasting formation environments and aerosol histories. The

~~A fair correlation (r = 0.66) between $\delta^{18}O\text{-}NO_3^-$ and $\delta^{15}N\text{-}NO_3^-$ highlights the interplay between oxidation processes and nitrogen cycling. As shown in Fig. 6c, two distinct regimes emerge: particles with~~ higher $\delta^{18}O\text{-}NO_3^-$ (55−83‰) ~~exhibit~~ with enriched $\delta^{15}N\text{-}NO_3^-$ (−6 to 1‰) can be assigned as an urban/transported regime. Freshly emitted in metropolitan areas contributed to elevated $\delta^{15}N$, while O_3-driven oxidation leads to high $\delta^{18}O$ (Gobel et al., 2013). The observed ~~those with~~ lower $\delta^{18}O\text{-}NO_3^-$ (9−38‰) ~~tend to have~~ and depleted $\delta^{15}N\text{-}NO_3^-$ (−10 to −2‰) is assigned as a rural/fog regime. These signatures reflect RO_2-initiated oxidation and $\delta^{15}N$-depleted NO_x from locally derived biogenic precursors or after extensive fractionation during transport, particularly under stagnant conditions. A ~~fair~~moderate positive correlation (r = 0.66) between $\delta^{18}O\text{-}NO_3^-$ and $\delta^{15}N\text{-}NO_3^-$ further highlights the intrinsic interplay between oxidation processes and nitrogen cycling at the site. These data demonstrate a $\delta^{18}O\text{-}NO_3^-$ and $\delta^{15}N\text{-}NO_3^-$ relationship that covers a broad isotopic range, spanning from the signatures observed at the Himalayan-Tibetan Plateau to those at regional background sites like Mt. Lulin (Fig. S14). ~~Considering the evolution of air parcels from urban to rural regions, particles with the highest $\delta^{15}N\text{-}NO_3^-$ (~ 0‰) and $\delta^{18}O\text{-}NO_3^-$ (~ 70‰) likely form in metropolitan areas, where freshly emitted NO contributes to elevated $\delta^{15}N\text{-}NO_3^-$ (Gobel et al., 2013), and O_3-driven oxidation (pathways PXb, Fig. S3) leads to higher $\delta^{18}O\text{-}NO_3^-$. During atmospheric transport from urban to mountainous areas, $\delta^{15}N\text{-}NO_3^-$ values gradually decrease from ~ 0‰ to −6‰ due to isotopic fractionation (Gobel et al., 2013), while $\delta^{18}O\text{-}NO_3^-$ values remain elevated (~ 60−80‰) because O_3-driven oxidation continues to dominate in the O_3-rich urban plumes. This intermediate regime represents particles formed during the transport process, maintaining the O_3 signature while experiencing nitrogen isotopic depletion. On the other hand, particles with the lowest $\delta^{15}N\text{-}NO_3^-$ (−10 to −2‰) and $\delta^{18}O\text{-}NO_3^-$ (9−38‰) likely form in rural mountainous regions, where oxidation pathways involving RO_2 (pathways PXa, Fig. S3) result in lower $\delta^{18}O\text{-}NO_3^-$. The lower $\delta^{15}N\text{-}NO_3^-$ values may result from continued isotopic depletion during NO_x transport and the increased contributions from $\delta^{15}N$-depleted biogenic emissions, especially under stagnant fog conditions.~~

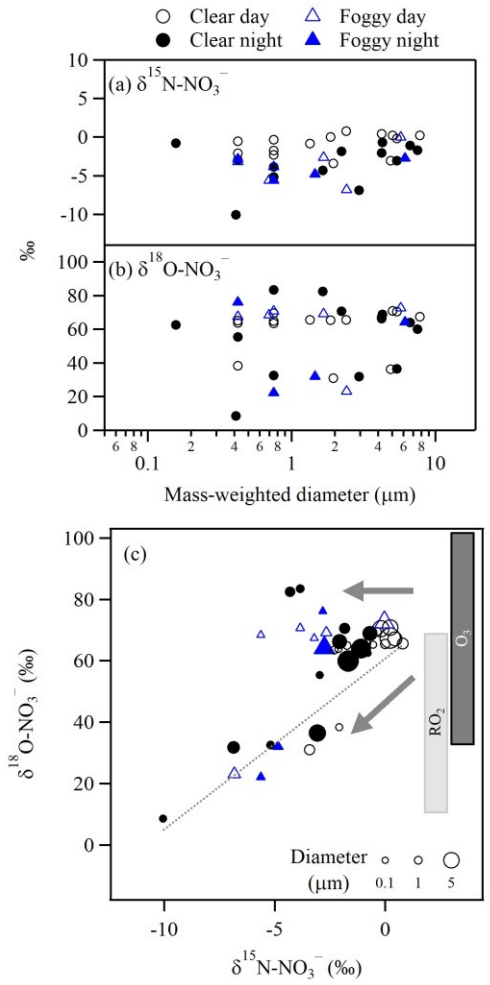

Figure 6. Size-resolved isotopic composition of pNO_3^-. (a) $\delta^{15}N\text{-}NO_3^-$ values as a function of mass-weighted particle diameter~~, with a dotted line indicating the linear regression trend~~. (b) $\delta^{18}O\text{-}NO_3^-$ values as a function of mass-weighted particle diameter. (c) Two-dimensional plot of $\delta^{15}N$ versus $\delta^{18}O$ across particle sizes. The dotted line provides a visual guide to possible source groupings. The gray boxes labeled "RO_2" and "O_3" indicate the potential $\delta^{18}O\text{-}NO_3^-$ ranges resulting from reactions with RO_2 and O_3, respectively.

~~The daily $\delta^{18}O\text{-}NO_3^-$ and $\delta^{15}N\text{-}NO_3^-$ relationship depicted in Fig. S11 and Fig. S12 further illustrates this evolution, exhibiting a shift toward lower isotopic values during the fog period, then increasing to higher values as transport resumed. The observed positive correlation between $\delta^{15}N\text{-}NO_3^-$ and $\delta^{18}O\text{-}NO_3^-$ is consistent with previous studies (Chang et al., 2018; Chen, T. Y. et al., 2022; Fan et al., 2020; Guha et al., 2017; Hall et al., 2016; Lin et al., 2021; Proemse et al., 2012; Savard et al., 2017; Vicars et al., 2013; Zhao et al., 2020), which have shown that higher $\delta^{15}N\text{-}NO_3^-$ and $\delta^{18}O\text{-}NO_3^-$ values are typically associated with polluted urban environments, while lower values are more common in less polluted regions (Fig. S13). Finer size-resolved measurements can reveal the evolution of nitrate formation as air masses move from emission source regions to rural sites. A quantitative analysis of pNO_3^- formation is provided in the following section.~~

~~3.4.3. Contributions of pNO_3^- formation pathways~~

Formation pathways of pNO_3^- were quantitatively analyzed using the MixSIAR framework based on $\delta^{18}O\text{-}NO_3^-$ values, as shown in Fig. ~~S7714a~~. ~~In the daytime~~During daytime periods characterized by low $\delta^{18}O\text{-}NO_3^-$

values (31−41‰) and low CO concentrations (< 0.22ppm, 17D, 19D, and 23D), ~~,~~ $P_{RO_2\text{-}OH1}$~~the RO_2 initiated P1a (RO_2 + NO → NO_2, followed by NO_2 + ·OH → HNO_3, Fig. S3)~~ accounted for ~~over~~ 82−92% of pNO_3^- formation ~~on 17D, 19D, and 23D~~ (Figs. ~~S~~7~~7~~14a and ~~7~~7b). These conditions are consistent with periods ~~were characterized by low $\delta^{18}O\text{-}NO_3^-$ values (31−41‰) and low CO concentrations (< 0.22ppm, Fig. S15), suggesting~~with limited influence from urban air masses, suggesting ~~and~~ the dominance of local RO_2 oxidation processes. In contrast, during daytime with higher $\delta^{18}O\text{-}NO_3^-$ values (63−70‰) and to elevated CO concentrations (0.24−0.27 ppm, 18D, 21D, 22D), the dominant pathways shifted toward ~~, such as 18D, 21D, 22D, and 24D,~~ $P_{RO_2\text{-}OH2}$~~P2a~~, $P_{O_3\text{-}OH1}$~~P1b~~, and $P_{O_3\text{-}OH2}$~~P2b were the dominant formation pathways~~, contributing an average of 29±1%, 27±3%, and 28±5%, respectively. This shift could probably reflect the enhanced transport of urban air masses enriched in O_3 and NO_x precursors.~~Except for 24D where CO concentration was 0.20 ppm, these days corresponded to elevated CO concentrations (0.24−0.27 ppm, Fig. S15), suggesting enhanced transport of urban pollutants.~~

~~At~~ Although nighttime~~,~~ ~~the~~ nitrate formation ~~of pNO_3^-~~ is theoretically dominated by heterogeneous reactions, our results reveal a~~became~~ more complex process. On nights with elevated $\delta^{18}O\text{-}NO_3^-$ values, heterogeneous pathways ($P_{RO_2\text{-}het}$ and $P_{O_3\text{-}het}$) were the dominant contributors, accounting for 33±6% and 47±9% of pNO_3^- formation on 19N, 21N, 23N. In contrast, on nights with lower $\delta^{18}O\text{-}NO_3^-$ values (32−43‰, 17N, 18N, 20N, and 22N), ~~-~~$P_{RO_2\text{-}OH1}$ ~~P1a~~ remained a major contributor, ~~which~~ accounting~~ed~~ for 80−94% of ~~pNO_3^-~~ formation ~~on several nights (17N, 18N, 20N, and 22N). This high $P_{RO_2\text{-}OH1}$ might stem from the residual pNO_3^- from daytime, or when $\delta^{18}O\text{-}NO_3^-$ values were lower (32−43‰). Th~~nighttime ~~e presence of P1a during nighttime likely resulted from residual ·OH produced during the daytime or from non-photolytic~~ ·OH generated ~~ion~~ via reactions between O_3 and alkenes ~~or~~ /terpenes (Kroll et al., 2001; Aschmann et al., 2002). The weak night-to-night covariation between $\delta^{18}O\text{-}NO_3^-$ and CO concentrations further suggests that nighttime nitrate isotope signatures are governed by the interplay among fog processing, reduced advection, and heterogeneous chemistry, rather than transport intensity alone.

~~During the periods with elevated $\delta^{18}O\text{-}NO_3^-$ values (19N, 21N, 23N, $\delta^{18}O\text{-}NO_3^-$ values ranging from 65 to 73‰), pathways P3a and P3b became the dominant contributors, accounting for 33±6% and 47±9% of pNO_3^- formation, respectively. The complexity in formation pathways, as well as weaker wind speed and relatively lower CO concentration, may lead to a weaker correlation between $\delta^{18}O\text{-}NO_3^-$ values and CO concentrations during nighttime.~~

~~During the fog, a~~ A distinct shift in nitrate formation pathways was observed during the fog. On 18D, ~~consistent with~~ high $\delta^{18}O\text{-}NO_3^-$ values (70‰) and elevated ~~pollutant concentrations (~~CO~~:~~ concentrations (0.24 ppm) were associated with the dominance of ~~, the dominant formation pathways were~~ $P_{RO_2\text{-}OH2}$~~P2a~~ (30±20%) and $P_{O_3\text{-}OH2}$~~P2b~~ (36±16%), indicating that O_3 from transported urban precursors remained active (Fig. S15).~~-~~ As fog intensified during 18N and persisted into 19D, $\delta^{18}O\text{-}NO_3^-$ values decreased sharply to ~34‰, and ~~the dominant pathway shifted to~~ $P_{RO_2\text{-}OH1}$~~P1a~~ became dominant (93±5% on 18N, and 90±5% on 19D). This transition is driven by two coupled effects: (1) the attenuation of incoming solar radiation suppresses O_3 photolysis and thereby reduces the availability of high-$\delta^{18}O$ oxidants, and (2) the scavenging of long-range transport by wet deposition diminishes the influx of urban NO_x and O_3. Together, these foggy conditions favor locally derived low-$\delta^{18}O$ RO_2 cycling as the predominant oxidant driving nitrate formation.

~~This transition reflects the suppression of long-range transport and O_3 photochemistry by the fog, leading to conditions favorable for local RO_2-driven oxidation.~~Distinguishing the relative contributions helps clarify how nitrate formation processes vary with air mass origin, photochemical activity, and fog processing, which is directly relevant to emission control strategies since the efficacy of nitrate reduction depends on the dominant oxidation pathway. At the global scale, model estimated that the NO_2 + ·OH (same as our $P_{O_3\text{-}OH1}$/$P_{O_3\text{-}OH2}$) and N_2O_5 hydrolysis (same as our $P_{RO_2\text{-}het}$/$P_{O_3\text{-}het}$) pathways each contributed approximately 41% to tropospheric nitrate formation (Alexander et al., 2020), while observation studies in both urban and mountain environments suggest that heterogeneous pathways become more important for nitrate formation under elevated pollution levels (Fan et al.,

2020; Lin et al., 2021). The pathway apportionment presented here provides finer resolution than bulk gas-phase/heterogeneous partitioning by explicitly distinguishing RO_2- from O_3-initiated formation, which can be useful in regions where RO_2 oxidation dominates. However, given the limited number of sampling days in this campaign, the relationship between nitrate formation pathways and pollution intensity warrants further investigation across seasons and contrasting meteorological conditions.

Beyond inorganic HNO_3 formation, the total particulate nitrogen budget includes particulate organic nitrate (*p*ON) species, which can account for 17−31% of total particulate nitrogen (Yu et al., 2024) in mixed urban-biogenic environments, and up to 50% observed in urban plumes (Murphy et al., 2025). *p*ON forms via the reaction of NO with RO_2 ($NO + RO_2 \rightarrow RONO_2$) during the day, and NO_3 with alkenes and biogenic VOC at night ($NO_3 + R \rightarrow RONO_2$) (Murphy et al., 2025; Ward et al., 2025; Guo et al., 2024). These mechanisms operate through the same RO_2- and NO_3-driven pathways identified here ($P_{RO_2\text{-}OH1}$ / $P_{RO_2\text{-}OH2}$ and $P_{RO_2\text{-}het}$/$P_{O_3\text{-}het}$, respectively), suggesting that the oxidation chemistry inferred from $\delta^{18}O\text{-}NO_3^-$ signatures at Xitou also drives concurrent *p*ON production. Because isotope analysis in this study assumes TN comprises only NO_3^- and NH_4^+, organic nitrogen contribution could bias the derived $\delta^{15}N\text{-}NH_4^+$ toward the signature of *p*ON. While this was partially mitigated by excluding samples with low $[NH_4^+]$ (<60% of ([TN]−[NN])), future research should prioritize direct $\delta^{15}N\text{-}NH_4^+$ measurement, which would enable the estimation of organic nitrate isotopes via residual mass balance (i.e., $[ON] = [TN] - [NH_4^+] - [NO_3^-]$) and provide a more complete characterization of the Nr budget in mountain forest environments.

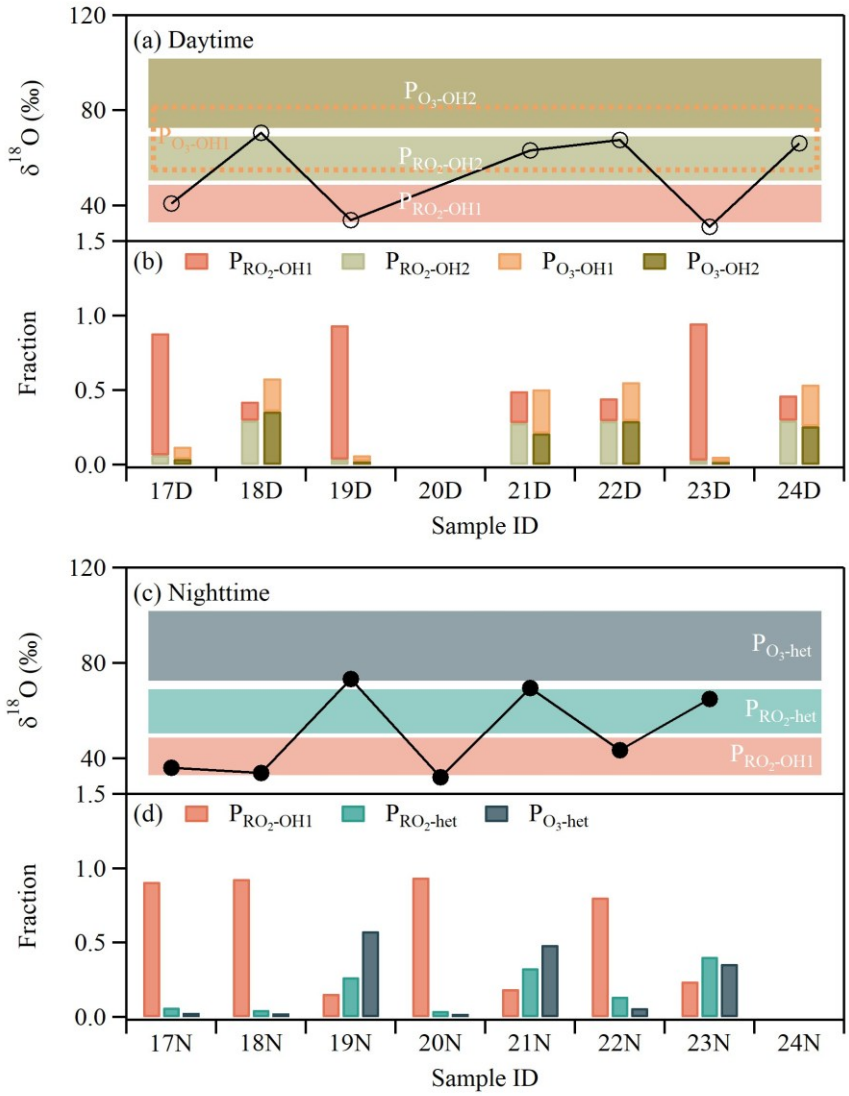

Figure 7. Contributions of nitrate formation pathways estimated by MixSIAR. (a, c) Measured $\delta^{18}O\text{-}NO_3^-$ values with the corresponding $\delta^{18}O$ ranges of potential formation pathways. (b, d) estimated fractional contributions of these pathways.

4. Conclusions

Our observations in a subtropical mountain forest in Taiwan revealed evident diurnal and meteorological influences on the transport and transformation of reactive nitrogen (Nr). Daytime particle concentrations consistently exceeded nighttime levels, reflecting upslope transport of urban plumes, while a 26-hour fog event suppressed urban input and enhanced local transformation processes. During the prolonged fog, progressive decreases in $\delta^{15}N\text{-}NH_4^+$ and $\delta^{15}N\text{-}NO_3^-$ values indicated ~~continued~~ sustained isotopic depletion on the particle phase due to partitioning of species from the isotopically depleted gas phase, combining with the preferential wet depletion of the earlier-formed $\delta^{15}N$-enriched particles~~fractionation~~ under stagnant conditions. Simultaneously, $\delta^{18}O\text{-}NO_3^-$ values shifted markedly, suggesting a transition from O_3- to RO_2-dominated pNO_3^- formation pathways. Unlike previous studies of shorter fog episodes, this extended fog allowed more precise identification of isotopic fractionation dynamics and nitrate evolution pathways.

Under clear conditions, size-resolved $\delta^{15}N\text{-}NH_4^+$ exhibited a bell-shaped distribution, peaking at ~15‰ in the accumulation mode (~0.5–2 μm) and decreasing to ~7‰ in both the ultrafine and coarse fractions. This pattern reflects a transition between local isotopically light NH_3 and conservative transport of combustion-derived, sulfate-bound NH_4^+ from urban source regions. During fog, this size-dependent gradient flattened as weakened winds suppressed advection and enhanced aqueous-phase re-equilibration across all size bins. Concurrently, size-resolved $\delta^{15}N\text{-}NO_3^-$ and $\delta^{18}O\text{-}NO_3^-$ patterns further revealed two distinct pNO_3^- formation regimes: one associated with ~~Size-resolved $\delta^{15}N\text{-}NO_3^-$ and $\delta^{18}O\text{-}NO_3^-$ patterns further revealed two distinct pNO_3^- formation regimes: one associated with long-range~~ transport from urban plumes under ~~O_3~~ O_3 oxidation, and another linked to local RO_2-driven processes with greater isotopic depletion and biogenic contributions.

Bayesian source apportionment based on $\delta^{15}N\text{-}NH_3$~~0~~ constraints ~~indicated~~ indicates that combustion-related emissions contributed 50–83% of ~~the~~ total NH_3, a finding that remained robust (88–95% in sensitivity tests) across varying meteorological conditions~~even under stagnant, foggy periods when fresh urban inputs were limited.~~. This persistent anthropogenic signature highlights the resilience of combustion sources in shaping local nitrogen budgets and underscores the potential for regional emission control strategies targeting anthropogenic NH_3, which represent a highly efficient mitigation for $PM_{2.5}$ reduction in Taiwan.~~.~~ Furthermore, ~~Isotopic~~ isotopic analysis of $\delta^{18}O\text{-}NO_3^-$ ~~further~~ revealed that RO_2-initiated oxidation accounted for 42–95% of daytime pNO_3^- formation and remained ~~as a~~ substantial ~~contributor~~ at night, ~~when~~ with heterogeneous reactions ~~accounted~~ accounting for 6–84% ~~of total pNO_3^- formation~~. These findings highlight the significance of RO_2 chemistry in nitrate formation, particularly in forested, high-humidity environments where biogenic VOC emissions promote RO_2 radical production.

Despite these insights, certain methodological uncertainties remain. Estimation of $\delta^{15}N\text{-}NH_3$ from particulate $\delta^{15}N\text{-}NH_4^+$ relied on simplified equilibrium fractionation assumptions that may underestimate kinetic effects ~~during gas–particle conversion~~, potentially ~~skewing~~ biasing source attribution toward combustion-related NH_3 sources. ~~Similarly~~Furthermore, ~~the~~ overlapping isotopic signatures ~~of NO_x to pNO_3^-~~ complicate ~~efforts~~ the ~~to~~ isolat~~e~~ion of individual NO_x to pNO_3^- oxidation ~~processes~~pathways. As these conclusions reflect processes observed during a one-week spring campaign, expanded measurements across multiple seasons and meteorological regimes would be needed to establish climatological representativeness. Future studies should integrate direct gas-phase isotope observations, chamber studies of aqueous-phase reactions, and region-specific source inventories to refine isotopic models. Such advancements will improve the differentiation between urban and biogenic contributions, thereby enabling a more rigorous ~~our ability to distinguish urban versus biogenic contributions, assess the role of local photochemistry, and~~ evaluation of ~~evaluate~~ the effectiveness of targeted emission reduction strategies.

Code availability. Codes are available upon request.

Data availability. Data are available upon request.

Sample availability. Samples are no longer available due to full consumption during analytical procedures.

Author contribution.

WCL: data curation, formal analysis, MixSIAR analysis, visualization, writing original draft; **MHH:** laboratory experiments, data curation, formal analysis; **WCH:** field observations, filter sample collection, laboratory experiments, data curation; **JPC:** CMAQ modeling and analysis; **YJL:** meteorological data collection; **HR:** supervision of isotope measurements and analysis; **HMH:** project design, project supervision, data discussion, manuscript review and editing. ~~HMH designed the project. WCH conducted the field observations and collected filter samples. MHH and WCH carried out the laboratory experiments. MHH, WCH, and WCL contributed to data curation. MHH and WCL performed the formal analysis. JPC conducted the CMAQ modeling and analysis. YJL collected the meteorological data. HR supervised the isotope measurements and analysis. WCL performed MixSIAR analysis, prepared the visualizations, and wrote the original draft. HMH supervised the project, led data discussions, and revised the manuscript.~~ All authors approved the final version of the manuscript.

Competing interests. The authors declare that they have no conflict of interest.

Disclaimer. Copernicus Publications remains neutral with regard to jurisdictional claims in published maps and institutional affiliations.

Acknowledgments. The authors acknowledge Hsu-Hung Lee and Ting-Yu Chen for their assistance with field observations, filter sampling, and preliminary data analysis. We also thank Prof. Jr-Chuan Huang from the Department of Geography, National Taiwan University, for IC instrumentation support, and the administration of the Xitou Experimental Forest, College of Bio-Resources and Agriculture, National Taiwan University, for local site support. AI tools (ChatGPT, Gemini, and Claude) were used to improve the clarity of language; all scientific content was developed and verified by the authors.

Financial support. This study was supported by the National Science and Technology Council of Taiwan (Grant Nos. 112-2111-M-002-014, ~~and~~ 113-2111-M-002-012, and 114-2111-M-002-014). W.-C. Lee received support from the National Science and Technology Council of Taiwan (Grant Nos. 113-2811-M-002-114 and 114-2811-M-002-083).

References

Alexander, B., Sherwen, T., Holmes, C. D., Fisher, J. A., Chen, Q., Evans, M. J., and Kasibhatla, P.: Global inorganic nitrate production mechanisms: comparison of a global model with nitrate isotope observations, Atmos. Chem. Phys., 20, 3859-3877, https://doi.org/10.5194/acp-20-3859-2020, 2020.

Aschmann, S. M., Arey, J., and Atkinson, R.: OH radical formation from the gas-phase reactions of O_3 with a series of terpenes, Atmos. Environ., 36, 4347-4355, https://doi.org/10.1016/S1352-2310(02)00355-2, 2002.

Böhlke, J. K., Mroczkowski, S. J., and Coplen, T. B.: Oxygen isotopes in nitrate: new reference materials for ^{18}O:^{17}O:^{16}O measurements and observations on nitrate-water equilibration, Rapid Commun. Mass Spectrom., 17, 1835-1846, https://doi.org/10.1002/rcm.1123, 2003.

Chang, Y., Zhang, Y., Wang, Q., Shao, S., Bao, M., Zhang, C., and Lehmann, M. F.: Nitrogen isotope fractionation associated with ammonia gas-to-aerosol conversion and implications for determining isotopic source signatures and tracing atmospheric ammonium origins, Environ. Sci. Technol., 59, 22110-22121, https://doi.org/10.1021/acs.est.5c11271, 2025.

Chang, Y., Zhang, Y., Tian, C., Zhang, S., Ma, X., Cao, F., Liu, X., Zhang, W., Kuhn, T., and Lehmann, M. F.: Nitrogen isotope fractionation during gas-to-particle conversion of NO_x to NO_3^- in the atmosphere – implications for isotope-based NO_x source apportionment, Atmos. Chem. Phys., 18, 11647-11661, https://doi.org/10.5194/acp-18-11647-2018, 2018.

Chen, C.-L., Chen, T.-Y., Hung, H.-M., Tsai, P.-W., Chou, C. C. K., and Chen, W.-N.: The influence of upslope fog on hygroscopicity and chemical composition of aerosols at a forest site in Taiwan, Atmos. Environ., 246, 118150, https://doi.org/10.1016/j.atmosenv.2020.118150, 2021.

Chen, T. Y., Chen, C. L., Chen, Y. C., Chou, C. C. K., Ren, H., and Hung, H. M.: Source apportionment and evolution of N-containing aerosols at a rural cloud forest in Taiwan by isotope analysis, Atmos. Chem. Phys., 22, 13001-13012, https://doi.org/10.5194/acp-22-13001-2022, 2022.

Chen, Z.-L., Song, W., Hu, C.-C., Liu, X.-J., Chen, G.-Y., Walters, W. W., Michalski, G., Liu, C.-Q., Fowler, D., and Liu, X.-Y.: Significant contributions of combustion-related sources to ammonia emissions, Nat. Commun., 13, 7710, https://doi.org/10.1038/s41467-022-35381-4, 2022.

Dubey, M. K., Mohrschladt, R., Donahue, N. M., and Anderson, J. G.: Isotope specific kinetics of hydroxyl radical (OH) with water (H_2O): Testing models of reactivity and atmospheric fractionation, J. Phys. Chem. A, 101, 1494-1500, https://doi.org/10.1021/jp962332p, 1997.

Ervens, B.: Modeling the processing of aerosol and trace gases in clouds and fogs, Chem. Rev., 115, 4157-4198, https://doi.org/10.1021/cr5005887, 2015.

Fan, M.-Y., Zhang, Y.-L., Lin, Y.-C., Cao, F., Zhao, Z.-Y., Sun, Y., Qiu, Y., Fu, P., and Wang, Y.: Changes of emission sources to nitrate aerosols in Beijing after the clean air actions: Evidence from dual isotope compositions, J. Geophys. Res.: Atmos., 125, e2019JD031998, https://doi.org/10.1029/2019JD031998, 2020.

Freyer, H. D., Kley, D., Volz-Thomas, A., and Kobel, K.: On the interaction of isotopic exchange processes with photochemical reactions in atmospheric oxides of nitrogen, J. Geophys. Res.: Atmos., 98, 14791-14796, https://doi.org/10.1029/93JD00874, 1993.

Galloway, J. N., Townsend, A. R., Erisman, J. W., Bekunda, M., Cai, Z., Freney, J. R., Martinelli, L. A., Seitzinger, S. P., and Sutton, M. A.: Transformation of the nitrogen cycle: Recent trends, questions, and potential solutions, Science, 320, 889-892, https://doi.org/doi:10.1126/science.1136674, 2008.

Gobel, A. R., Altieri, K. E., Peters, A. J., Hastings, M. G., and Sigman, D. M.: Insights into anthropogenic nitrogen deposition to the North Atlantic investigated using the isotopic composition of aerosol and rainwater nitrate, Geophys. Res. Lett., 40, 5977-5982, https://doi.org/10.1002/2013GL058167, 2013.

Gong, C., Tian, H., Liao, H., Pan, N., Pan, S., Ito, A., Jain, A. K., Kou-Giesbrecht, S., Joos, F., Sun, Q., Shi, H., Vuichard, N., Zhu, Q., Peng, C., Maggi, F., Tang, F. H. M., and Zaehle, S.: Global net climate effects of anthropogenic reactive nitrogen, Nature, 632, 557-563, https://doi.org/10.1038/s41586-024-07714-4, 2024.

Guha, T., Lin, C. T., Bhattacharya, S. K., Mahajan, A. S., Ou-Yang, C.-F., Lan, Y.-P., Hsu, S. C., and Liang, M.-C.: Isotopic ratios of nitrate in aerosol samples from Mt. Lulin, a high-altitude station in Central Taiwan, Atmos. Environ., 154, 53-69, https://doi.org/10.1016/j.atmosenv.2017.01.036, 2017.

Guo, F., Bui, A. A. T., Schulze, B. C., Dai, Q., Yoon, S., Shrestha, S., Wallace, H. W., Sanchez, N. P., Alvarez, S., Erickson, M. H., Sheesley, R. J., Usenko, S., Flynn, J., and Griffin, R. J.: Airmass history, night-time particulate organonitrates, and meteorology impact urban SOA formation rate, Atmos. Environ., 322, 120362, https://doi.org/10.1016/j.atmosenv.2024.120362, 2024.

Haagen-Smit, A. J., Bradley, C. E., and Fox, M. M.: Ozone formation in photochemical oxidation of organic substances, Ind. Eng. Chem., 45, 2086-2089, https://doi.org/10.1021/ie50525a044, 1953.

Hall, S. J., Ogata, E. M., Weintraub, S. R., Baker, M. A., Ehleringer, J. R., Czimczik, C. I., and Bowling, D. R.: Convergence in nitrogen deposition and cryptic isotopic variation across urban and agricultural valleys in northern Utah, J. Geophys. Res.: Biogeosci., 121, 2340-2355, https://doi.org/10.1002/2016JG003354, 2016.

Hastings, M. G., Sigman, D. M., and Lipschultz, F.: Isotopic evidence for source changes of nitrate in rain at Bermuda, J. Geophys. Res.: Atmos., 108, 4790, https://doi.org/10.1029/2003JD003789, 2003.

Heaton, T. H. E., Spiro, B., and Robertson, S. M. C.: Potential canopy influences on the isotopic composition of nitrogen and sulphur in atmospheric deposition, Oecologia, 109, 600-607, https://doi.org/10.1007/s004420050122, 1997.

Holmes, R. M., Aminot, A., Kérouel, R., Hooker, B. A., and Peterson, B. J.: A simple and precise method for measuring ammonium in marine and freshwater ecosystems, Can. J. Fish. Aquat. Sci., 56, 1801-1808, https://doi.org/10.1139/f99-128, 1999.

Huang, P. C., Hung, H. M., Lai, H. C., and Chou, C. C. K.: Assessing the effectiveness of SO_2, NO_x, and NH_3 emission reductions in mitigating winter $PM_{2.5}$ in Taiwan using CMAQ, Atmos. Chem. Phys., 24, 10759-10772, https://doi.org/10.5194/acp-24-10759-2024, 2024.

Huang, W. C., Hung, H. M., Chu, C. W., Hwang, W. C., and Lung, S. C. C.: Deriving the hygroscopicity of ambient particles using low-cost optical particle counters, Atmos. Meas. Tech., 17, 6073-6084, https://doi.org/10.5194/amt-17-6073-2024, 2024.

Kawashima, H., Yoshida, O., and Suto, N.: Long-term source apportionment of ammonium in $PM_{2.5}$ at a suburban and a rural site using stable nitrogen isotopes, Environ. Sci. Technol., 57, 1268-1277, https://doi.org/10.1021/acs.est.2c06311, 2023.

Kroll, J. H., Clarke, J. S., Donahue, N. M., Anderson, J. G., and Demerjian, K. L.: Mechanism of HO_x formation in the gas-phase ozone−alkene reaction. 1. Direct, pressure-dependent measurements of prompt OH yields, J. Phys. Chem. A, 105, 1554-1560, https://doi.org/10.1021/jp002121r, 2001.

Kroopnick, P. and Craig, H.: Atmospheric oxygen: Isotopic composition and solubility fractionation, Science, 175, 54-55, https://doi.org/10.1126/science.175.4017.54, 1972.

Kundu, S., Kawamura, K., and Lee, M.: Seasonal variation of the concentrations of nitrogenous species and their nitrogen isotopic ratios in aerosols at Gosan, Jeju Island: Implications for atmospheric processing and source changes of aerosols, J. Geophys. Res.: Atmos., 115, D20305, https://doi.org/10.1029/2009JD013323, 2010.

Lin, Y.-C., Zhang, Y.-L., Yu, M., Fan, M.-Y., Xie, F., Zhang, W.-Q., Wu, G., Cong, Z., and Michalski, G.: Formation mechanisms and source apportionments of airborne nitrate aerosols at a Himalayan-Tibetan Plateau site: Insights from nitrogen and oxygen isotopic compositions, Environ. Sci. Technol., 55, 12261-12271, https://doi.org/10.1021/acs.est.1c03957, 2021.

Lin, Z., Ji, X., Xu, L., Chen, G., Yang, C., Zhang, K., Zhang, F., Li, L., Chen, Y., and Chen, J.: Enhanced NO_2-driven multiphase formation of particulate nitrate and sulfate under high-humidity conditions, npj Clim. Atmos. Sci., 9, 76, https://doi.org/10.1038/s41612-026-01352-5, 2026.

Meng, W., Zhong, Q., Yun, X., Zhu, X., Huang, T., Shen, H., Chen, Y., Chen, H., Zhou, F., Liu, J., Wang, X., Zeng, E. Y., and Tao, S.: Improvement of a global high-resolution ammonia emission inventory for combustion and industrial sources with new data from the residential and transportation sectors, Environ. Sci. Technol., 51, 2821-2829, https://doi.org/10.1021/acs.est.6b03694, 2017.

Moore, H.: The isotopic composition of ammonia, nitrogen dioxide and nitrate in the atmosphere, Atmos. Environ., 11, 1239-1243, https://doi.org/10.1016/0004-6981(77)90102-0, 1977.

Morin, S., Savarino, J., Frey, M. M., Domine, F., Jacobi, H.-W., Kaleschke, L., and Martins, J. M. F.: Comprehensive isotopic composition of atmospheric nitrate in the Atlantic Ocean boundary layer from 65°S to 79°N, J. Geophys. Res.: Atmos., 114, D05303, https://doi.org/10.1029/2008JD010696, 2009.

Murphy, S. E., Buenconsejo, R. S., Draper, D. C., Crounse, J. D., Baliaka, H. D., Ward, R. X., Schulze, B. C., Rezgui, S. P., Ball, K., Susskind, T., Kappaganthula, G., and Wennberg, P. O.: Multi-functional organic nitrogen in the Los Angeles Air Basin, ACS ES&T Air, 2, 2009-2027, https://doi.org/10.1021/acsestair.5c00206, 2025.

Pan, Y., Tian, S., Liu, D., Fang, Y., Zhu, X., Zhang, Q., Zheng, B., Michalski, G., and Wang, Y.: Fossil fuel combustion-related emissions dominate atmospheric ammonia sources during severe haze episodes: Evidence from ^{15}N-stable isotope in size-resolved aerosol ammonium, Environ. Sci. Technol., 50, 8049-8056, https://doi.org/10.1021/acs.est.6b00634, 2016.

Proemse, B. C., Mayer, B., Chow, J. C., and Watson, J. G.: Isotopic characterization of nitrate, ammonium and sulfate in stack $PM_{2.5}$ emissions in the Athabasca Oil Sands Region, Alberta, Canada, Atmos. Environ., 60, 555-563, https://doi.org/10.1016/j.atmosenv.2012.06.046, 2012.

Pye, H. O. T., Nenes, A., Alexander, B., Ault, A. P., Barth, M. C., Clegg, S. L., Collett Jr, J. L., Fahey, K. M., Hennigan, C. J., Herrmann, H., Kanakidou, M., Kelly, J. T., Ku, I. T., McNeill, V. F., Riemer, N., Schaefer, T., Shi, G., Tilgner, A., Walker, J. T., Wang, T., Weber, R., Xing, J., Zaveri, R. A., and Zuend, A.: The acidity of atmospheric particles and clouds, Atmos. Chem. Phys., 20, 4809-4888, https://doi.org/10.5194/acp-20-4809-2020, 2020.

Romer, P. S., Duffey, K. C., Wooldridge, P. J., Allen, H. M., Ayres, B. R., Brown, S. S., Brune, W. H., Crounse, J. D., de Gouw, J., Draper, D. C., Feiner, P. A., Fry, J. L., Goldstein, A. H., Koss, A., Misztal, P. K., Nguyen, T. B., Olson, K., Teng, A. P., Wennberg, P. O., Wild, R. J., Zhang, L., and Cohen, R. C.: The lifetime of nitrogen oxides in an isoprene-dominated forest, Atmos. Chem. Phys., 16, 7623-7637, https://doi.org/10.5194/acp-16-7623-2016, 2016.

Savard, M. M., Cole, A., Smirnoff, A., and Vet, R.: $\delta^{15}N$ values of atmospheric N species simultaneously collected using sector-based samplers distant from sources – Isotopic inheritance and fractionation, Atmos. Environ., 162, 11-22, https://doi.org/10.1016/j.atmosenv.2017.05.010, 2017.

Stock, B. C. and Semmens, B. X.: MixSIAR GUI User Manual. Version 3.1, https://doi.org/10.5281/zenodo.1209993, 2016.

Stock, B. C., Jackson, A. L., Ward, E. J., Parnell, A. C., Phillips, D. L., and Semmens, B. X.: Analyzing mixing systems using a new generation of Bayesian tracer mixing models, PeerJ, 6, e5096, https://doi.org/10.7717/peerj.5096, 2018.

Ti, C., Gao, B., Luo, Y., Wang, X., Wang, S., and Yan, X.: Isotopic characterization of NH_x-N in deposition and major emission sources, Biogeochemistry, 138, 85-102, https://doi.org/10.1007/s10533-018-0432-3, 2018.

Tsai, I. C., Hsieh, P.-R., Hsu, H.-H., Tung, Y.-S., Chen, Y.-M., and Cheng, C.-T.: Climate change-induced impacts on $PM_{2.5}$ in Taiwan under 2 and 4 °C global warming, Atmos. Pollut. Res., 15, 102106, https://doi.org/10.1016/j.apr.2024.102106, 2024.

Vicars, W. C., Morin, S., Savarino, J., Wagner, N. L., Erbland, J., Vince, E., Martins, J. M. F., Lerner, B. M., Quinn, P. K., Coffman, D. J., Williams, E. J., and Brown, S. S.: Spatial and diurnal variability in reactive nitrogen oxide chemistry as reflected in the isotopic composition of atmospheric nitrate: Results from the CalNex 2010 field study, J. Geophys. Res.: Atmos., 118, 10,567-510,588, https://doi.org/10.1002/jgrd.50680, 2013.

Walters, W. W. and Michalski, G.: Theoretical calculation of oxygen equilibrium isotope fractionation factors involving various NO_y molecules, OH, and H_2O and its implications for isotope variations in atmospheric nitrate, Geochim. Cosmochim. Acta, 191, 89-101, https://doi.org/10.1016/j.gca.2016.06.039, 2016.

Walters, W. W., Karod, M., Willcocks, E., Baek, B. H., Blum, D. E., and Hastings, M. G.: Quantifying the importance of vehicle ammonia emissions in an urban area of northeastern USA utilizing nitrogen isotopes, Atmos. Chem. Phys., 22, 13431-13448, https://doi.org/10.5194/acp-22-13431-2022, 2022.

Walters, W. W., Song, L., Chai, J., Fang, Y., Colombi, N., and Hastings, M. G.: Characterizing the spatiotemporal nitrogen stable isotopic composition of ammonia in vehicle plumes, Atmos. Chem. Phys., 20, 11551-11567, https://doi.org/10.5194/acp-20-11551-2020, 2020.

Ward, R. X., Baliaka, H. D., Schulze, B. C., Kerr, G. H., Crounse, J. D., Hasheminassab, S., Bahreini, R., Dillner, A. M., Russell, A., Ng, N. L., Wennberg, P. O., Flagan, R. C., and Seinfeld, J. H.: Poorly quantified trends in ammonium nitrate remain critical to understand future urban aerosol control strategies, Science Advances, 11, eadt8957, https://doi.org/10.1126/sciadv.adt8957, 2025.

Weigand, M. A., Foriel, J., Barnett, B., Oleynik, S., and Sigman, D. M.: Updates to instrumentation and protocols for isotopic analysis of nitrate by the denitrifier method, Rapid Commun. Mass Spectrom., 30, 1365-1383, https://doi.org/10.1002/rcm.7570, 2016.

Wu, C., Cao, C., Li, J., Lv, S., Li, J., Liu, X., Zhang, S., Liu, S., Zhang, F., Meng, J., and Wang, G.: Different physicochemical behaviors of nitrate and ammonium during transport: a case study on Mt. Hua, China, Atmos. Chem. Phys., 22, 15621-15635, https://doi.org/10.5194/acp-22-15621-2022, 2022.

Xu, W., Kuang, Y., Xu, W., Liu, L., Xu, H., Wang, X., Liu, Y., Cheng, H., Zhang, X., Zhai, M., Liu, C., Liang, L., Zhang, G., Luo, B., Tao, J., Liu, J., Zhao, H., Ren, S., Zhou, G., Liu, P., Xu, X., and Sun, Y.: Efficient nitrate formation in fog events implicates fog interstitial aerosols as significant drivers of atmospheric chemistry, Environ. Sci. Technol., 58, 22298-22311, https://doi.org/10.1021/acs.est.4c09078, 2024.

Yu, H.-R., Zhang, Y.-L., Cao, F., Zhao, Z.-Y., Fan, M.-Y., and Yang, X.-Y.: Fog event is possibly a source rather than a sink of atmospheric nitrate aerosols: Insights from isotopic measurements in Nanjing, China, Appl. Geochem., 155, 105721, https://doi.org/10.1016/j.apgeochem.2023.105721, 2023.

Yu, X., Li, Q., Liao, K., Li, Y., Wang, X., Zhou, Y., Liang, Y., and Yu, J. Z.: New measurements reveal a large contribution of nitrogenous molecules to ambient organic aerosol, npj Clim. Atmos. Sci., 7, 72, https://doi.org/10.1038/s41612-024-00620-6, 2024.

Zhang, G., Hu, X., Sun, W., Yang, Y., Guo, Z., Fu, Y., Wang, H., Zhou, S., Li, L., Tang, M., Shi, Z., Chen, D., Bi, X., and Wang, X.: A comprehensive study about the in-cloud processing of nitrate through coupled measurements of individual cloud residuals and cloud water, Atmos. Chem. Phys., 22, 9571-9582, https://doi.org/10.5194/acp-22-9571-2022, 2022.

Zhang, Q., Jiang, X., Tong, D., Davis, S. J., Zhao, H., Geng, G., Feng, T., Zheng, B., Lu, Z., Streets, D. G., Ni, R., Brauer, M., van Donkelaar, A., Martin, R. V., Huo, H., Liu, Z., Pan, D., Kan, H., Yan, Y., Lin, J., He, K., and Guan, D.: Transboundary health impacts of transported global air pollution and international trade, Nature, 543, 705-709, https://doi.org/10.1038/nature21712, 2017.

Zhou, W., Xu, W., Kim, H., Zhang, Q., Fu, P., Worsnop, D. R., and Sun, Y.: A review of aerosol chemistry in Asia: Insights from aerosol mass spectrometer measurements, Environ. Sci. Processes Impacts, 22, 1616-1653, https://doi.org/10.1039/D0EM00212G, 2020.

Supporting Information

Description S1. Particle concentration estimated by FTIR analysis

Description S2. Calculation of mass-weighted particle diameter (D_m)

Description S3~~3~~. Sensitivity analyses on $\varepsilon_{NH_4^+-NH_3}$

Description S4~~4~~. Sensitivity analyses on the nitrate formation pathway

Description S5. Calculation of concentration-weighted $\delta^{15}N\text{-}NH_4^+$, $\delta^{15}N\text{-}NO_3^-$, and $\delta^{18}O\text{-}NO_3^-$

Table S1. Sensitivity of gas–particle equilibrium in estimating NH_3 emission sources.

Table S2~~1~~. Ranges of $\delta^{15}N\text{-}NH_3$ values (mean ± SD‰) from fertilizer, waste, NH_3 slip, and fossil fuel (Kawashima et al., 2023).

Table S3~~2~~. Reconstructed $\delta^{18}O$ (‰) from MixSIAR results of C0, C1, and C2 scenarios.

Table S4~~3~~. Fractional contribution of each nitrate formation pathway in C0 (and C1).

Figure S1. (a) Horizontal distance between the sampling location (Xitou) and Taichung, plotted using GeoMapApp (ver 3.7.4). (b) Elevation profile along the same transect between the sampling location (Xitou) and Taichung.

Figure S2. pNH_4^+ concentration measured by fluorometric versus those estimated by CMAQ analysis.

Figure S3. Estimated $\delta^{18}O$ during HNO_3 formation adapted from Chen et al. (2022). Yellow boxes indicate OH directly derived from the oxygen atom in H_2O.

Figure S4. Size-resolved aerosol (a) NH_4^+, (b) NO_3^-, (c) SO_4^{2-}, and (d) BC concentrations.

Figure S5~~5~~. Particulate $\delta^{15}N\text{-}NH_4^+$ measured in this study (red symbol) and reported in the literature.

Figure S6. Scatter plot of $[NO_3^-] + 2*[SO_4^{2-}]$ versus $[NH_4^+]$ measured by ion chromatography during the observation period.

Figure S7. NOAA HYSPLIT 24-h backward trajectories for air parcels arriving at the receptor site (23°40'12" N, 120°47'54" E) at 10 m above ground level, calculated using the Global Forecasting System (GFS) meteorological data at a 0.25° spatial resolution. Trajectories are shown for arrival times of 0400 UTC (1200 LT) and 1700 UTC (0100 LT). Analyses were performed using the NOAA Air Resources Laboratory HYSPLIT model (https://www.ready.noaa.gov/HYSPLIT.php). The trajectory arriving at 1200 LT on 20 and 21 April (pink and light blue) transited through agriculturally dominated lowland areas (Yunlin and Chiayi counties) prior to reaching the receptor site.

~~Figure S4. Size-resolved aerosol (a) NH_4^+, (b) NO_3^-, (c) SO_4^{2-}, and (d) BC concentrations.~~

~~Figure S5. Particulate $\delta^{15}N\text{-}NH_4^+$ measured in this study (red symbol) and reported in the literature.~~

~~Figure S6 Scatter plot of $[NO_3^-] + 2*[SO_4^{2-}]$ versus $[NH_4^+]$ measured during the observation period.~~

Figure S8~~7~~. Temporal variation of (a) NH_3 concentration (from CMAQ), (b) pNH_4^+ concentration (from fluorometric analysis), and (c) the estimated f (= $[pNH_4^+]$ / ($[NH_3]$ +$[pNH_4^+]$)).~~Resulting concentration of (a) NH_3, (b) pNH_4^+, and (c) the estimated f from fluorometric and CMAQ analysis.~~

Figure S9~~8~~. Source apportionment results for NH_3 from the MixSIAR framework for (a) fossil fuel, (b) NH_3 slip, (c) waste, and (d) fertilizer~~Source apportionment results from the MixSIAR framework for (a) fossil fuel, (b) NH_3 slip, (c) waste, and (d) fertilizer~~.

Figure S10~~9~~. Particulate $\delta^{15}N\text{-}NO_3^-$ measured in this study (red symbol) and reported in the literature.

Figure S11~~10~~. Particulate $\delta^{18}O\text{-}NO_3^-$ measured in this study (red symbol) and reported in the literature.

Figure S12~~11~~. Daily size-resolved isotopic composition of $p\mathrm{NO_3^-}$ from 17 to 20 April.

Figure S13~~12~~. Daily size-resolved isotopic composition of $p\mathrm{NO_3^-}$ from 21 to 24 April.

Figure S14~~13~~. Relationship between particulate $\delta^{15}\mathrm{N\text{-}NO_3^-}$ versus $\delta^{18}\mathrm{O\text{-}NO_3^-}$ in this study (red symbols) and reported in the literature~~Particulate $\delta^{15}\mathrm{N\text{-}NO_3^-}$ versus $\delta^{18}\mathrm{O\text{-}NO_3^-}$ measured in this study (red symbols) and reported in the literature~~. Red open circles represent individual measurements from this study, while the red solid circle denotes the mean value.

~~Figure S14. Contributions of nitrate formation pathways estimated by MixSIAR. (a, c) Measured $\delta^{18}\mathrm{O\text{-}NO_3^-}$ values with the corresponding $\delta^{18}\mathrm{O}$ ranges of potential formation pathways. (b, d) estimated fractional contributions of these pathways (*c.f.*, Fig. S3).~~

Figure S15~~15~~. Correlation between daily-averaged CO concentration and $\delta^{18}\mathrm{O\text{-}NO_3^-}$.

Supplementary Information for

Size-resolved isotope analysis reveals anthropogenic reactive nitrogen transport and transformation in Taiwan mountain forests

Wen-Chien Lee,[1] Ming-Hao Huang,[1] Wei-Chieh Huang,[1] Jen-Ping Chen,[1] Yen-Jen Lai,[2,3] Haojia Ren,[4]* and Hui-Ming Hung[1]*

[1] Department of Atmospheric Sciences, National Taiwan University, Taipei, 10617, Taiwan

[2] Experimental Forest, National Taiwan University, Nantou, 557004, Taiwan

[3] Department of Agricultural Chemistry, National Taiwan University, Taipei, 10617, Taiwan

[4] Department of Geosciences, National Taiwan University, Taipei, 10617, Taiwan

Correspondence to: Haojia Ren (abbyren@ntu.edu.tw) and Hui-Ming Hung (hmhung@ntu.edu.tw)

This PDF file includes:

Number of pages: 22~~1~~

Number of Descriptions: ~~3~~5

Number of tables: ~~1~~4

Number of figures: 15~~5~~

Description S1. Particle concentration estimated by FTIR analysis

The mass concentration of aerosol particles on the filter samples was estimated using FTIR absorbance spectra, as detailed in Chen et al. (2022). First, specific peaks in the absorbance spectra were identified and quantified, including the NH_4^+ peak at 1417 cm^{-1} in the region of 1405−1450 cm^{-1}, the NO_3^- peak at 1340−1355 cm^{-1}, the SO_4^{2-} peak at 1085 cm^{-1}, and the BC peak at 3945−3955 cm^{-1}. The peaks were fitted with Lorentzian functions to derive the absorbance (*Abs*) of each functional group. FTIR absorbance and mass concentration measured by ion chromatography (IC) were then applied to derive the mass concentrations of the functional groups by assuming a well-distributed sample on the filter:

$$\frac{A_{\mathrm{FTIR}}}{A_{\mathrm{sample}}} \times m \times F \times t_s = \alpha \times Abs \tag{S1}$$

where A_{FTIR} is the FTIR scanning area, A_{sample} is the sampling area on the filter, m is the mass concentration measured by IC, F is the sampling flow rate, t_s is the sampling time, and α is obtained through an experimental regression of IC and FTIR measurements.

Description S2. Calculation of mass-weighted particle diameter (D_{m})

Aerosol particle diameter was determined from filter samples collected using a micro-orifice uniform deposit impactor (MOUDI). To ensure sufficient particle concentrations for isotope analysis, some filter samples were combined. For these combined samples, the particle diameters were calculated as mass-weighted diameters for specific chemical species according to:

$$\log D_{\mathrm{m}} = \frac{\sum_{i=1}^{n}\left(\log D_i \times m_{D_i}\right)}{\sum_{i=1}^{n} m_{D_i}} \tag{S2}$$

where D_{m} is the mass-weighted diameter, D_i is the geometric mean diameter of particles collected in the i^{th} stage of the MOUDI sampler, m_{D_i} is the mass concentration of particles with a diameter D_i determined by FTIR analysis, and n is the number of combined filter samples. Mass-weighted particle diameters were calculated separately for $p\mathrm{NH_4^+}$ and $p\mathrm{NO_3^-}$.

Description S3 Sensitivity analyses on $\varepsilon_{\mathrm{NH_4^+-NH_3}}$

The influence of (1) temperature, (2) gas–particle equilibrium, and (3) open-system equilibrium assumptions on $\varepsilon_{NH_4^+-NH_3}$ is discussed below.

Temperature dependence. The temperature sensitivity of $\varepsilon_{NH_4^+-NH_3}$ was estimated using the empirical relationship of Kawashima et al. (2023):

$$\varepsilon_{NH_4^+-NH_3} = \frac{12.4678\times1000}{(T+273.15)} - 7.6694, \quad \text{(S3)}$$

where T represents temperature in °C. Over the observed temperature range at Xitou (10–30°C), $\varepsilon_{NH_4^+-NH_3}$ varied from 36.36‰ (at 10°C) to 33.46‰ (at 30°C). MixSIAR source contributions estimated at these two temperature extremes are summarized in Table S1 (~~+~~ $\varepsilon_{NH_4^+-NH_3}$ of 33‰ and 37‰). Contributions from fertilizer and waste were insensitive to temperature. The most notable temperature effect was on fossil fuel and NH_3 slip: the fossil fuel contribution decreased by ~ 20% at higher temperature, while NH_3 slip increased correspondingly by ~ 20%.

Gas–particle equilibrium fractionation pathways. In addition to the baseline fractionation reaction ($NH_4^+{}_{(aq/s)}/NH_{3(g)}$ equilibrium during condensation (equilibrium isotope effect (EIE) of 33‰)), three alternative fractionation scenarios were tested: (1) nucleation with a kinetic isotope effect (KIE) of −28‰, (2) $NH_{3(aq)}/NH_{3(g)}$ equilibrium during condensation (EIE of 4 ± 3‰), and (3) $NH_4^+{}_{(aq)}/NH_{3(aq)}$ equilibrium during condensation (EIE = 37 ± 4‰) (Chang et al., 2025). Because δ^{15}N-NH_3 was not directly measured in this study, δ^{15}N-NH_3 was inferred from fractionation factors rather than observation. Each scenario was therefore evaluated independently under the assumption that it contributed 100% to NH_3 formation, and the resulting MixSIAR source contributions are reported in Table S1~~+~~.

Under equilibrium fractionation scenarios (EIE = 4, 33, 37‰), contributions from fertilizer and waste ranged from 1.8–4.6% and 2.8–7.1%, respectively, while fossil fuel and NH_3 slip ranged from 21.1–66.4% and 23.2–74.3%, respectively. The combined contribution of fossil fuel and NH_3 slip remained dominant across all EIE scenarios (88–95%), indicating that the qualitative conclusion that "anthropogenic NH_3 sources dominate particulate ammonium at Xitou" is robust to the choice of equilibrium fractionation factor.

Open-system equilibrium assumptions. Under the KIE scenario, the estimated fertilizer contribution increased to 26.6%, and fossil fuel decreased to 12.6%, while NH_3 slip and waste remained within the range spanned by EIE scenarios. However, the KIE scenario represents a physically extreme end-member.

At Xitou, NH_3 formation is dominated by condensation under open-system conditions, where $NH_{3(g)}$ undergoes continuous exchange with the gas phase rather than irreversible incorporation. Under such conditions, isotope fractionation is expected to approach thermodynamic equilibrium (EIE) rather than kinetic control (KIE). The KIE result is therefore best interpreted as an upper bound on source apportionment uncertainty rather than a physically realistic atmospheric scenario.

Description S4. Sensitivity analyses on the nitrate formation pathway

Sensitivity analyses were performed to compare three different model configurations (C0–C2):

- C0 (main text): $P_{RO_2\text{-}OH1}$, $P_{RO_2\text{-}het}$, and $P_{O_3\text{-}het}$
- C1 (full): $P_{RO_2\text{-}OH1}$, $P_{RO_2\text{-}OH2}$, $P_{RO_2\text{-}het}$, $P_{O_3\text{-}OH1}$, $P_{O_3\text{-}OH2}$, $P_{O_3\text{-}het}$
- C2 (nighttime only): $P_{RO_2\text{-}het}$ and $P_{O_3\text{-}het}$

The results demonstrate that C0 provides the best fit. In addition, excluding P1a (C2) leads to a sharp increase in the absolute differentiation (averaged error) from 4.34‰ to 14‰, as these models fail to capture observed low $\delta^{18}O$ values (< 40‰) (Table S3~~3~~). Furthermore, the full model (C1) did not improve accuracy (averaged error of 5.65‰) and introduced unnecessary complexity due to the identical ^{18}O signatures of $P_{RO_2\text{-}OH2}/P_{RO_2\text{-}het}$ and $P_{O_3\text{-}OH2}/P_{O_3\text{-}het}$ (Figure S4~~4~~). Consequently, C0 was selected as the optimized setting.

Description S5. Calculation of concentration-weighted $\delta^{15}N\text{-}NH_4^+$, $\delta^{15}N\text{-}NO_3^-$, and $\delta^{18}O\text{-}NO_3^-$

The concentration-weighted means of $\delta^{15}N\text{-}NH_4^+$, $\delta^{15}N\text{-}NO_3^-$, and $\delta^{18}O\text{-}NO_3^-$ were calculated for each sampling period to characterize the isotopic composition. The concentration-weighted mean of a given isotope was determined using the following equation:

$$\delta_{\text{avg}}^{\text{isotope}} = \frac{\sum_{j=1}^{m}\left([X]_j \times \delta_j^{\text{isotope}}\right)}{\sum_{j=1}^{m}[X]_j} \quad \text{(S4)}$$

where $\delta_{\text{avg}}^{\text{isotope}}$ is the average isotope value, $[X]_j$ is the mass concentration of compound X in the j^{th} sample, $\delta_j^{\text{isotope}}$ is the isotope value of the j^{th} sample, and ~~p~~ m is the total number of samples in the same sampling period. The mass concentrations of pNH_4^+ and pNO_3^- were measured using a fluorometric and a $NO/NO_2/NO_x$ analyzer (Model T200P, Teledyne API), respectively.

Table S1. Sensitivity of gas–particle equilibrium in estimating NH_3 emission sources.

$\varepsilon_{NH_4^+-NH_3}$	Contribution (%)			
	Fertilizer	Fossil Fuel	NH_3 slip	waste
−28 ‰	26.6 ± 34	12.6 ± 10.4	56.3 ± 35.4	4.6 ± 4.4
4 ‰	1.8 ± 1.9	21.1 ± 15.3	74.3 ± 15.4	2.8 ± 2.9
33 ‰	4.2 ± 3.2	66.4 ± 15.1	23.2 ± 18.3	5.2 ± 5
37 ‰	4.6 ± 3.8	42.3 ± 18.7	46 ± 23	7.1 ± 6.1

Table S2. Ranges of $\delta^{15}N$-NH_3 values (mean±SD‰) from fertilizer, waste, NH_3 slip, and fossil fuel (Kawashima et al., 2023).

Source types	$\delta^{15}N$-NH_3	Statistic number
Fertilizer	−28.3±5.8	21
Waste	−17.6±5.6	51
NH_3 slip	−8.2±5.5	9
Fossil fuel	1.8±3.2	38

Table S3. Reconstructed $\delta^{18}O$ (‰) from MixSIAR results of C0, C1, and C2 scenarios.

Sample ID	Measured $\delta^{18}O$ (‰)	Reconstructed $\delta^{18}O$ (‰) (absolute difference, ‰)		
		C0 (4.34)	C1 (5.65)	C2 (14)
17N	35.86	43.18 (7.32)	44.99 (9.13)	60.05 (24.19)
18N	33.81	42.71 (8.90)	44.54 (10.72)	59.99 (26.18)
19N	73.27	72.48 (0.79)	71.91 (1.36)	74.13 (0.86)
20N	31.94	42.42 (10.47)	44.03 (12.09)	59.97 (28.02)
21N	69.49	69.29 (0.20)	69.02 (0.47)	70.14 (0.65)
22N	43.37	46.01 (2.65)	48.26 (4.89)	60.30 (16.93)
23N	64.79	64.85 (0.06)	65.65 (0.86)	65.56 (1.17)

Table S4. Fractional contribution of each nitrate formation pathway in C0 (and C1).

Sample ID	Measured $\delta^{18}O$ (‰)	Fractional contribution of C0 (and C1)					
		$P_{RO_2\text{-}OH1}$	$P_{RO_2\text{-}OH2}$	$P_{RO_2\text{-}het}$	$P_{O_3\text{-}OH1}$	$P_{O_3\text{-}OH2}$	$P_{O_3\text{-}het}$
17N	35.86	0.91(0.85)	(0.03)	0.06(0.04)	(0.04)	(0.02)	0.03(0.02)
18N	33.81	0.93(0.87)	(0.03)	0.05(0.03)	(0.03)	(0.02)	0.03(0.02)
19N	73.27	0.16(0.09)	(0.17)	0.27(0.14)	(0.14)	(0.23)	0.58(0.23)
20N	31.94	0.94(0.88)	(0.03)	0.04(0.03)	(0.03)	(0.02)	0.02(0.02)
21N	69.49	0.19(0.12)	(0.18)	0.33(0.16)	(0.16)	(0.19)	0.48(0.19)
22N	43.37	0.80(0.73)	(0.06)	0.14(0.07)	(0.07)	(0.03)	0.06(0.03)
23N	64.79	0.24(0.16)	(0.18)	0.41(0.19)	(0.20)	(0.13)	0.36(0.14)

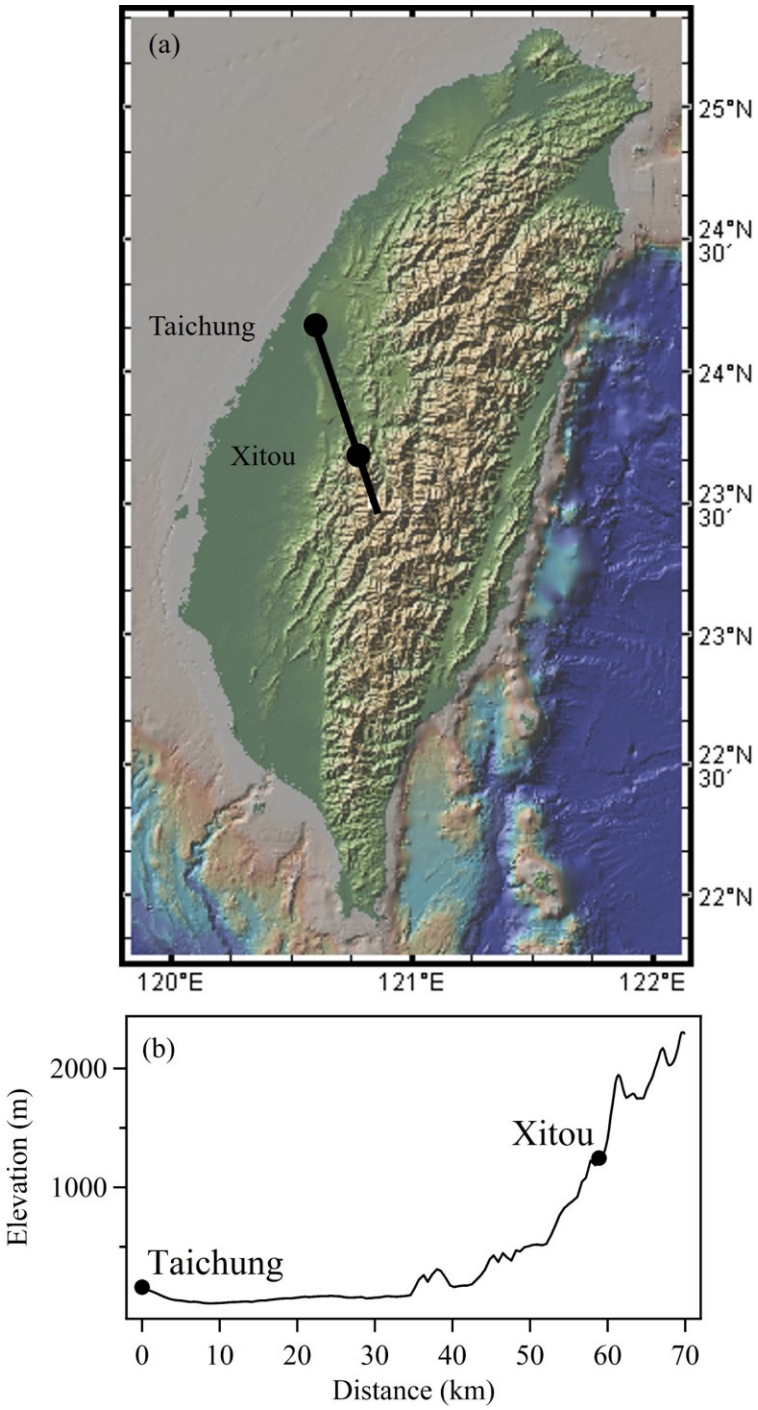

Figure S1. (a) Horizontal distance between the sampling location (Xitou) and Taichung, plotted using GeoMapApp (ver 3.7.4). (b) Elevation profile along the same transect between the sampling location (Xitou) and Taichung.

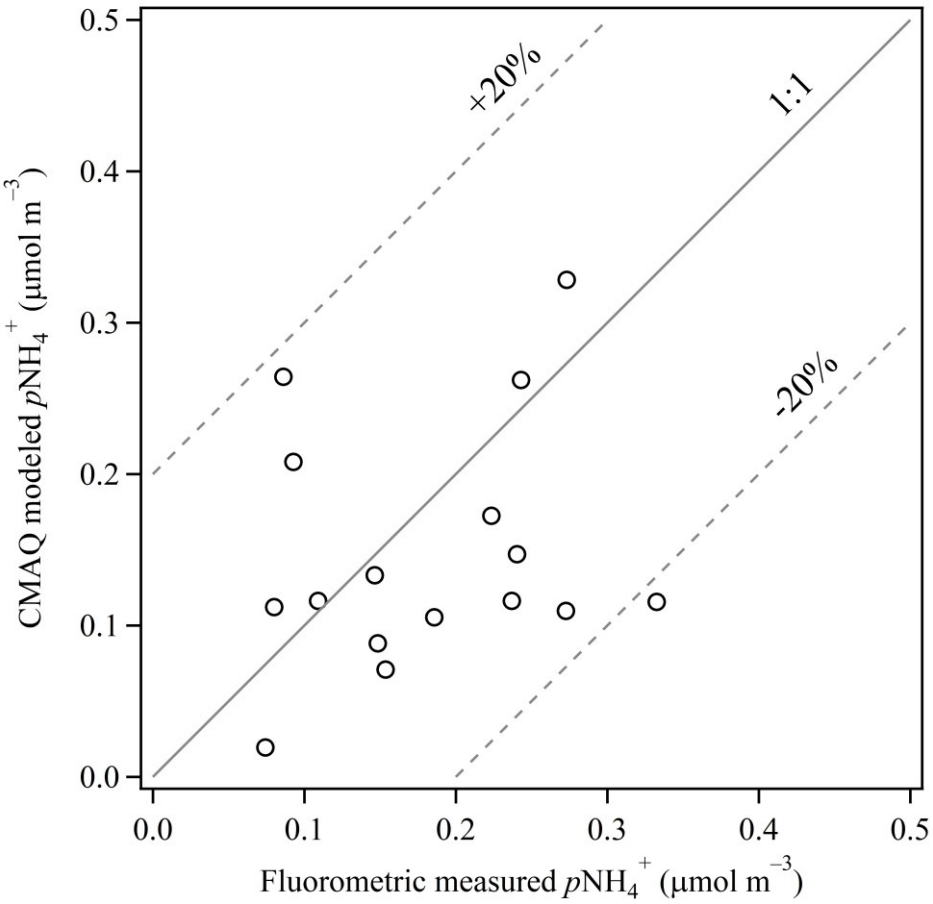

Figure S2. pNH_4^+ concentration measured by fluorometric versus those estimated by CMAQ analysis.

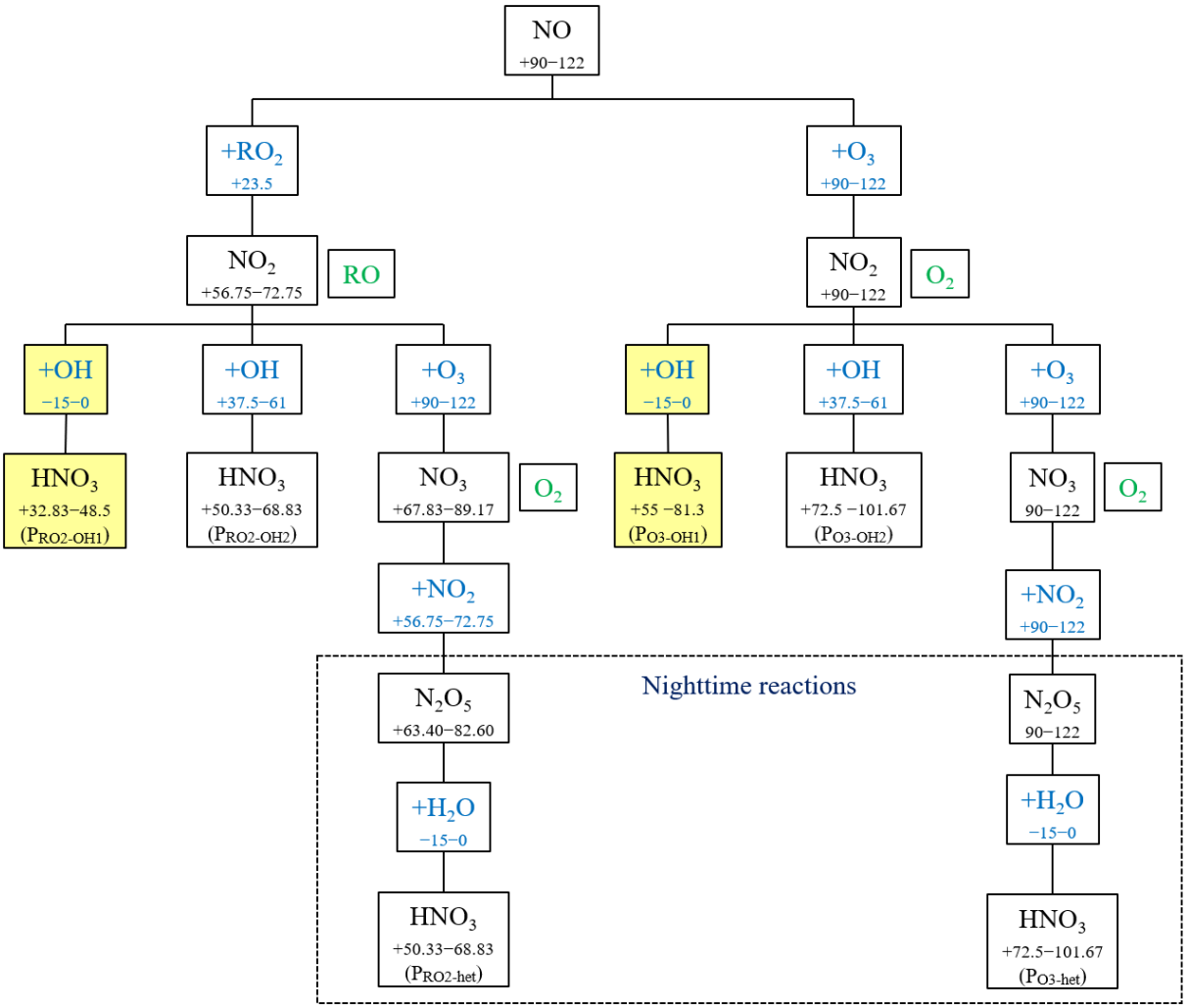
NO
+90−122
+RO2
+23.5
+O3
+90−122
NO2
+56.75−72.75
RO
NO2
+90−122
O2
+OH
−15−0
+OH
+37.5−61
+O3
+90−122
+OH
−15−0
+OH
+37.5−61
+O3
+90−122
HNO3
+32.83−48.5
(PRO2-OH1)
HNO3
+50.33−68.83
(PRO2-OH2)
NO3
+67.83−89.17
O2
HNO3
+55 −81.3
(PO3-OH1)
HNO3
+72.5 −101.67
(PO3-OH2)
NO3
90−122
O2
+NO2
+56.75−72.75
+NO2
+90−122
Nighttime reactions
N2O5
+63.40−82.60
N2O5
90−122
+H2O
−15−0
+H2O
−15−0
HNO3
+50.33−68.83
(PRO2-het)
HNO3
+72.5−101.67
(PO3-het)

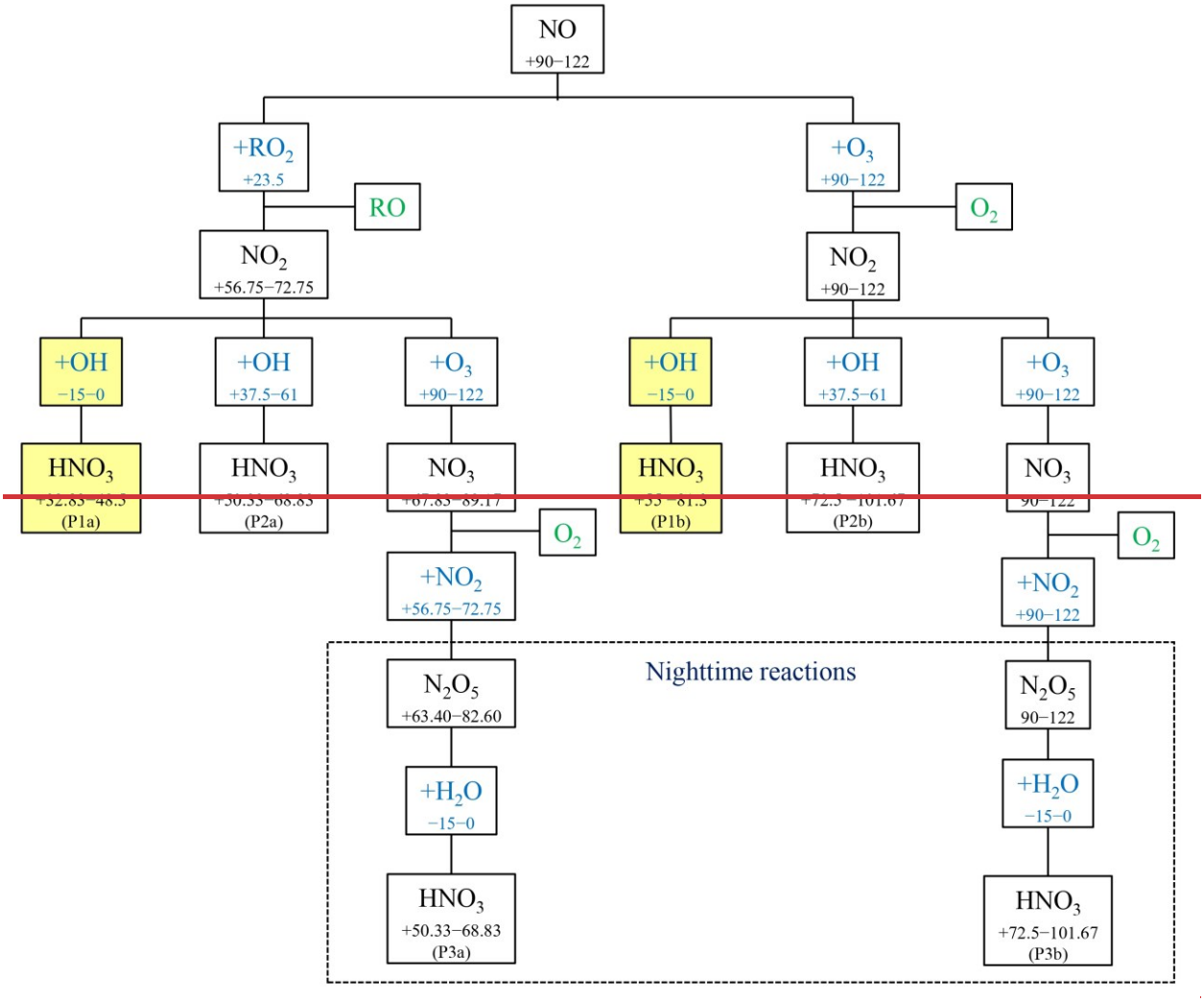

Figure S3. Estimated $\delta^{18}O$ (‰) during HNO_3 formation adapted from Chen et al. (2022). Yellow boxes indicate OH directly derived from the oxygen atom in H_2O.

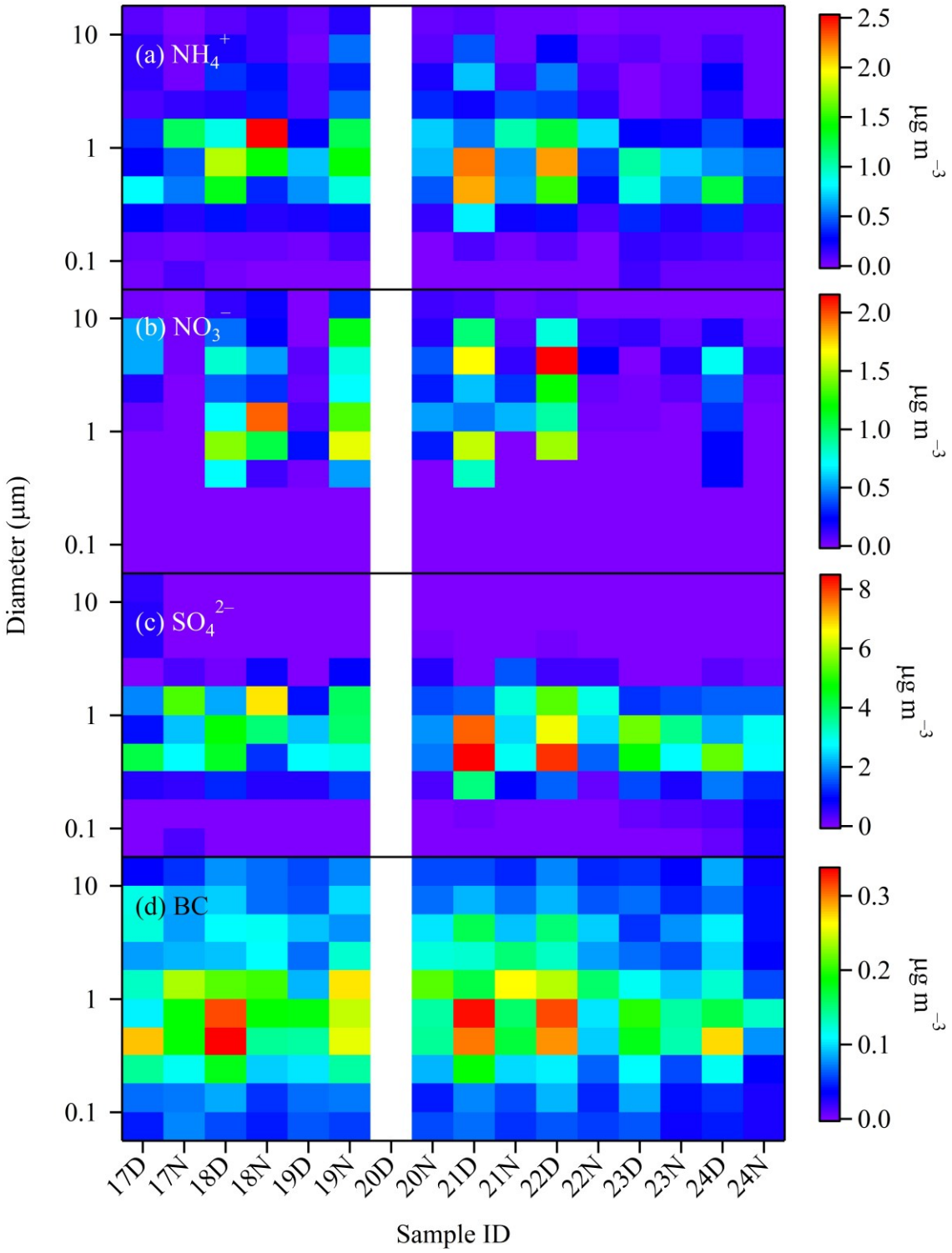

Figure S4. Size-resolved aerosol (a) NH_4^+, (b) NO_3^-, (c) SO_4^{2-}, and (d) BC concentrations.

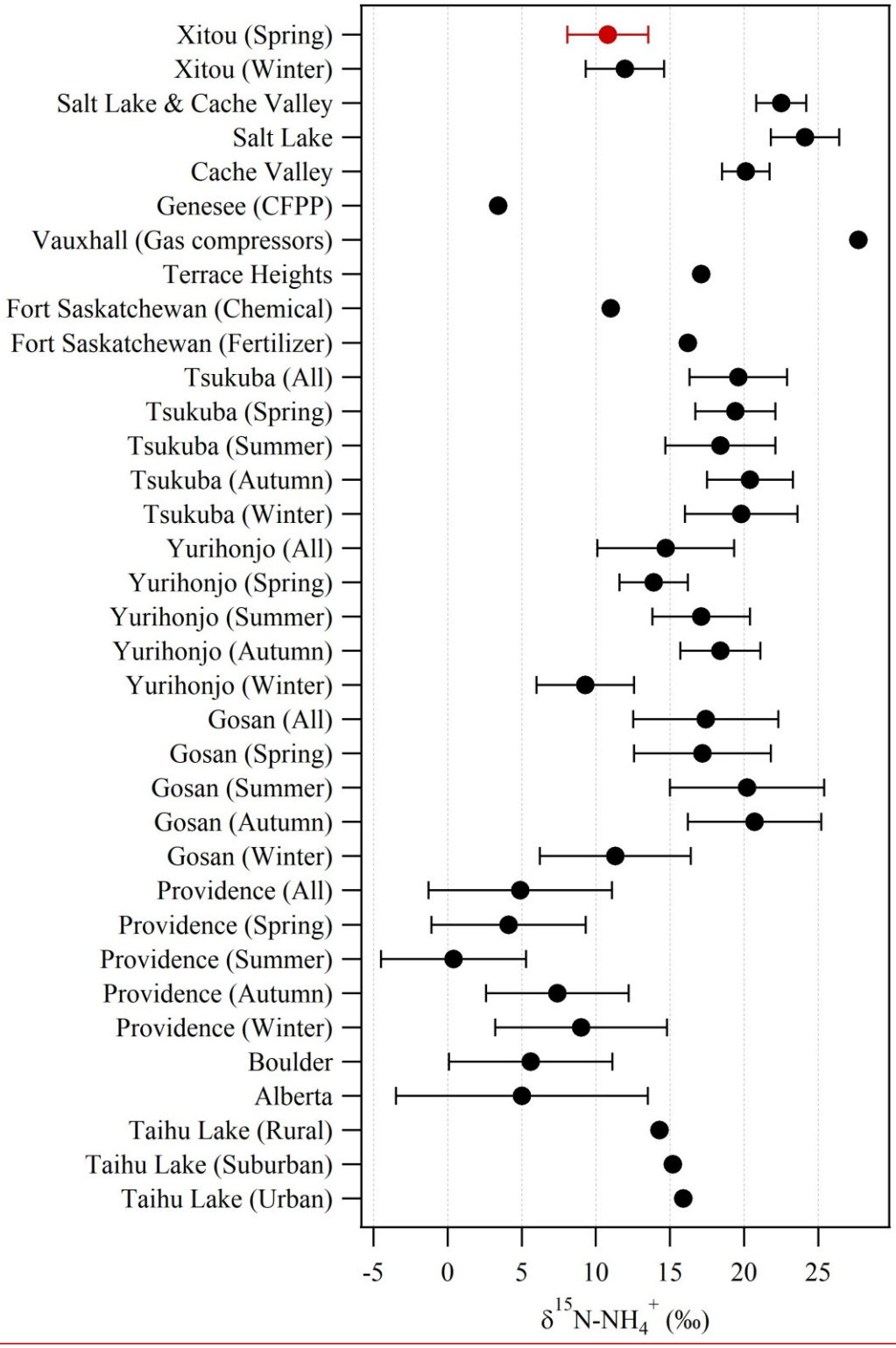

Figure S5. Particulate $\delta^{15}N\text{-}NH_4^+$ measured in this study (red symbol) and reported in the literature (Chen et al., 2022; Savard et al., 2018; Proemse et al., 2012; Hall et al., 2016; Moore, 1977; Kundu et al., 2010; Walters et al., 2022; Kawashima et al., 2023; Ti et al., 2018).

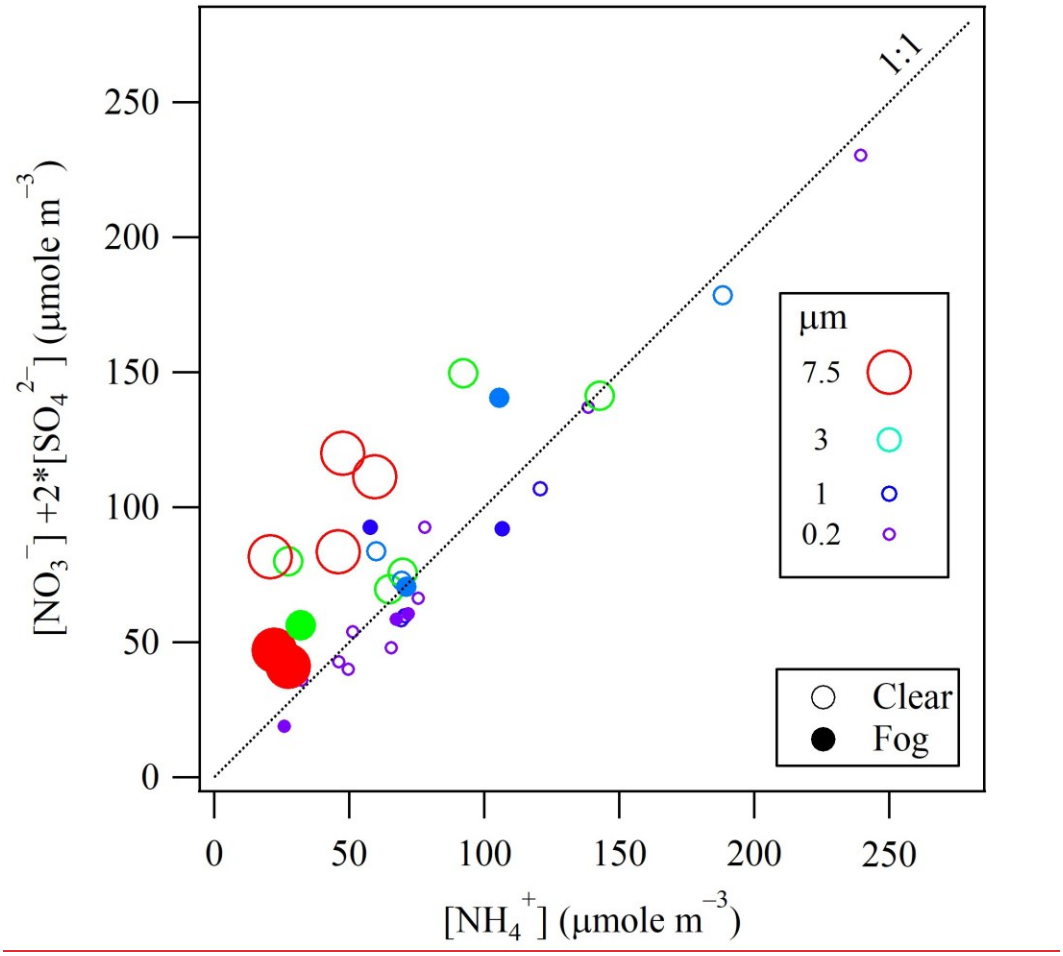
1:1
250
200
150
100
50
0
0
50
100
150
200
250
[NO3−] +2*[SO4 2−] (µmole m−3)
[NH4+] (µmole m−3)
µm
7.5
3
1
0.2
Clear
Fog

Figure S6. Scatter plot of $[NO_3^-] + 2*[SO_4^{2-}]$ versus $[NH_4^+]$ measured by ion chromatography during the observation period.

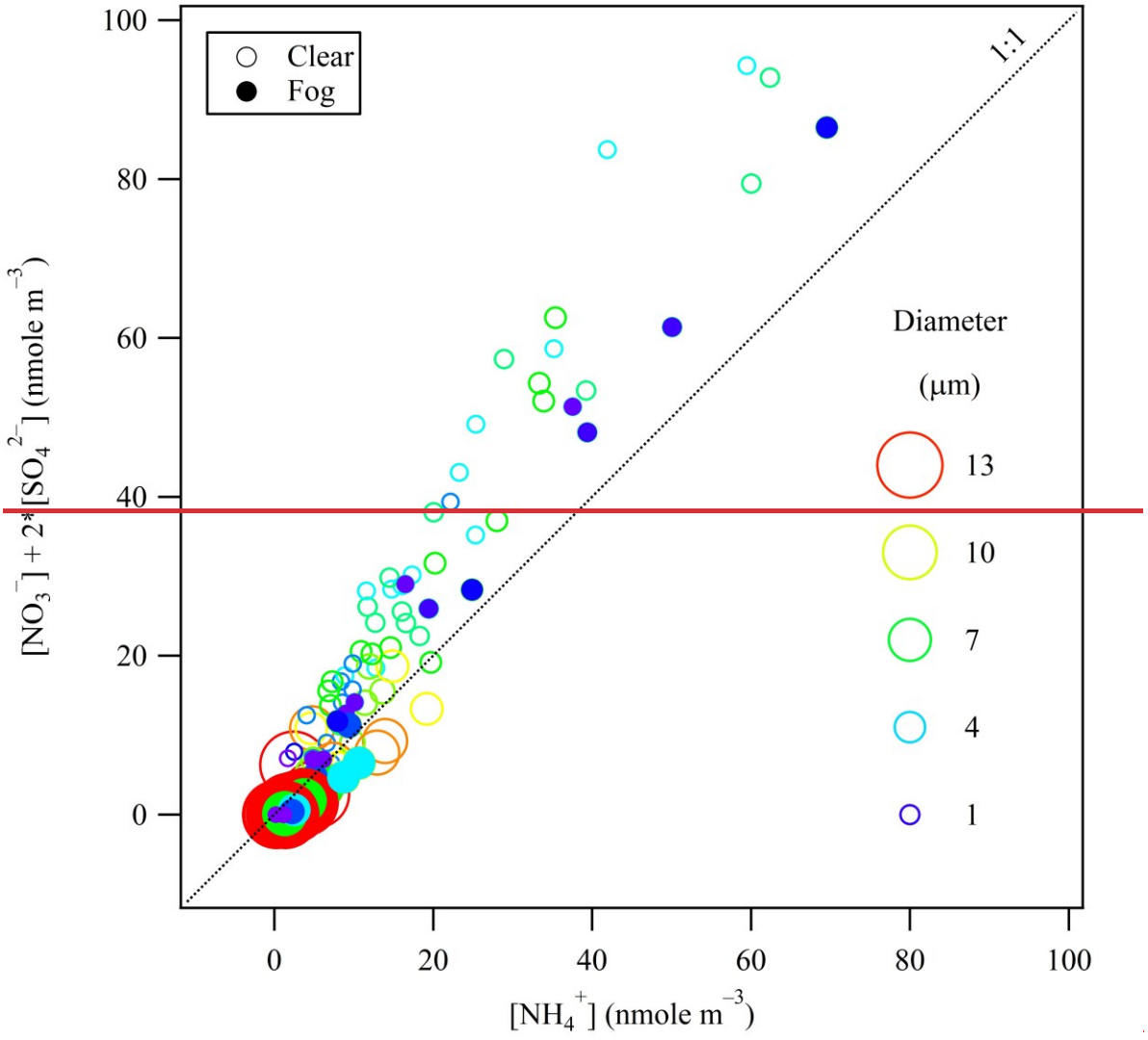

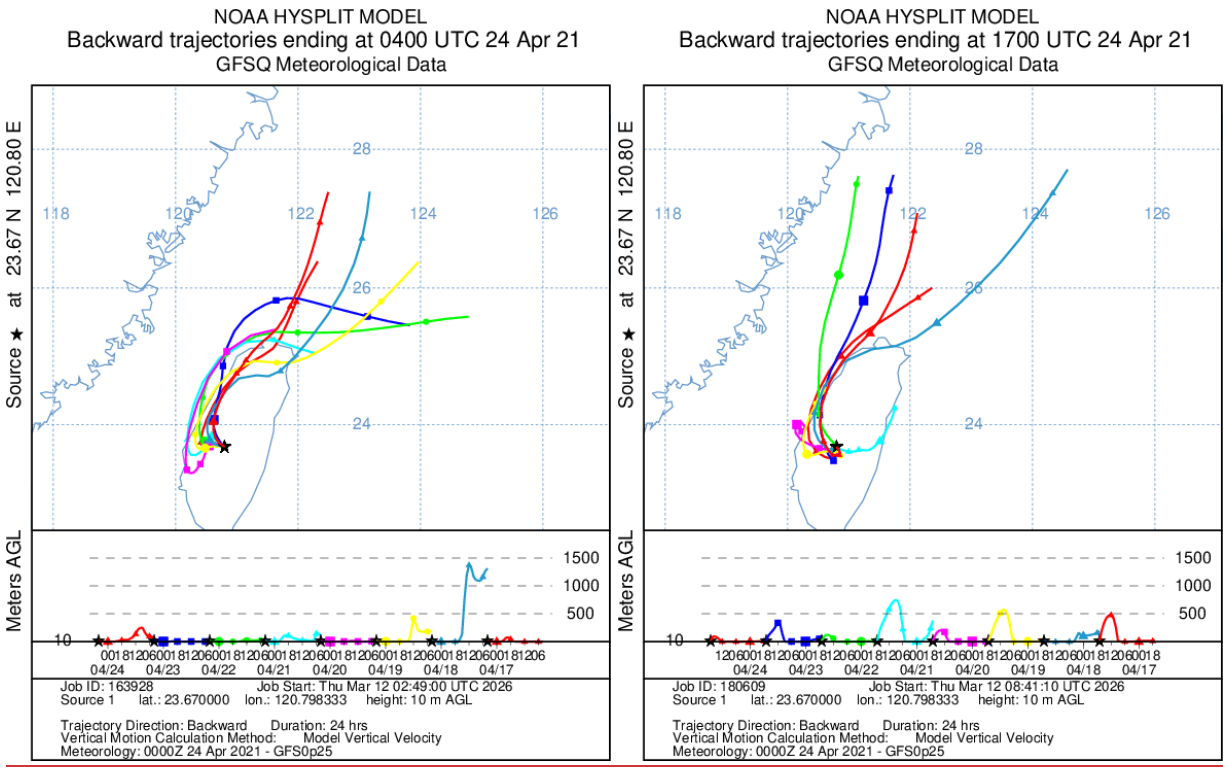

Figure S7. NOAA HYSPLIT 24-h backward trajectories for air parcels arriving at the receptor site (23°40'12" N, 120°47'54" E) at 10 m above ground level, calculated using the Global Forecasting System (GFS) meteorological data at a 0.25° spatial resolution. Trajectories are shown for arrival times of 0400 UTC (1200 LT) and 1700 UTC (0100 LT). Analyses were performed using the NOAA Air Resources Laboratory HYSPLIT model (https://www.ready.noaa.gov/HYSPLIT.php). The trajectory arriving at 1200 LT on 20 and 21 April (pink and light blue) transited through agriculturally dominated lowland areas (Yunlin and Chiayi counties) prior to reaching the receptor site.

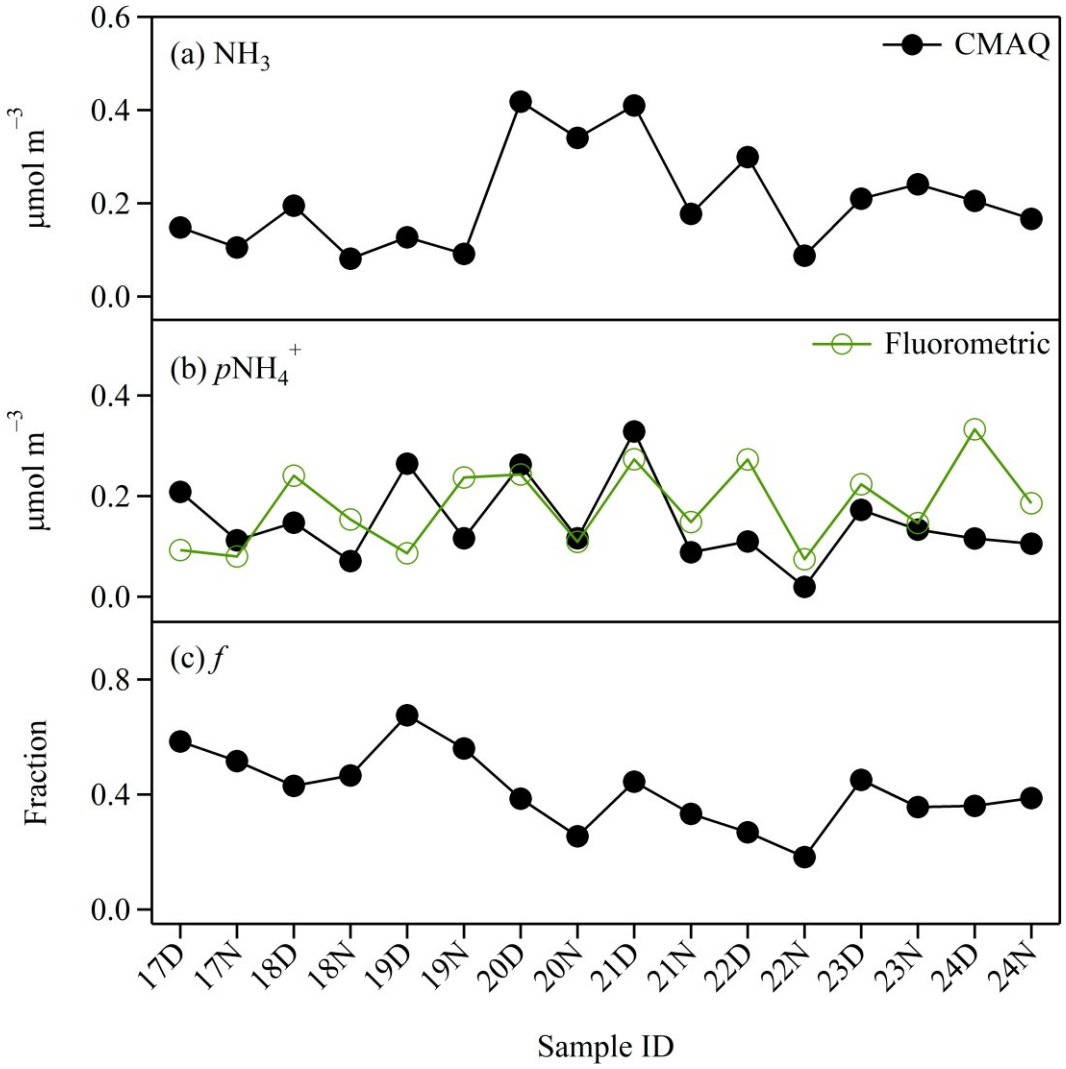

Figure S8. ~~Resulting concentration~~ Temporal variation of (a) NH_3 concentration (from CMAQ), (b) pNH_4^+ concentration (from fluorometric analysis), and (c) the estimated f (= $[pNH_4^+]$ / ($[NH_3]$ + $[pNH_4^+]$))~~from fluorometric and CMAQ analysis~~.

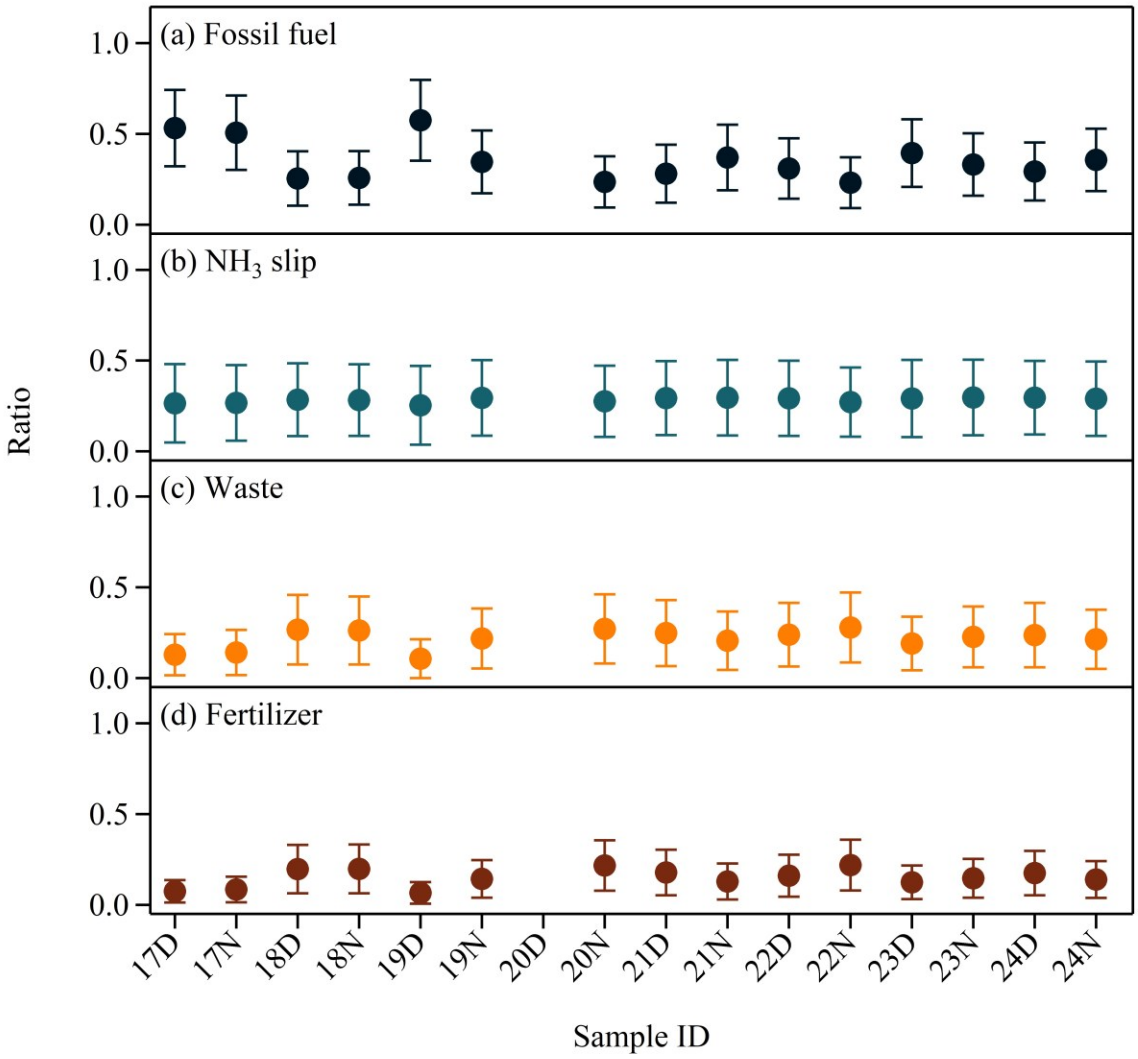

Figure S9. Source apportionment results for NH_3 from the MixSIAR framework for (a) fossil fuel, (b) NH_3 slip, (c) waste, and (d) fertilizer.

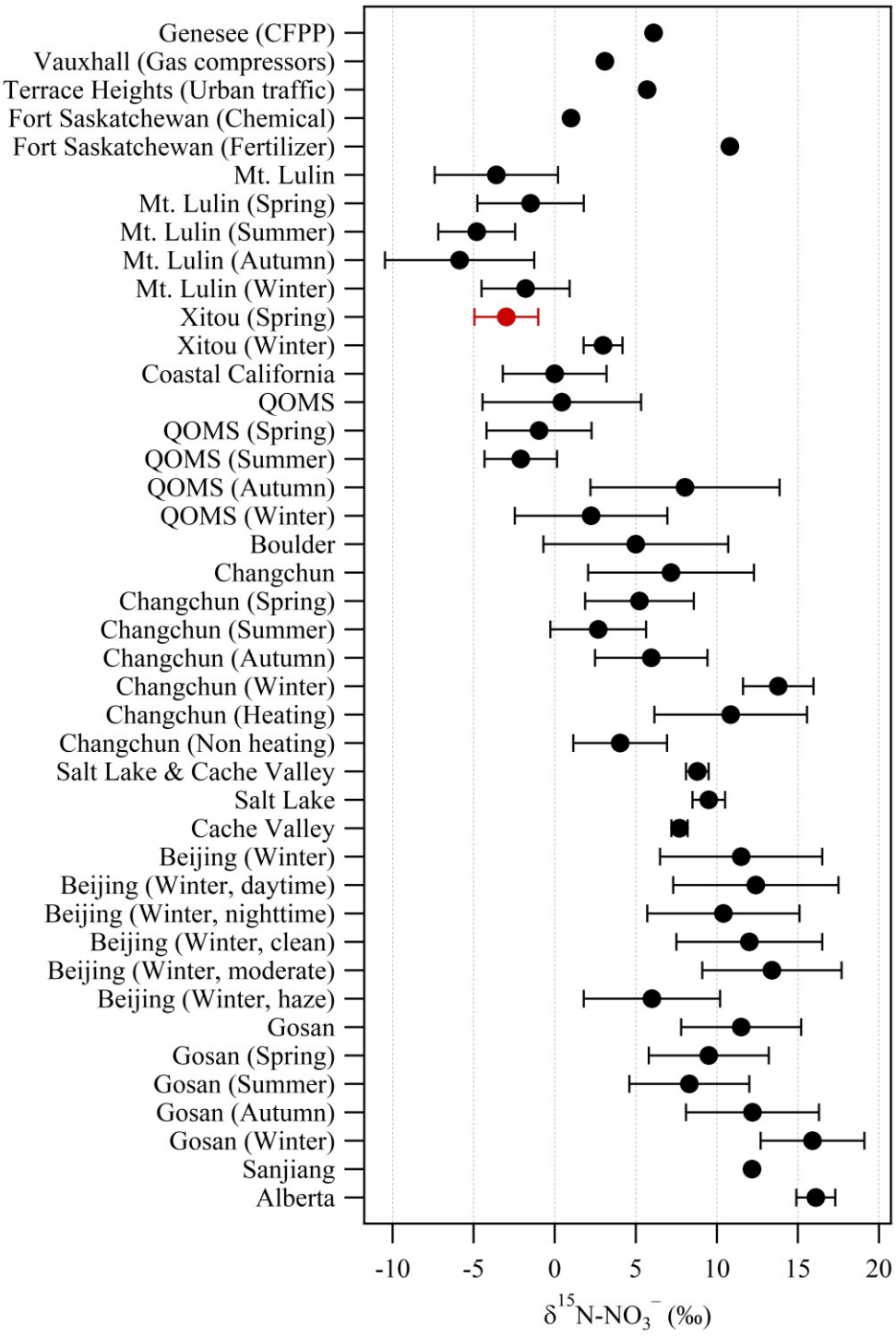

Figure S10. Particulate $\delta^{15}N\text{-}NO_3^-$ measured in this study (red symbol) and reported in the literature (Savard et al., 2018; Guha et al., 2017; Chen et al., 2022; Vicars et al., 2013; Lin et al., 2021; Moore, 1977; Zhao et al., 2020; Hall et al., 2016; Fan et al., 2020; Kundu et al., 2010; Chang et al., 2018; Proemse et al., 2012).

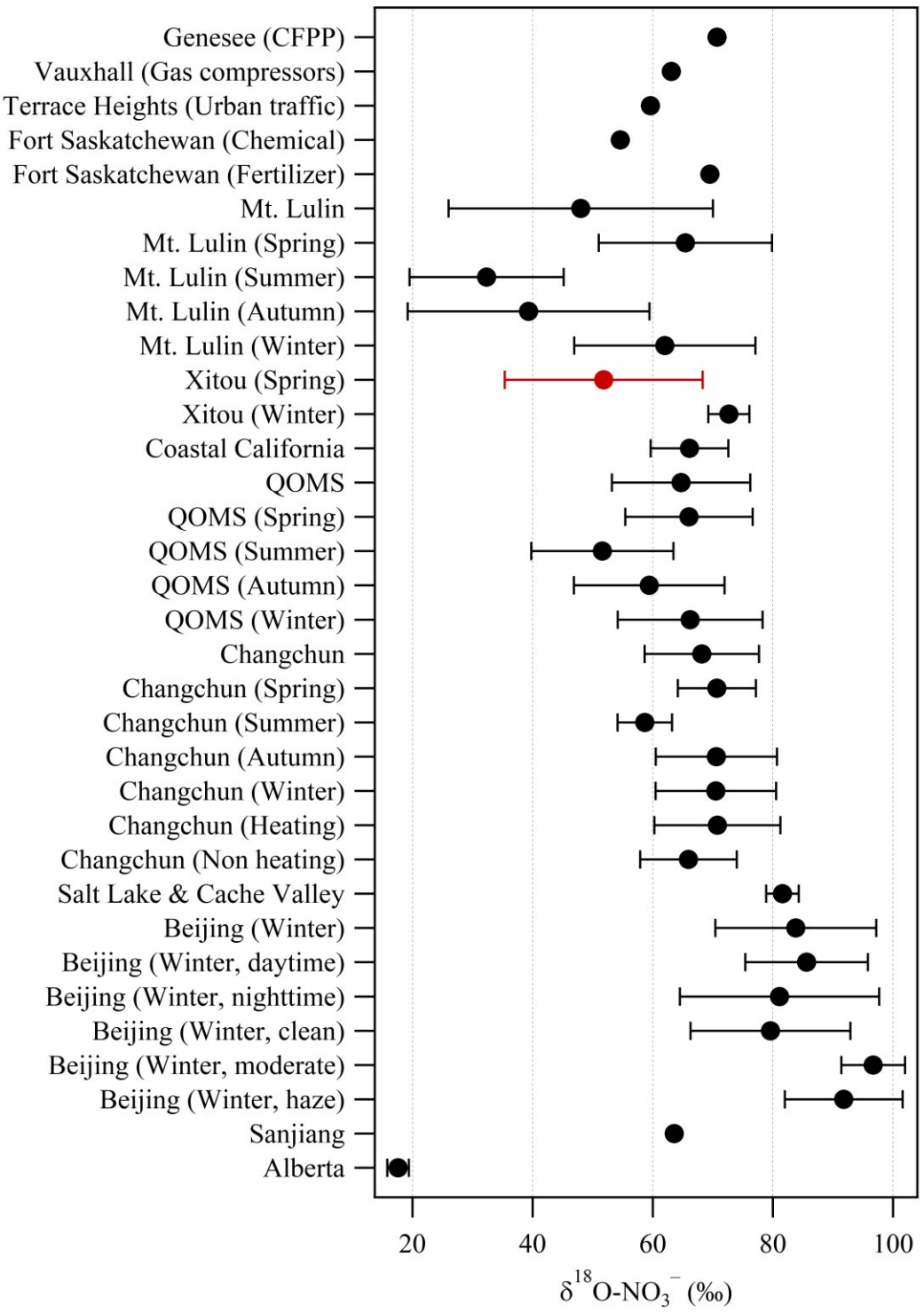

Figure S11. Particulate $\delta^{18}O\text{-}NO_3^-$ measured in this study (red symbol) and reported in the literature (Savard et al., 2018; Guha et al., 2017; Chen et al., 2022; Vicars et al., 2013; Lin et al., 2021; Zhao et al., 2020; Hall et al., 2016; Fan et al., 2020; Chang et al., 2018; Proemse et al., 2012).

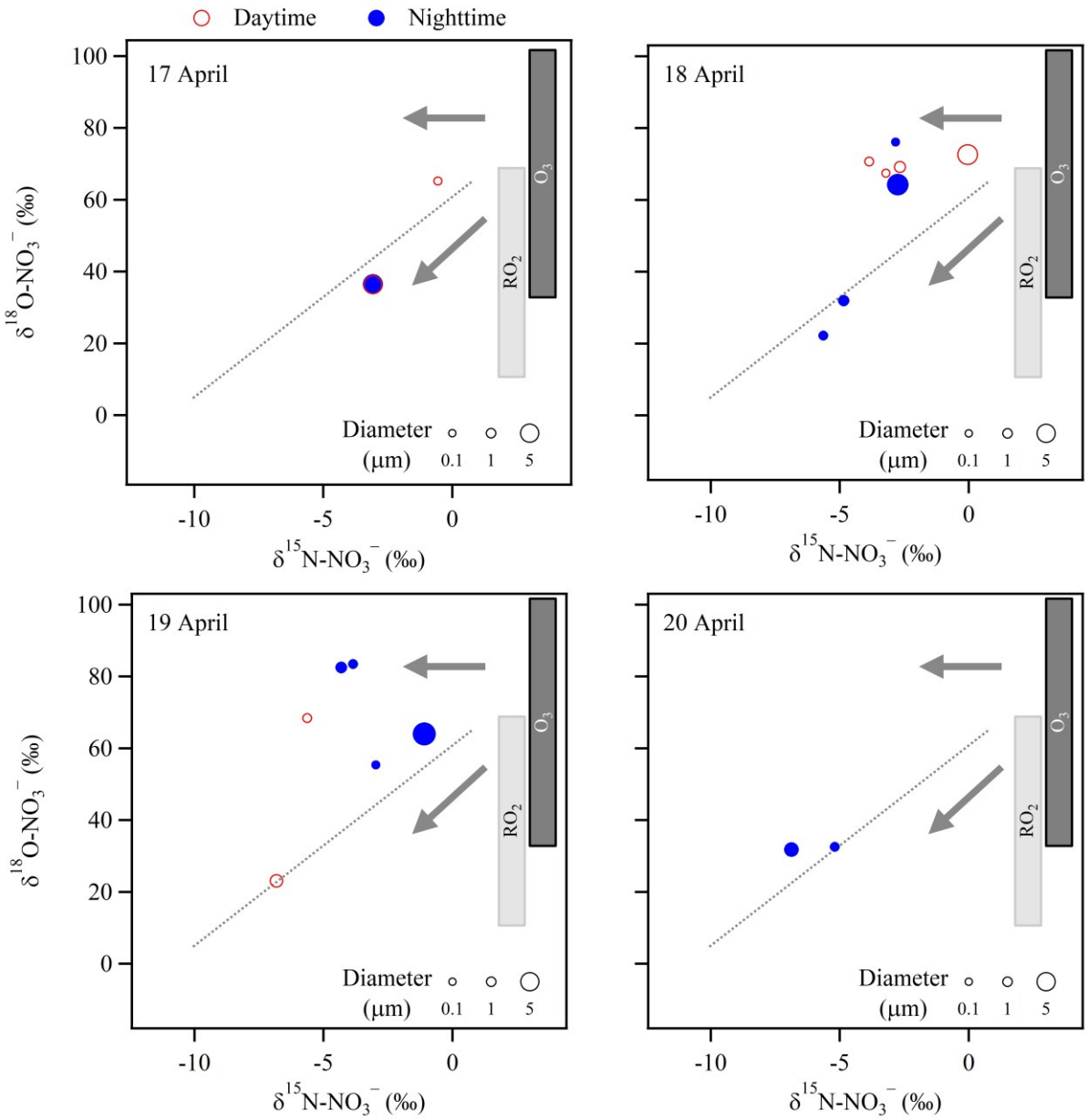

Figure S12. Daily size-resolved isotopic composition of pNO_3^- from 17 to 20 April.

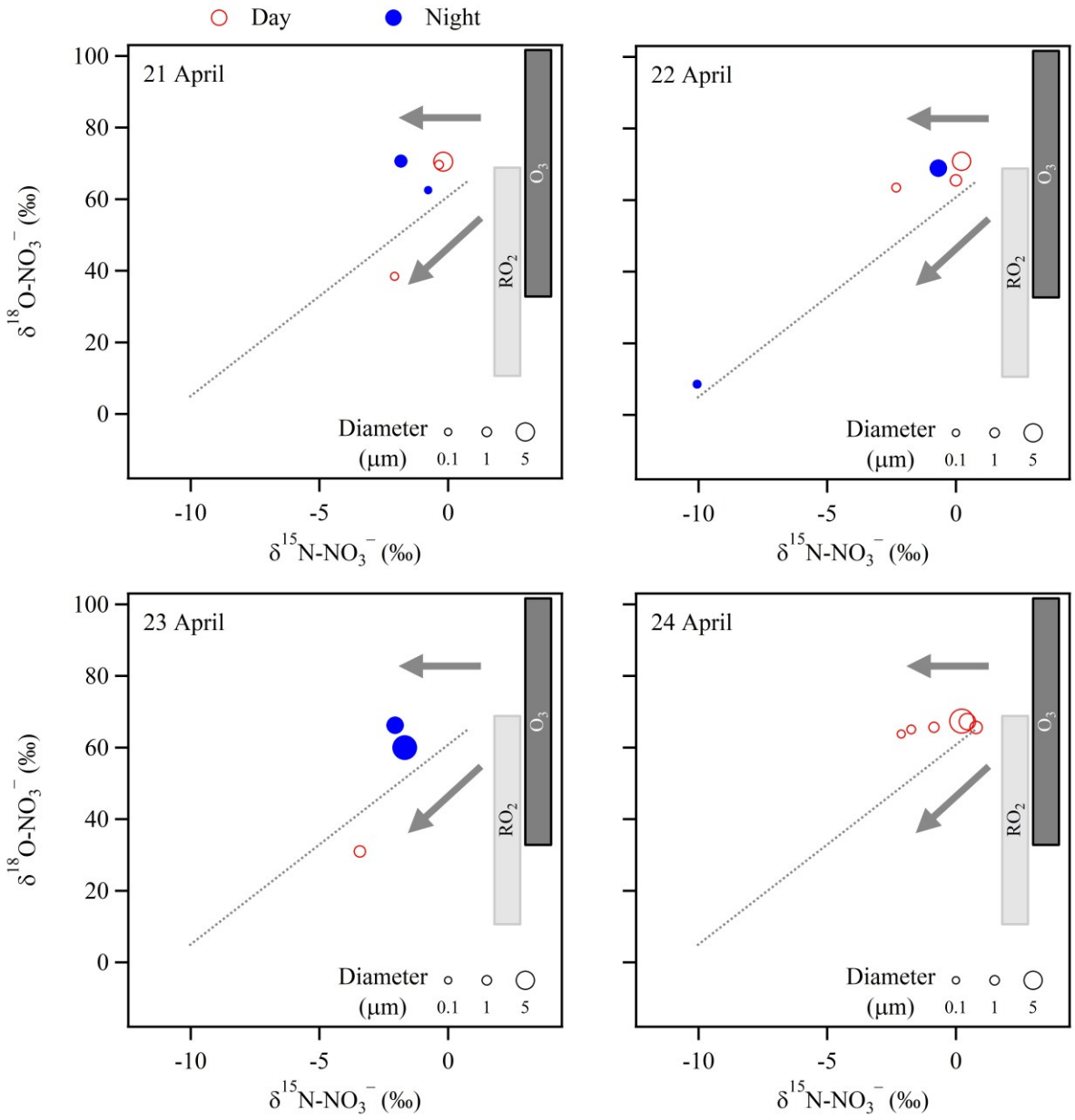

Figure S13. Daily size-resolved isotopic composition of pNO_3^- from 21 to 24 April.

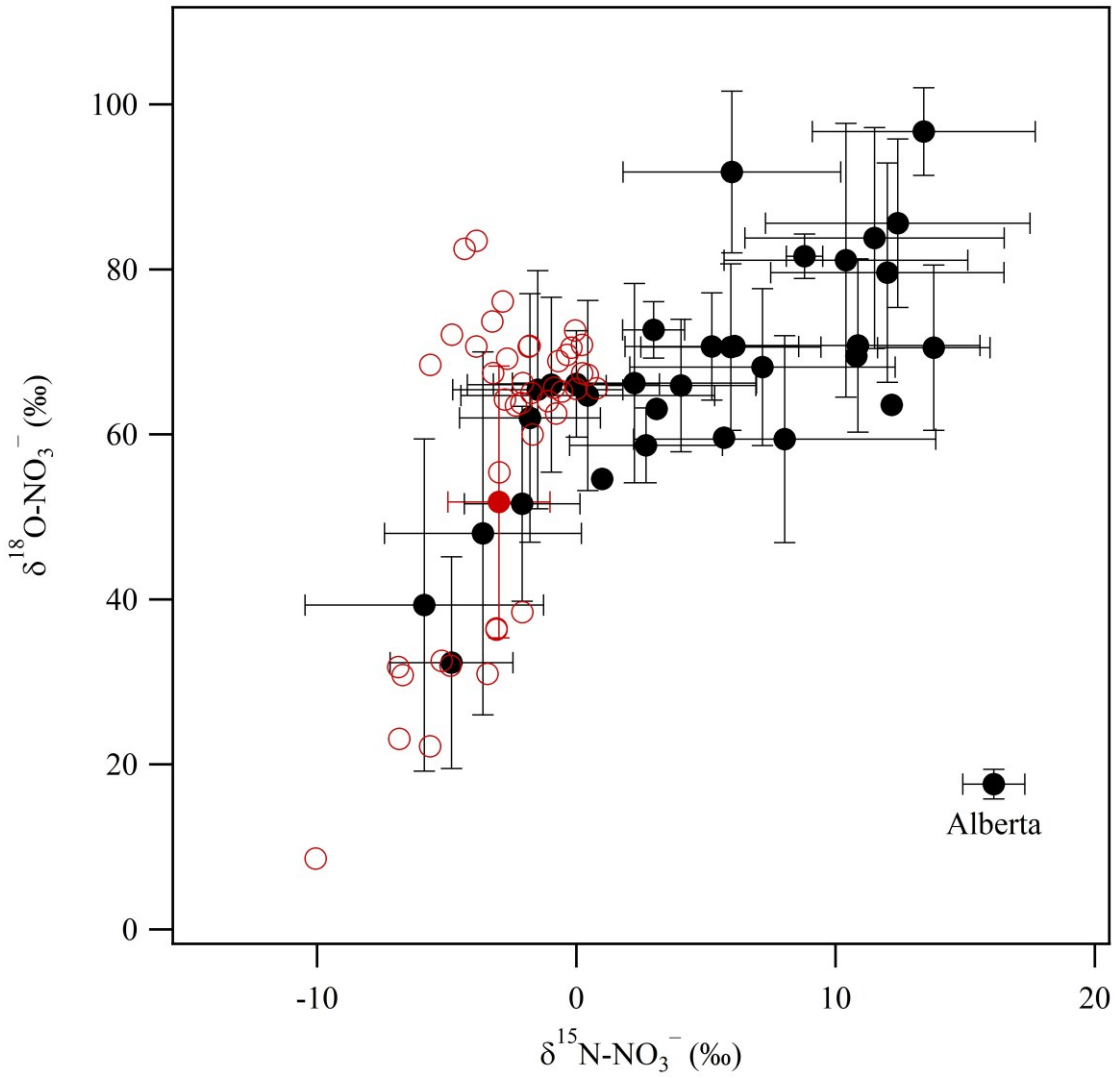

Figure S14. Relationship between particulate δ^{15}N-NO_3^- versus δ^{18}O-NO_3^- in this study (red symbols) and reported in the literature (Savard et al., 2018; Guha et al., 2017; Chen et al., 2022; Vicars et al., 2013; Lin et al., 2021; Zhao et al., 2020; Hall et al., 2016; Fan et al., 2020; Chang et al., 2018; Proemse et al., 2012). Red open circles represent individual measurements from this study, while the red solid circle denotes the mean value.

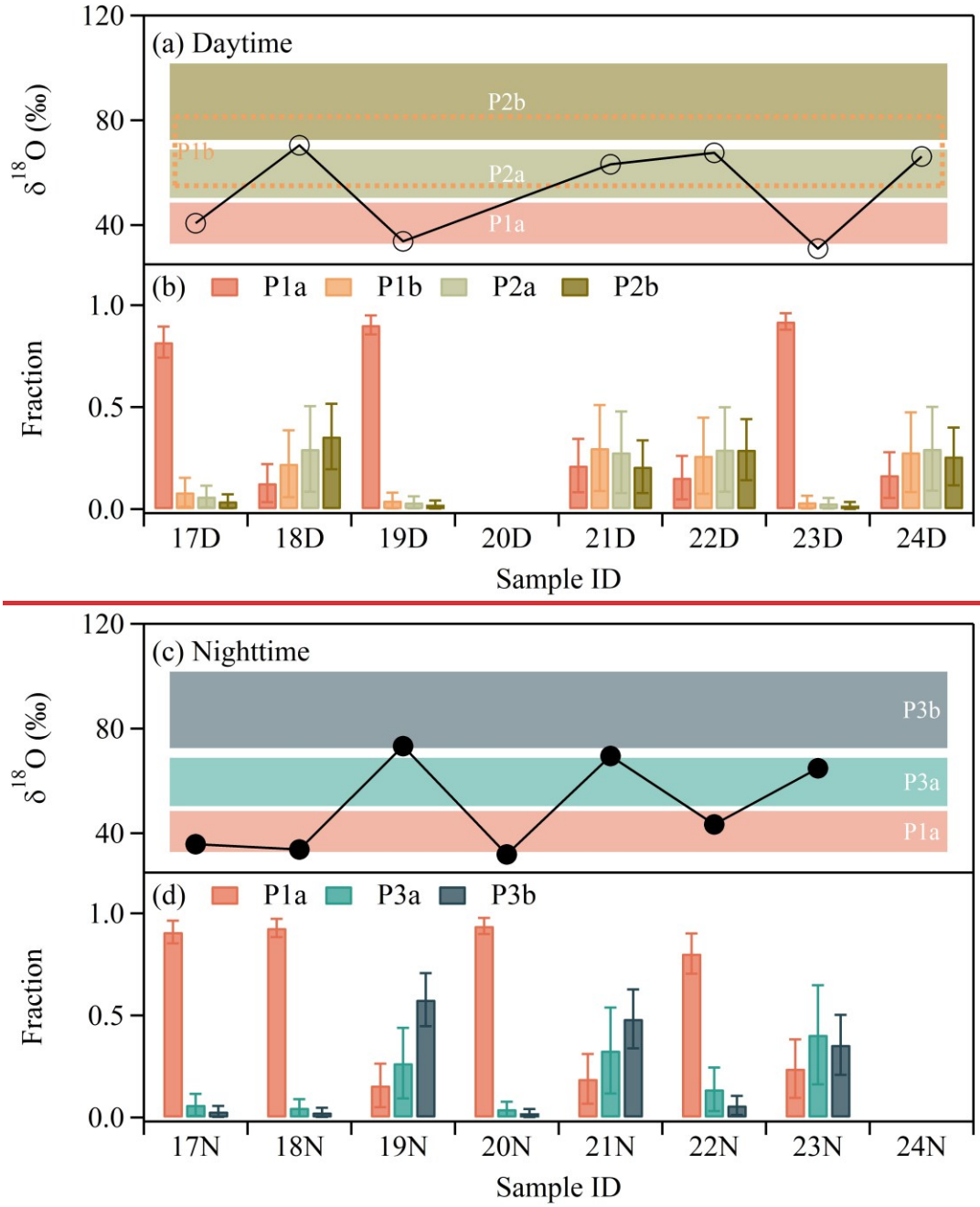

Figure S14. Contributions of nitrate formation pathways estimated by MixSIAR. (a, c) Measured $\delta^{18}O$-NO_3^- values with the corresponding $\delta^{18}O$ ranges of potential formation pathways. (b, d) estimated fractional contributions of these pathways (*c.f.*, Fig. S3).

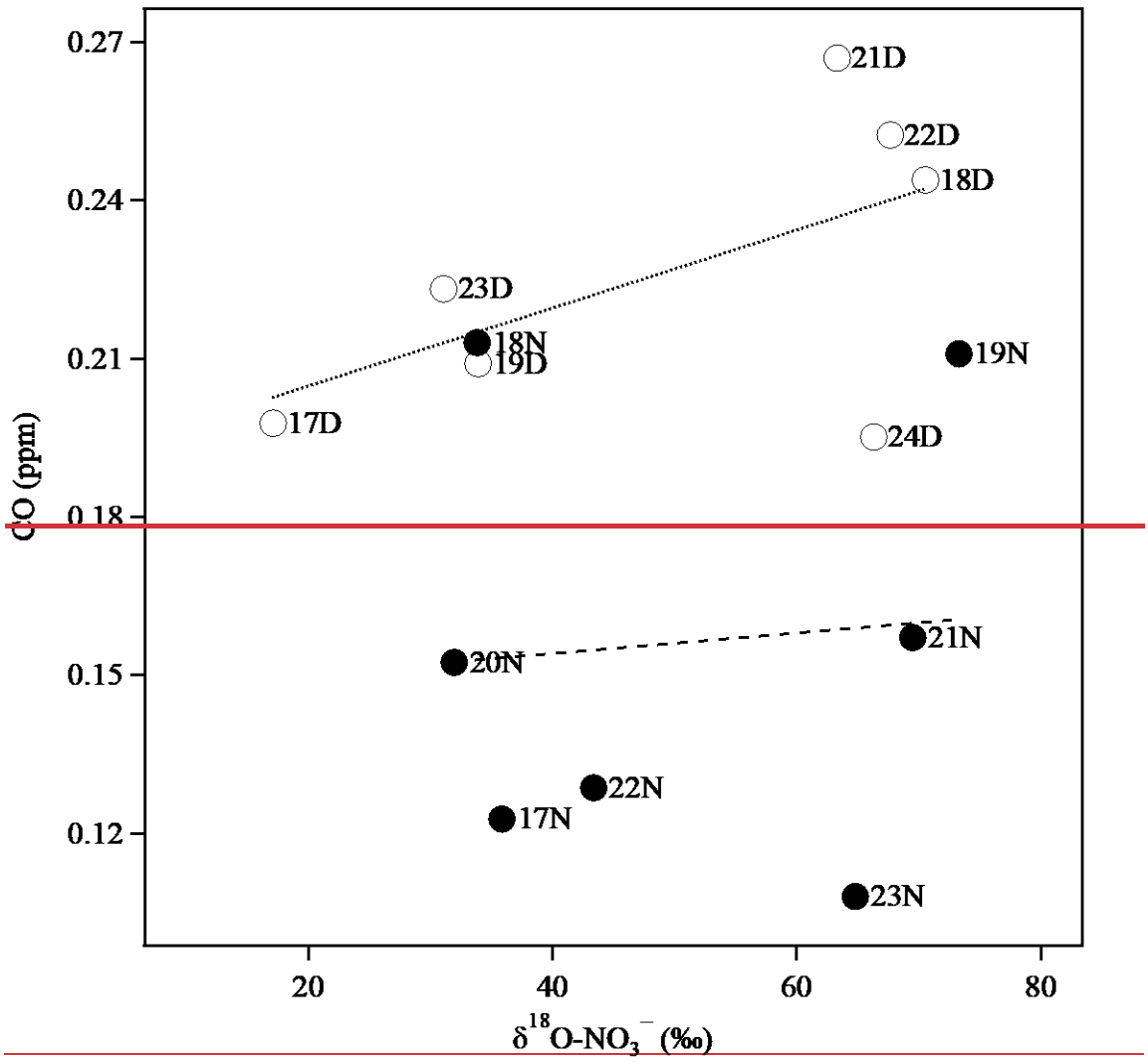
0.27
0.24
0.21
0.18
0.15
0.12
CO (ppm)
20
40
60
80
δ18O-NO3− (‰)
21D
22D
18D
23D
18N
19D
19N
17D
24D
21N
20N
22N
17N
23N

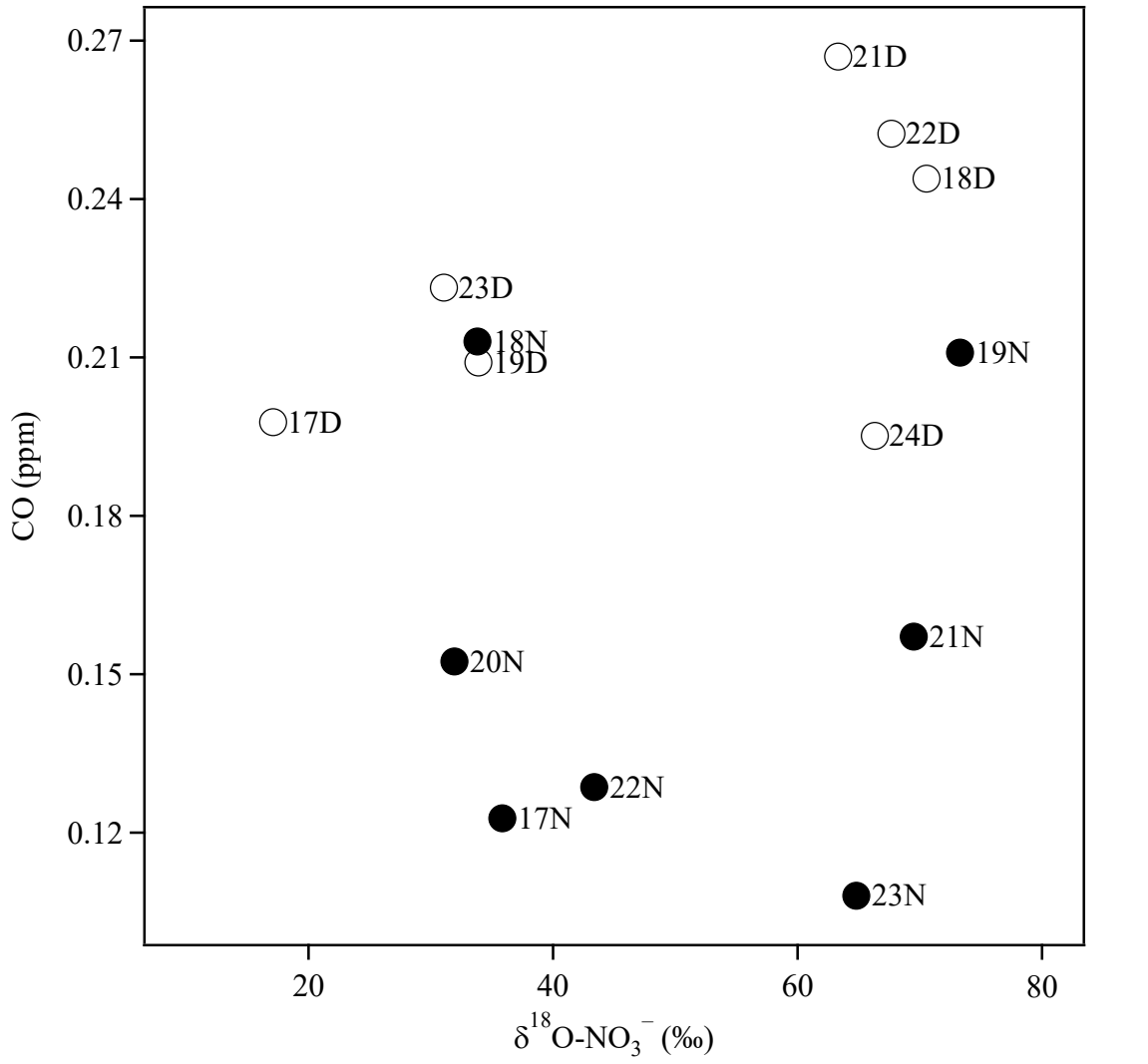

Figure S15. Correlation between daily-averaged CO concentration and $\delta^{18}O\text{-}NO_3^-$.

References

Chang, Y., Zhang, Y., Wang, Q., Shao, S., Bao, M., Zhang, C., and Lehmann, M. F.: Nitrogen isotope fractionation associated with ammonia gas-to-aerosol conversion and implications for determining isotopic source signatures and tracing atmospheric ammonium origins, Environ. Sci. Technol., 59, 22110-22121, https://doi.org/10.1021/acs.est.5c11271, 2025.

Chang, Y., Zhang, Y., Tian, C., Zhang, S., Ma, X., Cao, F., Liu, X., Zhang, W., Kuhn, T., and Lehmann, M. F.: Nitrogen isotope fractionation during gas-to-particle conversion of NO_x to NO_3^- in the atmosphere – implications for isotope-based NO_x source apportionment, Atmos. Chem. Phys., 18, 11647-11661, https://doi.org/10.5194/acp-18-11647-2018, 2018.

Chen, T. Y., Chen, C. L., Chen, Y. C., Chou, C. C. K., Ren, H., and Hung, H. M.: Source apportionment and evolution of N-containing aerosols at a rural cloud forest in Taiwan by isotope analysis, Atmos. Chem. Phys., 22, 13001-13012, https://doi.org/10.5194/acp-22-13001-2022, 2022.

Fan, M.-Y., Zhang, Y.-L., Lin, Y.-C., Cao, F., Zhao, Z.-Y., Sun, Y., Qiu, Y., Fu, P., and Wang, Y.: Changes of emission sources to nitrate aerosols in Beijing after the clean air actions: Evidence from dual isotope compositions, J. Geophys. Res.: Atmos., 125, e2019JD031998, https://doi.org/10.1029/2019JD031998, 2020.

Guha, T., Lin, C. T., Bhattacharya, S. K., Mahajan, A. S., Ou-Yang, C.-F., Lan, Y.-P., Hsu, S. C., and Liang, M.-C.: Isotopic ratios of nitrate in aerosol samples from Mt. Lulin, a high-altitude station in Central Taiwan, Atmos. Environ., 154, 53-69, https://doi.org/10.1016/j.atmosenv.2017.01.036, 2017.

Hall, S. J., Ogata, E. M., Weintraub, S. R., Baker, M. A., Ehleringer, J. R., Czimczik, C. I., and Bowling, D. R.: Convergence in nitrogen deposition and cryptic isotopic variation across urban and agricultural valleys in northern Utah, J. Geophys. Res.: Biogeosci., 121, 2340-2355, https://doi.org/10.1002/2016JG003354, 2016.

Kawashima, H., Yoshida, O., and Suto, N.: Long-term source apportionment of ammonium in $PM_{2.5}$ at a suburban and a rural site using stable nitrogen isotopes, Environ. Sci. Technol., 57, 1268-1277, https://doi.org/10.1021/acs.est.2c06311, 2023.

Kundu, S., Kawamura, K., and Lee, M.: Seasonal variation of the concentrations of nitrogenous species and their nitrogen isotopic ratios in aerosols at Gosan, Jeju Island: Implications for atmospheric processing and source changes of aerosols, J. Geophys. Res.: Atmos., 115, D20305, https://doi.org/10.1029/2009JD013323, 2010.

Lin, Y.-C., Zhang, Y.-L., Yu, M., Fan, M.-Y., Xie, F., Zhang, W.-Q., Wu, G., Cong, Z., and Michalski, G.: Formation mechanisms and source apportionments of airborne nitrate aerosols at a Himalayan-Tibetan Plateau site: Insights from nitrogen and oxygen isotopic compositions, Environ. Sci. Technol., 55, 12261-12271, https://doi.org/10.1021/acs.est.1c03957, 2021.

Moore, H.: The isotopic composition of ammonia, nitrogen dioxide and nitrate in the atmosphere, Atmos. Environ., 11, 1239-1243, https://doi.org/10.1016/0004-6981(77)90102-0, 1977.

Proemse, B. C., Mayer, B., Chow, J. C., and Watson, J. G.: Isotopic characterization of nitrate, ammonium and sulfate in stack $PM_{2.5}$ emissions in the Athabasca Oil Sands Region, Alberta, Canada, Atmos. Environ., 60, 555-563, https://doi.org/10.1016/j.atmosenv.2012.06.046, 2012.

Savard, M. M., Cole, A. S., Vet, R., and Smirnoff, A.: The $\Delta^{17}O$ and $\delta^{18}O$ values of atmospheric nitrates simultaneously collected downwind of anthropogenic sources – implications for polluted air masses, Atmos. Chem. Phys., 18, 10373-10389, https://doi.org/10.5194/acp-18-10373-2018, 2018.

Ti, C., Gao, B., Luo, Y., Wang, X., Wang, S., and Yan, X.: Isotopic characterization of NH_x-N in deposition and major emission sources, Biogeochemistry, 138, 85-102, https://doi.org/10.1007/s10533-018-0432-3, 2018.

Vicars, W. C., Morin, S., Savarino, J., Wagner, N. L., Erbland, J., Vince, E., Martins, J. M. F., Lerner, B. M., Quinn, P. K., Coffman, D. J., Williams, E. J., and Brown, S. S.: Spatial and diurnal variability in reactive nitrogen oxide chemistry as reflected in the isotopic composition of atmospheric nitrate: Results from the CalNex 2010 field study, J. Geophys. Res.: Atmos., 118, 10,567-510,588, https://doi.org/10.1002/jgrd.50680, 2013.

Walters, W. W., Karod, M., Willcocks, E., Baek, B. H., Blum, D. E., and Hastings, M. G.: Quantifying the importance of vehicle ammonia emissions in an urban area of northeastern USA utilizing nitrogen isotopes, Atmos. Chem. Phys., 22, 13431-13448, https://doi.org/10.5194/acp-22-13431-2022, 2022.

Zhao, Z.-Y., Cao, F., Fan, M.-Y., Zhang, W.-Q., Zhai, X.-Y., Wang, Q., and Zhang, Y.-L.: Coal and biomass burning as major emissions of NO_X in Northeast China: Implication from dual isotopes analysis of fine nitrate aerosols, Atmos. Environ., 242, 117762, https://doi.org/10.1016/j.atmosenv.2020.117762, 2020.